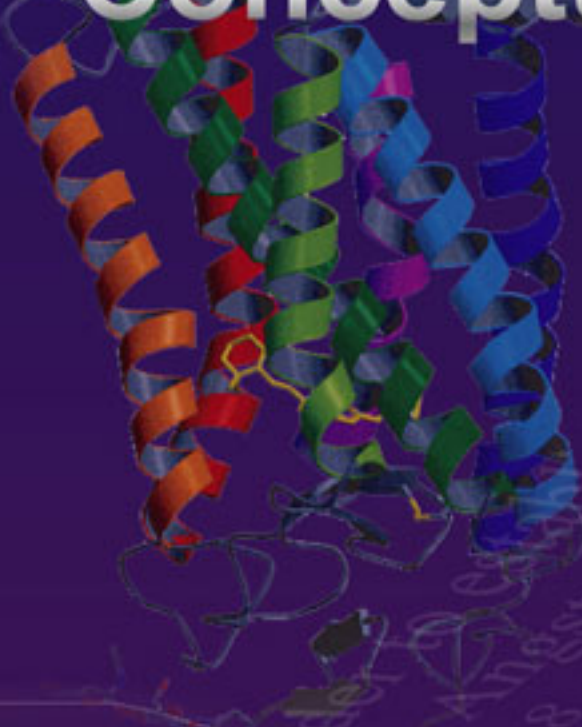


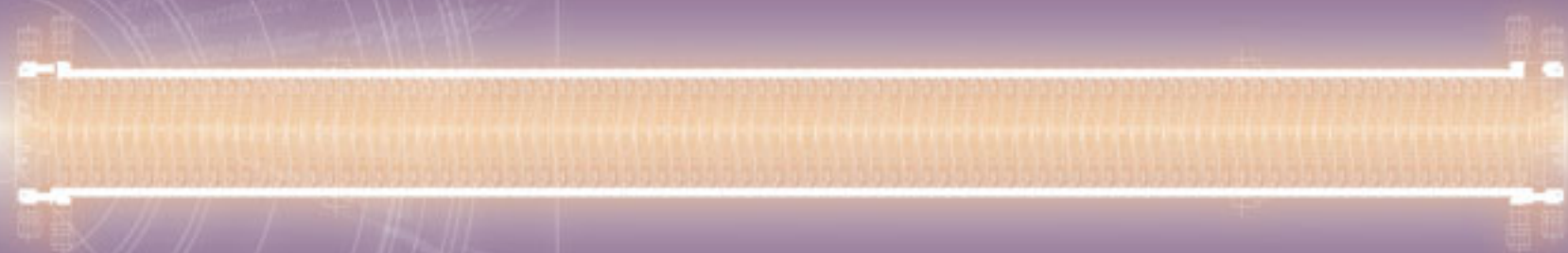
SCSS X-FEL

Conceptual Design Report

May 2005



$$\left(\frac{\partial^2}{\partial x^2} + 2i \frac{\omega}{c} \frac{\partial}{\partial z} \right) \psi \propto h(\mathbf{r}, z) = \left(\frac{\gamma_0}{\gamma_j} e^{-N_j \delta(r-r_j)} \right)$$



SPRING-8 COMPACT SASE SOURCE PROJECT
SCSS SPRING-8
COMPACT
SASE
SOURCE



RIKEN Harima Institute
Coherent X-Ray Optics Laboratory
Coherent Synchrotron Light Source Physics Laboratory
Advanced Electron Beam Physics Laboratory

*This document was created by collaborative work between
JASRI/SPring-8 and Harima RIKEN.
We would like to thank all contributors.....May, 2005*

Copyright © RIKEN, Japan, May 2005. All rights reserved.

SCSS XFEL, R&D Group

RIKEN Harima Institute/SPring-8

1-1-1, Kouto, Mikazuki, Sayo, Hyogo JAPAN 679-5148

Edited by Takashi Tanaka and Tsumoru Shintake

TABLE OF CONTENTS

Table of Contents	1
Introduction	2
Scientific Case	5
Accelerator Design Overview	10
Optimization of Parameters	20
Electron Injector	25
C-band Main Accelerator	33
Undulator Line.....	42
Undulator to Experimental Area:	50
X-Ray Transport System	50
Beam Trajectory control and Alignment	55
FEL Commissioning.....	66
SCSS Control System Conceptual Design	73
Time Base and RF Signal Generation, Transmission and Distribution System	80
Radiation Safety Issues.....	89

INTRODUCTION

The first practical application of synchrotron radiation began in the later part of the 1960's. The electromagnetic wave (light) produced when high energy electrons moving at almost the speed of light have their motion deflected by magnetic fields or otherwise, is what we call synchrotron radiation. If the electron beam is of sufficiently high energy, we can obtain an extremely intense light source covering a broad range of wave lengths from the RF up to soft X-rays. The initial period of the 1960's was when the synchrotron radiation available for applications was generated as a side effect in the beam bending magnets of electron beam accelerators being used for high energy physics experiments. As light sources, the synchrotron radiation of that period was so incoherent that it didn't make sense to even discuss its coherence properties. However, by the 1990's large scale synchrotron radiation light sources, as typified by the 3rd generation SPring-8, had come online. By this generation of machines, the production of synchrotron radiation had transitioned from a bending magnet side-effect, to being the output of purpose-built specialized insertion devices such as undulators. An undulator has a linear array of permanent magnets placed such that their polar orientations are changed in a cyclic fashion. When high energy electron are injected into an undulator, they execute a repeated meandering wavy motion such that the intensity spectrum of the resulting synchrotron radiation is strongly peaked at a particular wavelength (monochromatic) with a laser-like directivity. In other words, when compared with the synchrotron radiation from beam orbit bending devices, the coherence property (brightness characteristic) of undulator sources is overwhelmingly superior, and scientific studies which capitalize on these special features have advanced in rapid progression.

While the coherence properties of these sources are certainly superior to that obtainable from

deflection sources, when compared with the properties taken for granted with lasers, even they appear to be not far from incandescent lamps. For example, it has been said that less than one millionth of the incident light remained after the optical processing needed to obtain coherent radiation for an X-ray diffraction microscopy proof of concept experiment was done with the high brightness radiation from SPring-8. The experiment observed colon bacillus, but the 1000 second exposure time for even a single image was so long at that it would be out of the question to try to observe the dynamics of living organisms that way. Nevertheless, that proof of concept experiment did point out a very important short coming and potentiality. The reason why the long exposure time was needed was that the intensity of the coherent X-rays contained in the SPring-8 synchrotron radiation is entirely too weak. But, if the light intensity could be raised 5 or 6 orders of magnitude, it should be possible to make atomic level observations of living systems with millisecond time resolution.

.When even SPring-8, the world's most intense source of X-rays is unable to provide entirely or even largely coherent X-rays, then the only remaining possible source has to be a source based on the induced emission radiation principle of XFEL, the X-ray Free Electron Laser. Naturally, the use of XFEL will enable closure in research into the interaction of light and matter in experimental regimes heretofore inaccessible, and the potential for single molecule structural analysis, atomic level X-ray microscopy, measurements down to sub-picosecond resolution is under serious discussion. So that going forward, just as happened so often in the past when a new light source became available, we can look for progress in nanotechnology, biological, medical, information science, materials science, all fields of fundamental and essential importance.

The above has presented the motivations behind this present project. The project itself is named SCSS, short for the SPring-8 Compact SASE Source, and the name directly reflects the above concepts and considerations. The reason why we choose this can be seen from the following background. In the decade of the 1990's, one after another 3rd generation large scale synchrotron radiation sources such as ESRF, APS and SPring-8 came online. As scientific results began pouring forth from these facilities as they exploited the special characteristics of high brilliance X-rays for protein structural analysis and the like, more and more interest in using high brilliance X-rays in ever broader scientific fields grew, to the point where it became impossible for the just the three large facilities to keep up with the world-wide demands of users. Further, when we consider the application of high brilliance X-rays to bio and industrial fields, it is natural to expect each country to want to have its own synchrotron radiation facility. However, when we take the current economic situation into consideration, we immediately come to the conclusion that it is not practical at all for each country to attempt construction of its own 6 GeV or higher energy large scale facility.

The large scale synchrotron radiation facilities established in the late 1980's, such as SPring-8, all have their design concepts based on the undulator technology of the time, a technology which from today's standpoint can only be called undeveloped. Even for what was called short period, at best about all that could be practically realized was a 4cm period length. In order to obtain high brilliance X-rays with undulators of this period, the beam energy was raised from 6GeV to 8GeV for these machines. But, in 1990 the in-vacuum undulator, a giant advance in synchrotron radiation insertion devices, was born at KEK. This undulator does not have a vacuum duct inside the magnet gap, and so an extremely small gap can be obtained, limited only by how tightly it can be closed before the accelerator operation would be impacted. As a result, even in an undulator with a very short period a sufficiently strong magnetic field can be achieved.

After that, this undulator technology was much further developed at SPring-8. In particular, the successful joint BNL-NSLS development of an 11mm period, 3.2mm pole piece gap, in-vacuum undulator has completely changed the world view of what 3rd generation synchrotron radiation sources can be, and thus creating what we might call the New Third Generation Source or perhaps the 3rd Generation Source Plus. In its main features, this concept combines an in-vacuum short-period undulator with a low emittance, rather low energy accelerator, so that a facility which while providing performance comparable to the large scale facilities like SPring-8, could be realized at low cost and mid sized scale. The first facility based on this design concept was the SLS (Swiss Light Source); the in-vacuum short period undulator and beam line installed there has already begun producing spectacular results in the field of structural biology. Furthermore, mid-scale facilities of DIAMOND (UK), SOLEIL (France), CLS (Canada), AS (Australia) and SSRF (China) are all currently under construction.

The same considerations can also be applied to XFEL light sources. The first two projects, The European X-Ray Laser Project XFEL (Germany, E=20GeV) and the Linac Coherent Light Source LCLS (USA, E=14.5GeV) as seen from their energy setpoints clearly belong to the large scale facility category. It is obvious that with the exception of the great powers, their scale is such that they could not be constructed by every country independently. Nevertheless, just as we have already seen 3rd generation sources go from large scale to mid-scale facilities around the world, in the near future we may well expect a similar tide in the world of XFEL sources as well. The SCSS project is designed to be the leader in this next wave. One of its design features is the adoption of the in-vacuum short period undulator, just as in the New 3rd Generation synchrotron radiation sources, this allows reducing the beam energy needed. But, this in turn causes a serious problem for the design of the linac. The allowable beam emittance for realizing an XFEL is determined not by the beam

energy, but rather by the target wavelength of the a linac where adiabatic damping reduces the emittance in proportion to the beam energy, when the target wavelength is fixed, when reducing the energy setpoint, the accompanying normalized emittance also has to be reduced proportionally. In other words, this design concept would be rendered impossible if we were restricted to the currently available photocathode electron guns which can not achieve a good enough emittance characteristic. Therefore it is necessary to develop an electron gun with a new principle of operation that can realize an emittance value a factor of $1/2 \sim 1/3$ lower.

In order to realize a mid-scale XFEL, it is also essential to realize a linac with a higher acceleration gradient. Fortunately, in Japan the technology for a practical working C-band accelerator structure is already available. An acceleration gradient of 40 MeV/m can be expected of the acceleration structures. Reiterating the essential components of the mid-scale XFEL concept, we see that the combination of in-vacuum short period undulators, a linac with a rather low energy but with high

radiation to be produced by the XFEL. Therefore in acceleration gradient, and an extremely low emittance electron gun, could make the realization of a low cost, mid-scale machine with performance that could compare favorably with the already ongoing German and US large scale projects. The SCSS project was design based on the above concepts, and has already successfully completed development of the important components.

For a site for the SCSS facility, we are planning on the space adjoining the 1km beam line at SPring-8. There are 3 reasons for choosing the SPring-8 site for SCSS: 1) it would complement the light source characteristics of the current SPring-8 8GeV storage ring, 3rd generation synchrotron radiation source, 2) it would be possible to simultaneously use the synchrotron radiation from the SPring-8 storage ring and the SCSS, and 3) the site provides a bedrock foundation with enough strength to assure a stable nanometer light source.

SCIENTIFIC CASE

Toward the utilization of the SCSS, several users working groups are being organized to discuss innovative sciences at the SCSS. Several Research and Developments for the use of coherent x-rays and/or short pulsed x-rays are ongoing using the 1 km and 27 m undulator beamlines of the SPring-8. These include optics and optical elements, single particle imaging and timing devices.

INTRODUCTION

It is widely recognized that the XFEL light properties are utterly different from those of the 3rd generation synchrotron light. Therefore, sciences to be explored with XFEL should not be mere analytical continuation from sciences with the 3rd generation synchrotron light sources. Recalling the initial planning stage of the SPring-8 utilization, many of the scientific proposals were simple extensions from what were going on 2nd generation sources. However, we know that experiences with the 3rd generation light have been giving birth to unprecedented sciences that were not expected before seeing the real light. Although the scientific case discussed at the moment may be similar, it is not useless to survey and compile the foreseeable scientific trends of XFEL.

On the other hand, accumulated experiences by using coherent x-rays at the 1000 m beam line and high power load at the 27 m undulator beam line of the SPring-8 will surely help develop the instrumentation needed to handle the XFEL beams.

The properties of x-ray beams obtained from the SPring-8 Compact SASE Source (SCSS) are similar to those from other XFEL sources. Nevertheless, we hope the SCSS will be one of the predecessors of compact XFEL in the world, since we may require more similar sources when the XFELs are proved to be extremely useful. The size and cost of the compact XFEL would enable many countries to afford the similar sources.

GENERAL CONSIDERATIONS

XFEL X-rays

SASE-based XFEL will give us unprecedented short-pulsed, spatially coherent and super-intense x-rays. These extraordinary properties will open up a huge number of new possibilities in vast scientific fields as has already discussed in detail in the conceptual design report [1] for LCLS and the technical design report [2] for TESLA-XFEL, which is now reorganized as the European XFEL facility.

At the moment, we have started organizing a users association which gathers potential users from wide range of the scientific fields. A series of workshops will be held to discuss the targets with XFEL in each scientific field, as well as to enhance communication among different fields.

Features of SCSS

Unique feature of SCSS compared with other existing XFEL projects is that it will be constructed adjacent to an operating 3rd generation SR. This will give various opportunities of simultaneous use of XFEL and SR beams. One of the simply conceivable examples may be an XFEL-pump and SR-probe where SR can be hard x-rays for structure dynamics or soft x-rays for electronics dynamics. XFEL x-rays can interact with electrons in the storage ring to give rise to inverse Compton scattering, or can modulate a short portion of electron bunches to produce new phenomena. To use the SCSS linac as an injector of SPring-8 storage ring will open up several new possibilities of producing x-rays with quite different nature from those delivered by the present SPring-8.

USERS ORGANIZATION

In view of the huge potential of XFEL, we are planning to organize users working groups in various fields. These include following scientific working groups:

- Atomic and Molecular Physics
- Condensed Matter Physics
- Materials Sciences
- Chemistry
- Life and Medical Sciences
- Optical and Laser Sciences

Each working group are being asked to organize several workshops where more detailed science cases are to be discussed.

Meanwhile, the developments of some technical issues applicable to interdisciplinary scientific fields are highly demanded. These include:

- Sub-ps to fs timing techniques
- Imaging techniques
- Nanometer focusing techniques
- Detectors
- Optics

These technical developments will be discussed either in the scientific working groups or in dedicatedly organized technical working groups.

In addition to the discussion among domestic scientists, international collaboration should be organized to facilitate information exchange. The tri-party workshop held by ESRF, APS and SPring-8 for the information exchange among large scale 3rd generation synchrotron radiation facilities would be a model for establishing a new international collaboration scheme among XFEL facilities.

ONGOING R&DS

Coherence preservation is the first-priority issue in developing optics for XFEL. By using partial coherent x-rays available at 1000 m beamline and high-brightness x-rays from the 27 m undulator of the SPring-8, several R&Ds for XFEL optics are underway. In fact, any optical elements in the coherent x-ray beam can be origins of unwanted interfering contamination of the beam. Therefore, further development of optical elements

for coherent beam is highly demanded. We are proceeding of the development of slit apertures, Be windows giving no interference fringes, super-smooth x-ray mirrors and high-perfection synthetic diamond crystals.

Ion Beam Figuring (IBF)

In performing coherence-related experiments even at the SPring-8 beam lines, speckles from slit and/or pinhole apertures always become a problem. Conventional machining techniques can hardly make a smooth figure required for coherent x-rays. The speckles observed are a result of interference. Therefore, it is difficult to subtract the background in the intensity regime since the background itself is a result of interference between unwanted radiation and real signals. To minimize the unwanted radiation, or at least to make the background easily treated, the surface finish of the slits or pinholes before the sample should be as smooth as possible. For this purpose, we are collaborating with a group of the University of Hyogo to finish the aperture surfaces using the Ion Beam Figuring (IBF) technique. Figure 1 illustrates a Ta pinhole (a) made with laser machining and (b) with IBF. Considerable improvement is observed both for the shape and surface roughness. We are planning to make x-ray tests soon.

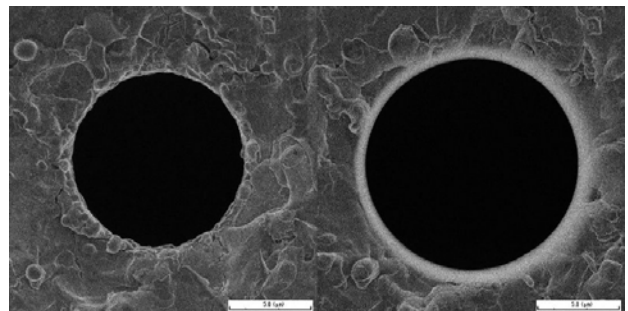


Fig. 1 SEM pictures of pinholes in Ta plates: laser drilled with 10 mm diameter (left); IBF machined with 13 mm diameter (right).

Be Window Development

One of the astonishing observations at undulator beamlines of the SPring-8 was the interference fringes caused by the imperfections of Be windows.

At the beginning, we attributed the origin of the fringes to surface imperfections. Accordingly, we have replaced the windows by super-polished Be foils with 0.1 μm Ra. The beam images after the windows became more uniform with the replacement, but interference fringes still remained. We have examined several types of Be foils with phase contrast x-ray imaging, and found that Be materials contain many void defects that produce interference fringe patterns [3]. Since Be foils can be an important candidate for the vacuum sealing windows of XFEL, further improvement in quality is highly demanded. There may be another approach not to use any windows but differential pumping system. However, we have a clear evidence at the 27 m undulator beam line that the filtering of lower energy components with Be window helps preventing the first optical elements from deteriorating with the radiation.

Super-Smooth X-Ray Mirrors

X-ray mirrors are another possible origin of interference speckles when illuminated with highly coherent x-rays. Super-smooth x-ray mirrors that produce no interference speckles are being developed in collaboration with a group of Osaka University. An atomic-level surface figuring technique called Elastic Emission Machining (EEM) [4] combined with a new surface figure metrology called micro-stitching interferometer [5] has enabled to fabricate super-smooth mirrors with less than 1 nm peak-to valley figure error even for aspherical shaped mirrors when applied to single crystal silicon crystals. A Kirkpatrick-Baez mirror composed of uncoated elliptical mirrors gave a focal size of 180 nm \times 90 nm at the 1000 m end station [6]. A new coating technique that does not introduce deterioration in surface quality is being developed to increase the usable glancing angle, thus enabling to fabricate aspherical mirrors with larger numerical apertures. As a result, a preliminarily fabricated elliptical mirrors gave a focal size of 40 nm \times 40 nm.

In parallel with the development of the super-smooth mirrors, a computer code based on the

wave-optical theory was developed for the simulation of x-ray reflection properties from rough mirror surfaces. Conventional ray-tracing programs based on the geometrical optics, such as SHADOW, cannot fully predict the reflection properties of rough mirrors when the incident x-rays are coherent. The newly developed code numerically solves the Fresnel-Kirchhof integral with measured surface figure data as a boundary condition.

Synthetic Single Crystal Diamond

Single crystals of diamond may be one of the few candidates that can overcome the unprecedented high power of XFEL, though the detailed interaction scheme is not yet fully revealed. Actually, heat load at some of the 3rd generation undulator beam lines is already above the limit of cryogenic cooling of silicon ($\sim 500\text{W}/\text{mm}^2$), so that diamonds are seriously considered as the first optical elements in such beam lines [7]. However, the current crystal quality of the diamond is not as high as that of the best silicon. In particular, it is still an open question whether the diamond crystal can preserve x-ray coherence.

The SPring-8 optics group has been collaborating with Sumitomo Electric Industries Co. Ltd toward the growth of diamond crystals with higher quality for more than ten years. Various types of characterization made at the SPring-8 have contributed to the improvement in crystal growing processes at Sumitomo. The characterization techniques include x-ray rocking curve measurements, x-ray topography, triple-crystal diffractometry, surface-figure profiling and x-ray fluorescence analysis. The long collaboration has led to the current availability of high quality crystals with a small number of stacking faults and dislocations [8].

Single Particle Imaging

Visualizing the arrangement of atoms has played a crucial role in understanding the microscopic world. There are already a few ways of imaging atomic structures, but each has its limitations. Scanning probe microscopes are limited to imaging

atomic structures at surface. Transmission electron microscopes can resolve atoms but only for samples thinner than ~ 30 nm. Crystallography can reveal the globally averaged 3D atomic structure based on the diffraction phenomenon, but requires crystals. These limitations can in principle be overcome by coherent diffraction imaging that is based upon the principle of using coherent x-ray scattering in combination with a method of direct phase recovery called oversampling [9]. Coherent diffraction imaging has been successfully applied to 2D and 3D imaging of nanoscale materials [10,11] and biological samples [12]. A highest spatial resolution of 7 nm has been achieved, while the ultimate resolution is only limited by the X-ray wavelengths. By using the 3rd generation synchrotron radiation sources, better-designed instruments and more robust image reconstruction algorithms, we expect to improve the spatial resolution to the 1 nm level within the next few years. Meanwhile, we will also pursue its applications in materials and nano science. We will focus on 3D imaging of porous silica particles, GaN semiconductors, quantum dots and mineralized bone composite. The ability to image the internal pore structures in three dimensions, 3D morphology of GaN and its alloys in nanocrystal form, and 3D internal structures of quantum dots, coupled with computational methods such as molecular dynamics and *ab initio* calculations, will profoundly expand our understanding of the critical structural and morphological features required to make superior catalysts, adsorbents, electrodes and semiconductors. Understanding the mineral component of bone such as the size, shape and arrangement of the calcium apatite crystals in a collagen matrix will be of fundamental importance in biology and medicine. In the long run, in a combination of brighter X-ray sources and pixel array detectors with higher quantum efficiency and a higher dynamic range, coherent diffraction imaging could potentially be used to determine the 3D structure of single particles down to the single atom level [13].

Time-Resolved Scattering/Spectroscopy

Several devices for the ps timing measurement at the SPring-8 beam lines have been developed. However, it would be difficult to use the existing devices for much faster timing measurement at the SCSS. A time-to-space converter (TSC) [14] could be one of the solutions. A post-processing system using TSC is under discussion.

REFERENCES

- [1] "Linac Coherent Light Source (LCLS) Conceptual Design Report", SLAC-R-593, April 2002.
- [2] "TESLA Technical Design Report, PART V, The X-Ray Free Electron Laser", ed. G. Materlik and Th. Tschentscher, March 2001.
- [3] S. Goto et al. "Characterization of Beryllium Windows Using Coherent X-Rays at 1-km Beamline," AIP Proc. vol. 705, 2004, pp. 400-403.
- [4] Y. Mori, Y. Yamauchi and K. Endo, "Mechanism of Atomic Removal in Elastic Emission Machining," *Precis. Eng.* **10**, 1988, pp.24-28.
- [5] K. Yamauchi et al. "Microstitching Interferometry for X-Ray Reflective Optics," *Rev. Sci. Instrum.* **74**, 2003, pp. 2894-2898.
- [6] K. Yamauchi et al. "Two-Dimensional Submicron Focusing of Hard X-Rays by Two Elliptical Mirrors Fabricated by Plasma Chemical Vaporization Machining and Elastic Emission Machining," *Jpn. J. Appl. Phys.* **42**, 2003, pp. 7129-7134.
- [7] <http://www.esrf.fr/Conferences/DiamondWorkshop/>
- [8] K. Tamasaku et al., "Goniometric and Topographic Characterization of Synthetic Ila Diamonds," XTOP 2004 Abstracts, 2004, p.88. Proceedings will appear in *J. Phys. D* if the paper is selected by the committee.
- [9] J. Miao et al., "Extending the Methodology of X-Ray Crystallography to Allow Imaging of Micrometer-Sized Non-Crystalline Specimens," *Nature*, 400, 1999, pp. 342-344.
- [10] J. Miao et al., "High Resolution 3D X-Ray Diffraction Microscopy," *Phys. Rev. Lett.* **89**, 2002, art. no. 088303.
- [11] J. Miao et al., "Phase Retrieval of Diffraction Patterns from Non-Crystalline Samples using Oversampling Method," *Phys. Rev. B*, 67, 2003, art. no. 174104.

- [12] J. Miao et al., "Imaging Whole Escherichia Coli Bacteria by using Single-Particle X-Ray Diffraction," Proc. Natl. Acad. Sci. **100**, 2003, pp. 110-112.
- [13] J. Miao, K. O. Hodgson and D. Sayre, "An Approach to Three-Dimensional Structure Analysis of Biomolecule by using Single-Molecule Diffraction Image," Proc. Natl. Acad. Sci. **98**, 2001, pp. 6641-6645.
- [14] Y. Tanaka et al. "Time-to-Space Converter for Ultrashort Pulsed X-Ray Experiments," AIP Proc. vol. 705, 2004, pp. 1379-1382.

ACCELERATOR DESIGN OVERVIEW

In SCSS project, three key technologies enable to construct a SASE mode FEL within available site length of 800 m at SPring-8. They are (1) low emittance electron injector using single crystal thermionic cathode and velocity bunching scheme, (2) high gradient C-band main accelerator, (3) short period undulator of in-vacuum type. By using shorter undulator period of 15 mm, we can lower the electron beam energy as low as 6 GeV to generate coherent X-ray radiation at 0.1 nm wavelength. The C-band rf system can generate 32 MV/m accelerating gradient using 50 MW class klystrons. 6 GeV (or 8 GeV) beam energy is available in accelerator length of 240 m (or 320 m). Including undulator length of nearly 100 m and X-ray beam line of 200 m, the total facility length becomes 750 m, which fits the open space at SPring-8 site.

XFEL MACHINE LAYOUT

Figure 1 shows the machine layout of X-ray FEL. The facility building is designed to house the higher energy machine up to 8 GeV. The electron gun, injector system located left end, and the electron beam will be accelerated in the S-band and C-band main accelerator from left to right, reaches to maximum energy at 350 m downstream. In the beam switchyard, the electron beam will be switched into different undulator lines in pulse-to-pulse time sharing mode, or shift-to-shift slow switching mode, or distribute bunch-by-bunch by fast sweeping along multi-beam line.

The proposed site is nest to the 1 km X-ray beam line at SPring-8, see Fig. 2, where 800 m long and 100 wide area has been reserved for future upgrade.

When the SPring-8 was constructed, the west north side hill was open cut, from where a large amount of rock were removed and buried in this site. About ten years have past after constructed, thus we believe the basement is steady enough. Detail survey is scheduled from this year.

In Fig. 1, the green coloured area under the undulator lines and X-ray beam delivery, was originally hill, rock base, and it is quite steady. In the X-ray FEL machine, most sensitive part to the position movement is the undulator line and user-facility, both of them are located mostly original rock base. Therefore, ground motion due to seasonal changes, or change due to weather (rain or dry high temperature) will be negligibly small.

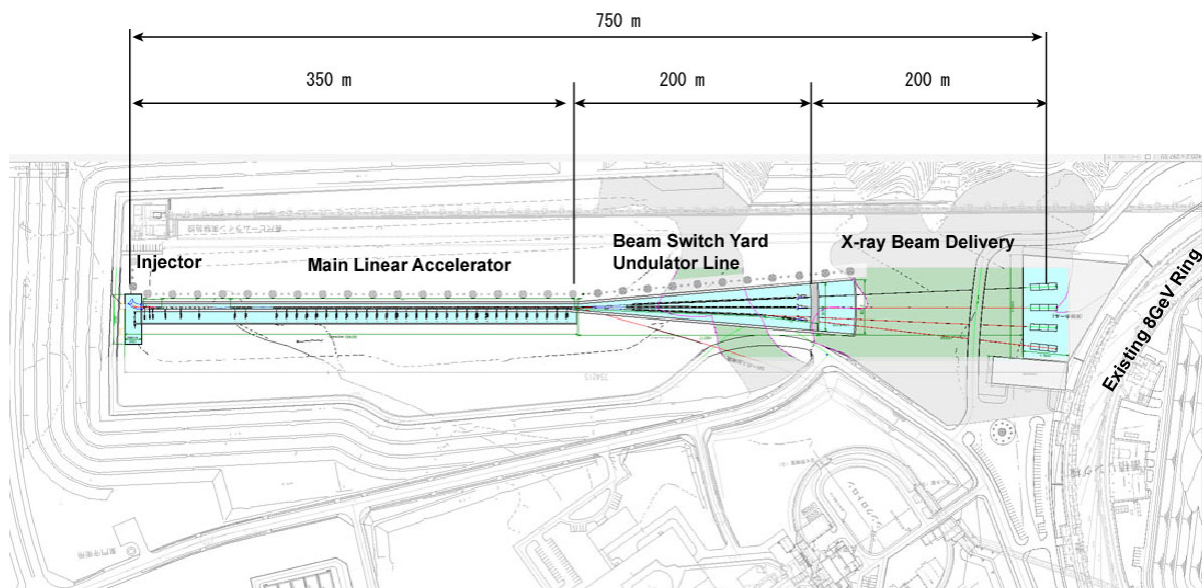


Fig. 1 XFEL machine layout and facility building. Total length fits available site length of 800 m.



Fig. 2 Proposed site for XFEL machine at SPring-8.

SCSS CONCEPT

Figure 3 shows the key technology in SCSS project. In SCSS project, three key technologies enable to construct a SASE mode FEL within available site length of 800 m at SPring-8. They are (1) low emittance electron injector using single crystal thermionic cathode and velocity bunching scheme, (2) high gradient C-band main accelerator,

(3) short period undulator of in-vacuum type. By using shorter undulator period of 15 mm, we can lower the electron beam energy as low as 6 GeV to generate coherent X-ray radiation at 0.1 nm wavelength. The C-band rf system can generate 32 MV/m accelerating gradient using 50 MW class klystrons. 6 GeV (or 8 GeV) beam energy is available in accelerator length of 240 m (or 320 m). Including undulator length of nearly 100 m and X-ray beam line of 200 m, the total facility length becomes

750 m, which fits the open space at SPring-8 site.

ELECTRON SOURCE DESIGN

As discussed in the later section on the machine parameter, XFEL requires high peak current and low emittance beam. In SCSS, it is 3 kA and $0.85 \pi \cdot \text{mm} \cdot \text{mrad}$. We may not generate this beam directly from any kind of cathodes, therefore we

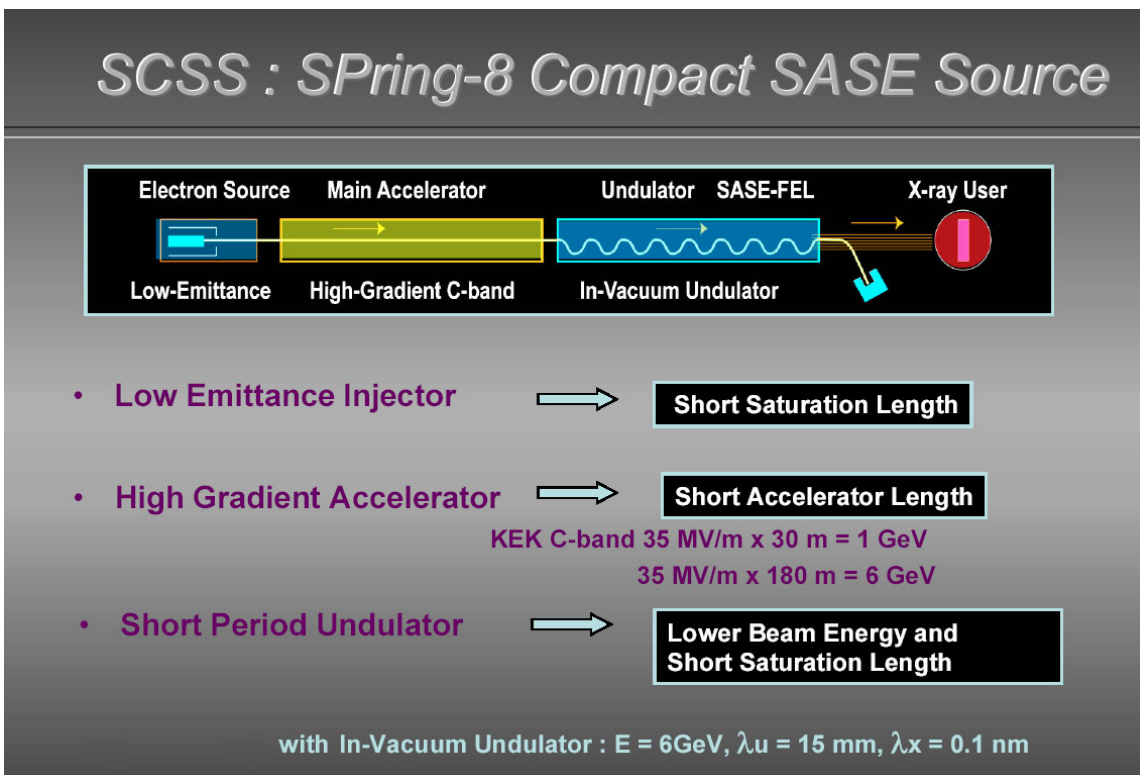


Fig. 3 Three key technologies in SCSS enable compact SASE-FEL machine.

Table-1 Comparison of rf-gun and thermionic cathode electron sources.

	Rf-gun with photocathode and short pulse laser	Thermionic cathode electron gun, followed by buncher.
Beam emittance from the cathode	$< 1 \pi$.mm.mrad depend on cathode size.	$< 1 \pi$.mm.mrad depend on cathode size.
Peak current available from cathode	> 100 A	a few Ampere max. current density < 100 A/cm ²
Emittance deterioration	rf field inside rf-gun creates correlated beam emittance growth, part of which can be compensated by a solenoid field.	There is no big deterioration in the gun. The rf-field inside pre-buncher and buncher system creates correlated beam emittance growth. By choosing lower rf frequency, it may lowered very small.
Bunch length from cathode	~ 1 psec, depends on laser pulse. Very short pulse < 0.1 fsec is also possible, but too short pulse causes emittance growth inside the rf-gun.	Long, basically DC beam. The control grid can not be used, since it breaks the emittance badly. We need beam chopper and pre-buncher and buncher system.
Merit	Direct generation of high current and short-bunch from cathode using short pulse laser.	Stable electron emission property for long period of operation. Low field on cathode, and no dark current emission.
Demerit	<u>High dark current</u> To extract short pulse beam from the cathode, very high accelerating field is required to suppress the space charge field effect. High dark current emission from the cathode runs through the accelerator, and cause radiation damage on undulator magnet.	<u>Complicated system</u> Need beam chopper, pre-bunch and buncher system. However, a laser system for the cathode as rf-gun is not required, and also its associated facility, manpower are not required.

must rely on bunch compression scheme using magnetic chicane. As discussed in later section of start-to-end simulation, in the magnetic chicane bunch compressor, the coherent synchrotron radiation (CSR) breaks the emittance in case of high compression ratio. By using two stages compression scheme, we may tolerate this effect. In SCSS, the total compression ratio is 75. In this compression ratio, no much emittance growth is expected. The peak current requirement becomes 40 A before the bunch compressor.

To generate 40 A peak current, there are two possible choices, (1) rf-gun with photo-cathode illuminated by short-pulse laser, (2) thermionic-cathode followed by traditional pre-buncher and buncher system. They are compared in Table-1. We

chose the thermionic cathode rather than the rf-gun. This is mainly due to superior stability and system reliability in the thermionic cathode. To an operate user facility, the first priority is the higher beam availability, which will be supported by high reliability and stability of the machine. From this point of view, we decided not to use the rf-gun system, which is not fully reliable yet, and the laser system requires manpower and frequent maintenance.

About the dark current, it will be emitted from the copper surface in the accelerating structure, and it can be transported down through the linac together with the main beam. 2D phase-space plot (r, r') of the dark-current emission has an empty hole at the center, since all of these trajectory

started from the copper surface, while the main beam stays at the center, thus it can be fully eliminated by using properly designed collimator. On the other hand, the dark-current from the cathode surface occupies the same phase space as the main beam, thus it can not be eliminated with collimators, and cause radiation damage on the undulator magnet. The rf-gun needs very high electric field on the cathode in order to quickly accelerate the bunched electron beam, therefore higher dark-current emission will be generated.

CHOICE OF TECHNOLOGY FOR THE MAIN AC ACCELERATOR

Some of the recently started new FEL projects have decided to employ the superconducting accelerator technology, mostly running at 1.3 GHz L-band frequency. Advantages in the superconducting accelerator are

- (1) Superconducting rf-cavity is able to run as CW mode, where the rf power to the beam energy efficiency becomes higher.
- (2) After intensive R&D for TELA e⁺e⁻ linear collider project, it has been proven that the superconducting rf cavity can handle high accelerating gradient as high as 30 MV/m or even higher at long pulse mode. However, we have to note that linear collider design assumes pulse mode operation, while XFEL requires CW mode operation for superconducting cavity to provide higher average beam power, where the accelerating gradient is still limited around 10 MV/m.
- (3) Peripheral hardware components (klystron, coupler, tuner, cryogenic system etc.) have been well developed and some of them are now available from industry.

However, we did not choose the superconducting technology in SCSS project, because

- (1) Project target is to generate coherent X-ray at wavelength $\sim 1 \text{ \AA}$, which is not a soft X-ray, thus the beam energy has to be as high as 6 GeV by using the short period in-vacuum undulator of 15 mm period.

- (2) To accelerate beam up to 6 GeV by the present superconducting technology, the machine size beam too large. The achievable accelerating gradient in today's superconducting accelerator will be to be 12 MV/m (CEBAF upgrade design), the active accelerator length becomes 500 m and accelerator length will be ~ 600 m including focusing system and beam diagnostics, which does not fit our site. Also, the total construction cost of the main accelerator (accelerator, refrigerator and facility tunnel) becomes much higher than normal conducting design.
- (3) Our major interests in X-FEL beam is its high peak brightness rather than high average brightness derived from CW beam. Therefore, the maximum pulse repetition rate of 60 Hz is acceptable for most scientific cases. For the multi-beam-line option, we accelerate the multi-bunch beam in each pulse and distribute each bunch to the multi-beam-lines by scanning kicker magnet.
- (4) Actual hardware implementation of the superconducting accelerator system is much more complex than the normal conducting accelerator system. We need many specialists (scientist and technician) not only for the installation but also for the maintenance.
- (5) The normal conducting accelerator system has been widely used and its technology has been well established. Thus we can construct the normal conducting accelerator system within a reasonable cost and maintain it with minimum manpower.

When we look a long-term perspective for 10 years or even longer, after the SCSS, there might be needs for the superconducting option in XFEL, because of its intrinsic superior performance: better beam stability and CW mode operation.

We propose SCSS X-FEL project as a short to middle-term project, i.e., from the case study to beam commissioning must fit within five years (two years engineering design and short term R&D, three years facility and machine construction). Only the

normal conducting technology fits this project at present.

If we do this project in correct time-scale, many new findings will be made in this machine quickly. Therefore, normal conducting accelerator design is the best choice. For details, see the later section.

UNDULATOR

There are several special requirements on undulator for the SASE-FEL, and discussed below.

- (1) Very long undulator line: ~ 100 m. We use segmented undulators of 4.5 m long, and install in the line with focusing element and BPM in between. We have technology established in the storage ring undulators at RIKEN/SPring-8. We are studying on maintenance issue and production cost.
- (2) Small gap: < 5 mm. This small gap size has been sometimes used in storage ring undulators, thus technically manageable. The various wakefield effects become larger

when the gap is small, and careful theoretical studies have been carried out in many laboratories. The wakefield is a kind of space charge effect, and the influence on the electron bunch is always collective effect, i.e. it cause projected emittance growth, but it does not deteriorate the slice emittance.

- (3) Very tight tolerance on electron beam trajectory straightness, it is less than $10 \mu\text{m}$ transverse for 10 m travel distance. As discussed later section, we have established technology to control the beam trajectory in this precision.

For details on undulator design, see later section.

OPTIMIZATION OF PARAMETERS

In designing each component in the FEL facility of SCSS, various parameters such as the electron energy, peak current, energy spread, undulator period and field strength, etc., should be carefully determined in order to realize lasing at 1 Å wavelength with the scale of facility as compact as possible. In practice, we need to optimise these values because they are closely related with each other.

UNDULATOR PARAMETER

The wavelength λ of FEL radiation is determined by the equation

$$\lambda = \frac{\lambda_u}{2\gamma^2} \left(1 + \frac{K^2}{2} \right),$$

where γ is the Lorentz factor of the electron beam and λ_u is the periodic length of the undulator. The parameter K , called a deflection parameter, is a dimensionless magnetic field strength of the undulator and given as

$$K = \frac{eB_0\lambda_u}{2\pi mc},$$

where e and m are the electron charge and mass, B_0 the peak field of the undulator, and c the speed of light. Assuming a pure Halbach configuration, the peak field is roughly estimated as

$$B_0 = 1.8B_r \exp(-\pi g / \lambda_u) \times \alpha,$$

where B_r is the remanent field of the permanent magnet material, g the magnetic gap and α a 3-

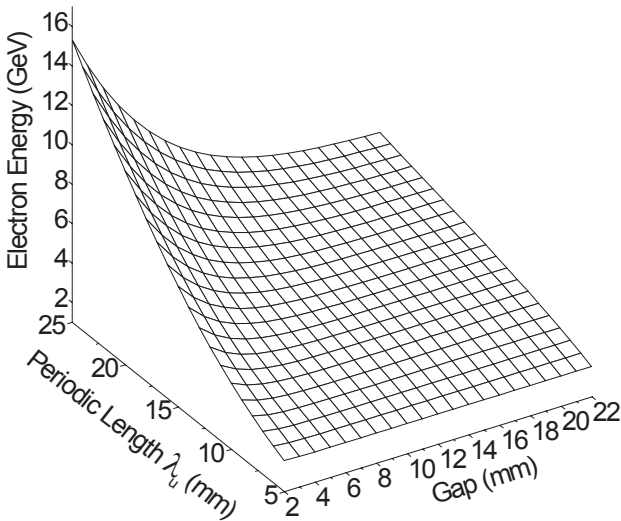


Figure. 1 Electron energy as a function of the periodic length and gap of the undulator to provide 1 Å radiation.

dimensional geometrical factor of permanent magnet blocks. Using these formulae, the relation between the parameters λ_u , γ , and g can be plotted as shown in Fig 1. In principle, it is possible to take any combination of (λ_u, g, γ) indicated in the figure to realize 1Å FEL. It should be noted, however, that the FEL amplification efficiency is also dependent on these parameters, which actually gives a scheme to find the optimum set of these parameters.

Under 1-dimensional approximation, the FEL radiation power is amplified according to the equation

$$P \propto \exp(z / L_g),$$

with

$$L_g = \frac{\lambda_u}{4\pi\sqrt{3}\rho},$$

$$\rho = \left[\frac{\gamma\lambda^2 r_e n_e}{8\pi} F_1(K) \right]^{1/3},$$

$$F_1(K) = \frac{K^2}{(1 + K^2/2)^2} \times$$

$$\left[J_0\left(\frac{K^2/4}{1 + K^2/2}\right) - J_1\left(\frac{K^2/4}{1 + K^2/2}\right) \right]^2,$$

where r_e is the classical radius of electron, n_e the electron density, J_0 and J_1 the Bessel functions of 0th and 1st order. The parameter L_g is called gain length and has a dimension of length, while ρ is called FEL parameter and is dimensionless. Thus ρ can be used to estimate the performance of FEL system. Apart from the wavelength λ to be fixed at 1Å, ρ is dependent on three parameters, γ , n_e , and K . Among them, n_e is independent of the other two parameters. Thus a figure of merit, q , for optimisation of parameters is the quantity $q = (\gamma F_1)^{1/3}$.

The contour plot of this quantity is plotted as a function of λ_u and g in Fig. 2 together with that of the electron energy. In terms of the FEL amplification, larger value of q is preferable, while lower electron energy results in a more compact facility and lower total cost. Thus, we have chosen the three parameters, the electron energy, periodic length, and nominal gap at point indicated by the cross mark in the figure, i.e., $E = 6$ GeV, $\lambda_u = 15$ mm, $g = 3.5$ mm. The K value in this case is calculated as $K=1.3$.

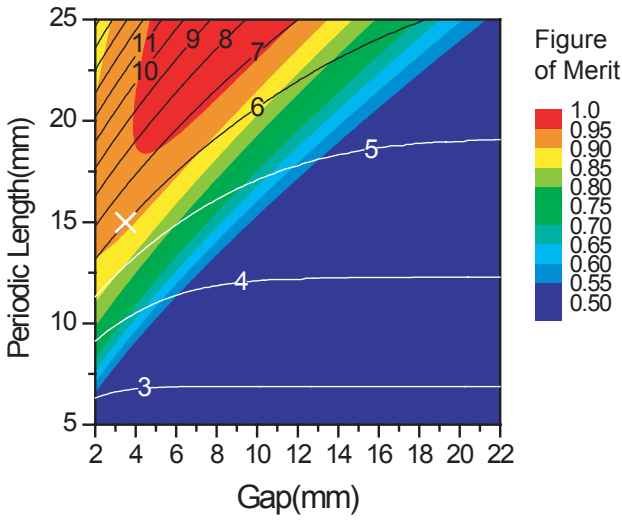


Figure. 2 Contour plot of the figure of merit (colour plot) and electron energy (indicated by numbers) for 1Å wavelength.

REQUIREMENTS ON THE BEAM PARAMETER

Having optimised several parameters for 1Å wavelength, the requirement on the electron beam parameters, the emittance, current, and energy spread, are investigated. We can use the universal scaling function for the FEL gain length ($L_{g,3d}$) with the 3-dimensional effects and energy spread of the electron beam taken into account, which has been derived from rigorous analysis on the FEL process [1]. Using the function, the gain length is expressed as

$$L_{g,3d} = L_g (1 + \eta),$$

with

$$\eta = F(\lambda_u, \gamma, L_g, \lambda, \beta, \varepsilon_n, I_p, \sigma_E),$$

being the scaling function composed of the above 8 input arguments and 19 fitting parameters. Among the arguments, the average betatron function β , normalized emittance ε_n , peak current I_p , and energy spread σ_E are still unknown and should be determined.

It is easy to understand that $L_{g,3d}$ is a monotonous function of ε_n , I_p , σ_E , i.e., lower values of ε_n and σ_E and a higher value of I_p results in a shorter gain length. On the other hand, there is an optimum value of β to obtain shorter $L_{g,3d}$ as shown in Fig. 3. Thus, β can be optimised for each set of ε_n , I_p , and σ_E .

Now we can investigate the requirements on the beam parameters to realize the 1Å FEL. Figure 4(a)~(d) shows contour plots of saturation length as a function of I_p and σ_E for different values of the natural emittance. The saturation length is given by

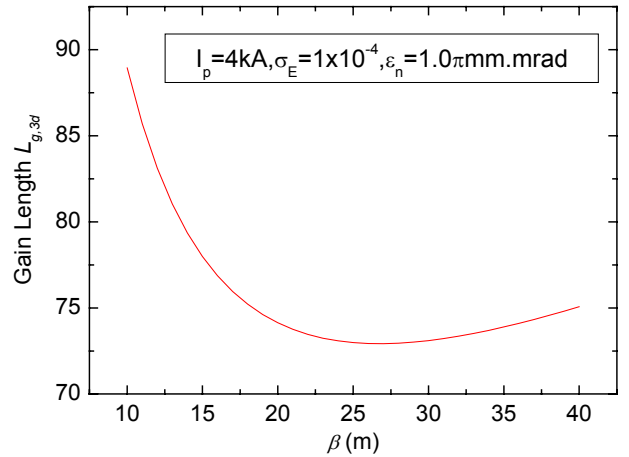


Figure. 3 Example of β dependence of $L_{g,3d}$. Other parameters necessary to calculate the scaling function are indicated in the figure.

$$L_{sat} = L_g \ln \left(\frac{P_{sat}}{P_{in} / 9} \right).$$

with

$$P_{in} = \rho^2 c E / \lambda$$

and

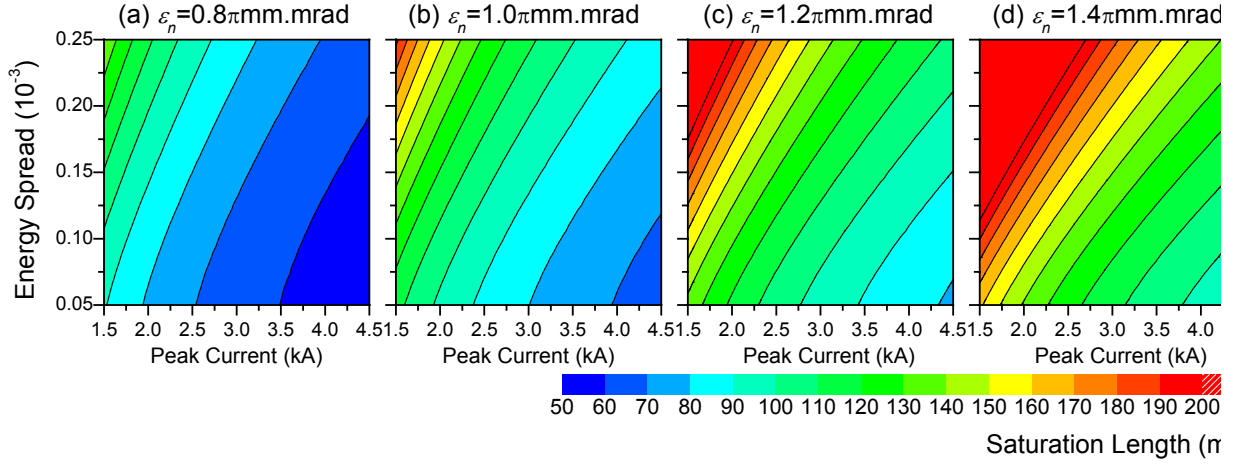


Figure. 4 Contour plots of the saturation length as functions of I_p and σ_E for different values of the natural emittance.

$$P_{sat} = 1.6\rho \left(\frac{L_g}{L_{g,3d}} \right)^2 P_{beam}$$

being the effective input noise power and saturation radiation power, respectively [1]. The total length of the undulator should be longer than L_{sat} to ensure saturation of the FEL radiation power. In each set of parameters ε_n , I_p and σ_E , β are optimised to give the shortest length of $L_{g,3d}$.

START TO END SIMULATION

Machine layout

Schematic layout of the 6 GeV machine is shown in Fig. 5. In order to estimate electron beam parameters and radiation performance, start to end simulation is carried out using three codes, PARMELA for the injector, ELEGANT for the main LINACs and bunch compressors and GENESIS for the undulator.

Expected electron beam parameters at injector

The initial condition of the simulation is based on the results of the emittance measurements of the electron gun. Since PARMELA can not treat a DC electron gun, the simulation does not fully reproduce the results of the emittance measurement.

In the simulation, 500 keV energy is immediately given to the electrons at the start and no DC acceleration process at the gun cathode is considered. Therefore, the effect of the space charge would be underestimated. Figure 6 compares the measured and simulated profiles of the electron beam under the same set up used for the emittance measurements. The effect of the space charge, which bends the edges of the distribution, is different between Fig. 6 (a) and (b). However, the initial condition of the simulation is determined so as that the divergences of the electron beam at $x = 0$ are consistent with each other as shown in Fig. 6 (c). In a real machine, this initial condition can be achieved by eliminating the edges of the distribution (Fig. 6 (a)) using a pin-hole slit. In this case, the emittance of the beam core neglecting the bent edges is about 0.5π mm-mrad and this beam core and 1 A beam current is used as the initial condition of the simulation.

A schematic of the SCSS injector is shown in Fig. 7. As described in the previous chapter, an electron pulse with 1~2 ns duration is produced from μ sec cathode emission by a chopper installed between the electron gun and a 238 MHz PB (Pre-Buncher). In the 238 MHz PB, the energy of the electron bunch is modulated as a function of its longitudinal position. This energy modulation turns into a velocity difference of the electrons. When the phases of the RF fields in the 238 MHz PB, 476

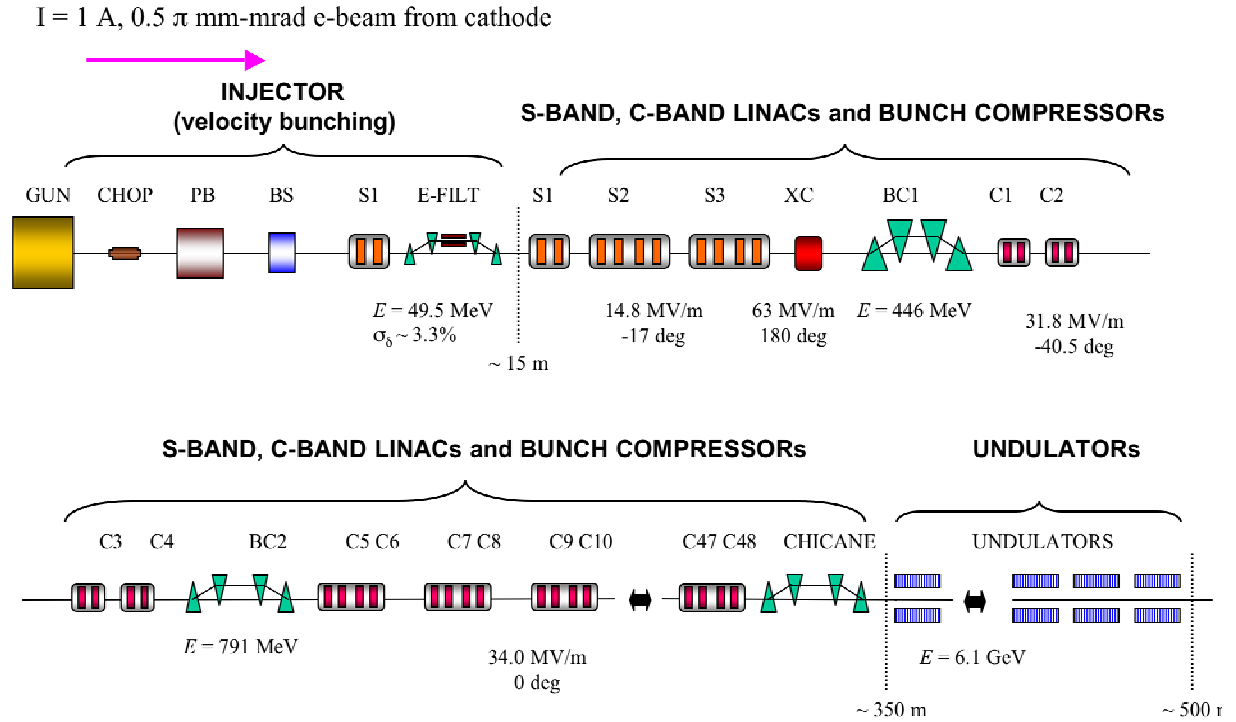


Fig. 5 Schematic layout of the 6 GeV machine

MHz booster and S-band LINACs are properly chosen, the length of the bunch can be compressed as it moves toward downstream. Thus the peak current of the electron bunch can be increased.

The energy and current profiles of the electron bunch at various locations in the injector are shown in Fig. 7 (a) ~ (d). The head of the bunch corresponds to the smaller time scale in Fig. 7 (a) ~ (d). At the end of the injector, the peak current close to 40 A is obtained with the beam energy of 50 MeV.

The emittance is another important parameter of the electron beam. Since a wavepacket of the emitted light in the undulator can interact only with a small fraction of the electron bunch, local property of the electron bunch is important for the SASE radiation. The local emittance of the electron bunch, so-called a slice emittance, is calculated and shown in Fig. 8. Since the electron beam energy in the injector does not fully get to a relativistic regime, the emittance of the beam is degraded due to the space charge effect as the peak current increases. The slice emittance at the end of the

injector is estimated to be about $0.85 \pi \text{ mm-mrad}$ as shown in Fig. 8 (c).

Main LINACs and bunch compressors

There are two stages of bunch compressors (BCs) in the current machine layout (Fig. 5) [2]. The first BC is located at the beam energy of $\sim 450 \text{ MeV}$. After the injector, the electron beam is accelerated up to 482 MeV in S-band LINACs. Before the first BC, the electron beam is decelerated in an X-band harmonic cavity as shown in Fig. 9 in order to correct the nonlinearity of the energy slope due to the RF curvature.

Between the first and second BCs, the beam is accelerated in C-band LINACs. The schematic layout and parameters of the second BC is described in Fig. 10. The configuration of the four bending magnets are the same for the two BCs, but the bending angle and compression factor of the second BC are set to be smaller in order to reduce the CSR effect [3, 4]. Figure 11 compares the normalized slice emittance at the two BCs, and it is

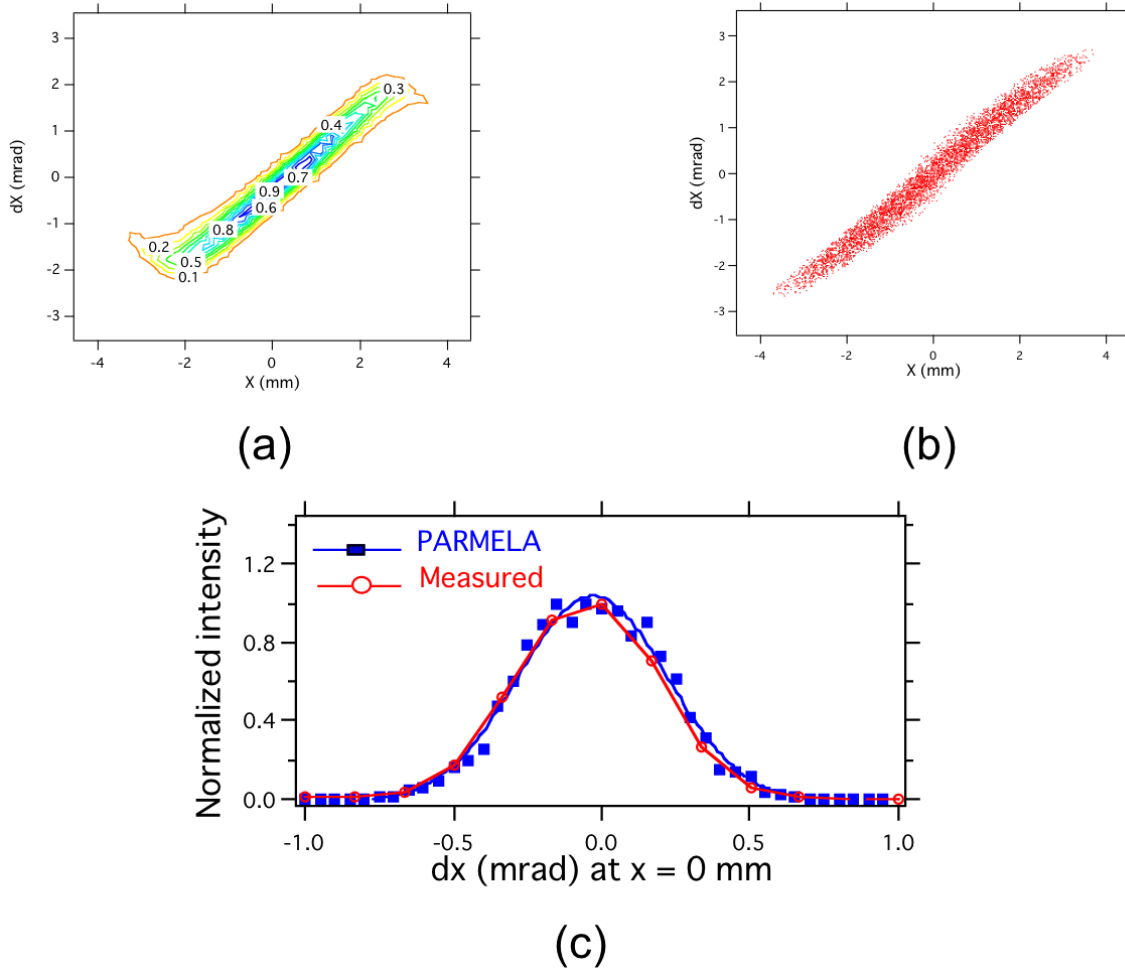


Fig. 6 Phase space profiles of the electron bunch, (a) measured and (b) calculated with PARMELA. The divergence of the electron beam at $x = 0$ (mm) is plotted in (c).

shown that there is no significant emittance degradation at the two BCs.

After the second BC, the electron bunch is accelerated up to 6 GeV with on crest phase of the C-band LINACs, and no further compression is occurred at the final chicane. Final projected emittance is about 3π mm-mrad at the end of the accelerator.

Figure 12 is the electron beam lattice used for the simulation. The beta function is minimized at the fourth bending magnets of the two BCs, and an FODO lattice is applied in the C-band LINACs and the undulator section.

Electron energy	6.135 GeV
Normalized slice emittance	$\sim 0.85 \pi$ mm.mrad
Peak current	~ 3 kA
Slice energy spread	$\sim 4 \times 10^{-5}$
Undulator period	15 mm
Undulator section length	4.5 m
Undulator gap (nominal)	3.5 mm
K value (nominal)	1.3
β function at undulators	~ 30 m
Radiation wavelength	~ 0.1 nm
FEL parameter	2.8×10^{-4}
3-D gain length	3.7 m

Table 1. Slice beam parameters of the center part of the electron bunch (blue part in Fig. 13 (b)), together with the parameters of the SASE radiation and the undulator.

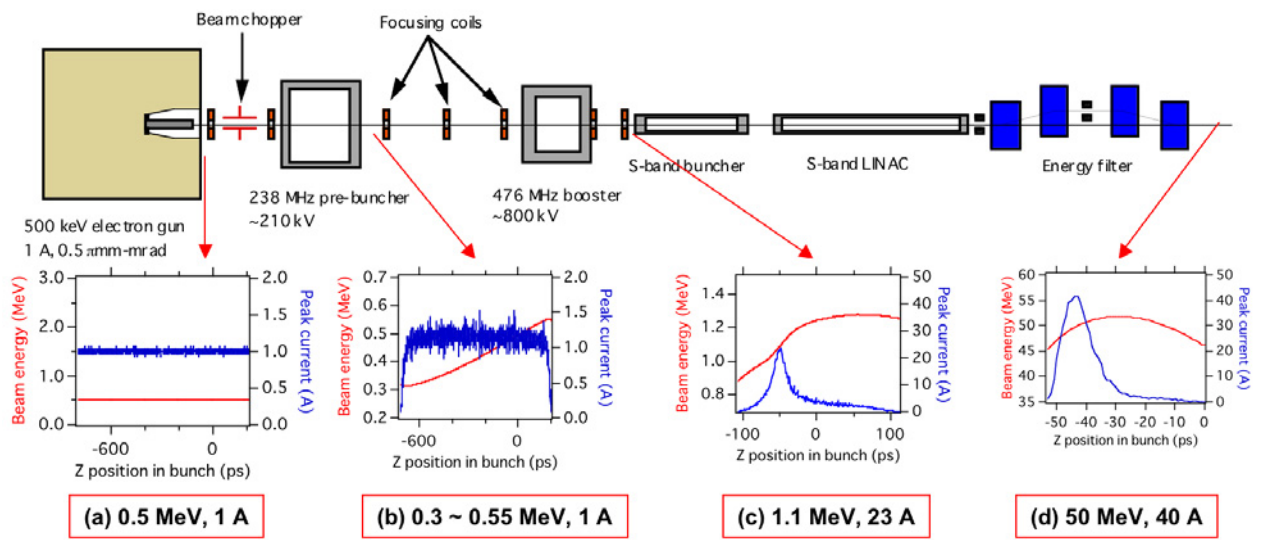


Fig. 7 Velocity bunching at the injector. Electron beam energy and bunch profile (peak current profile) are shown in red and blue lines respectively in (a) at gun exit, (b) at pre-buncher exit, (c) at S-band entrance and (d) at injector end (after energy filter).

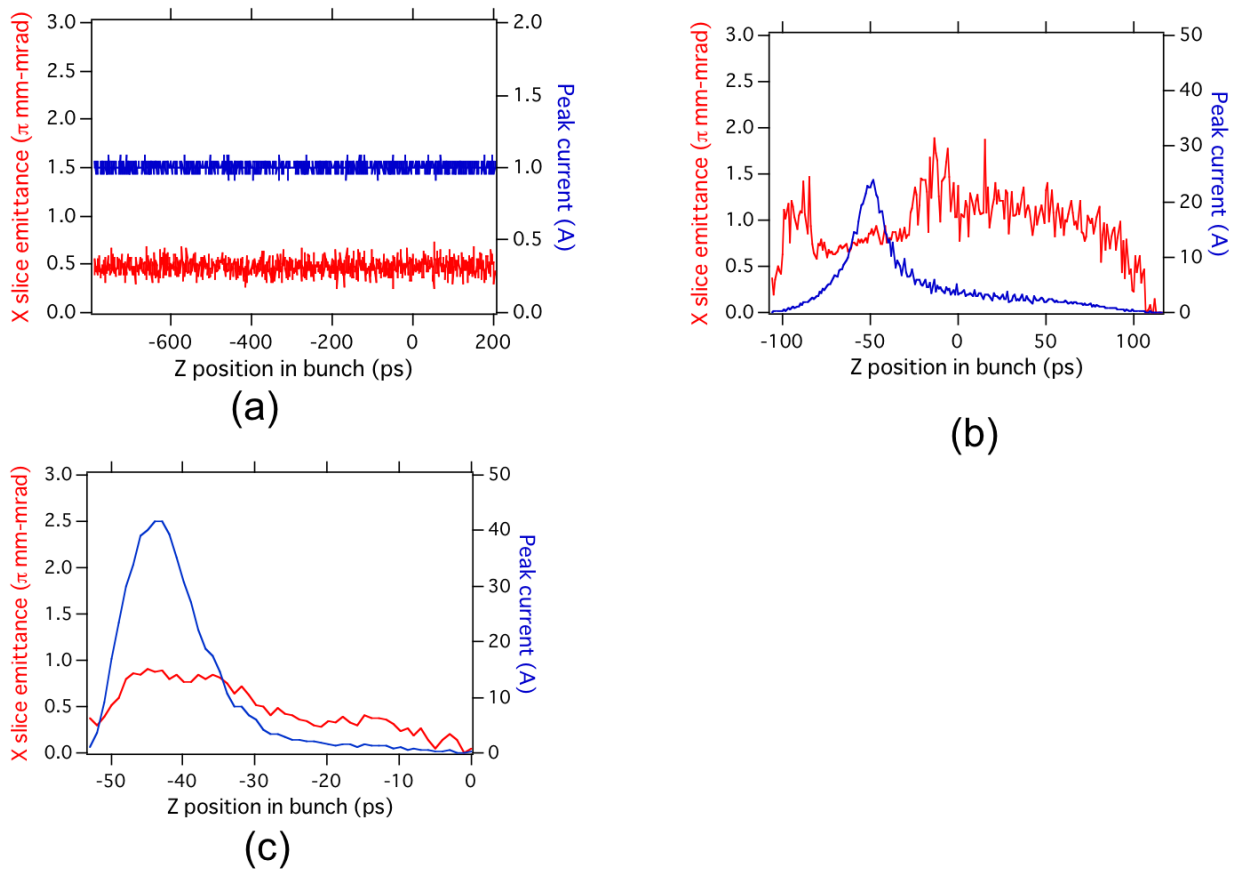


Fig. 8 Normalized slice emittance and bunch profile (peak current profile) are shown in red and blue lines respectively in (a) at gun exit, (b) at S-band entrance and (c) at injector end (after energy filter).

Radiation from undulators

The final electron beam emittance, peak current profile and longitudinal beam energy distribution at the entrance of the undulator section are shown in Fig. 13 (a) and (b). In order to estimate the SASE radiation, a center part of the electron bunch, which is shown in blue in Fig. 13 (b), is sliced out and used for the calculation of the SASE radiation. The slice parameters of this center part of the electron bunch is summarized in table 1.

Figure 14 is the simulated evolution of the SASE radiation using the transverse electron beam distribution contained in the blue part of Fig. 13 (b). The SASE radiation is calculated in a time independent mode. From Fig. 14, the expected saturation length is 80 ~ 100 m including the space between the undulator segments.

REFERENCE

- [1] M. Xie, Proceedings of PAC 1995, p. 183.
- [2] Y. Kim, private communication.
- [3] Y. Kim et al., Nucl. Instr. and Meth., A528 (2004) 421.
- [4] Y. Kim et al., "Start-to-End Simulations for PAL XFEL Project", Proceedings of FEL 2004.

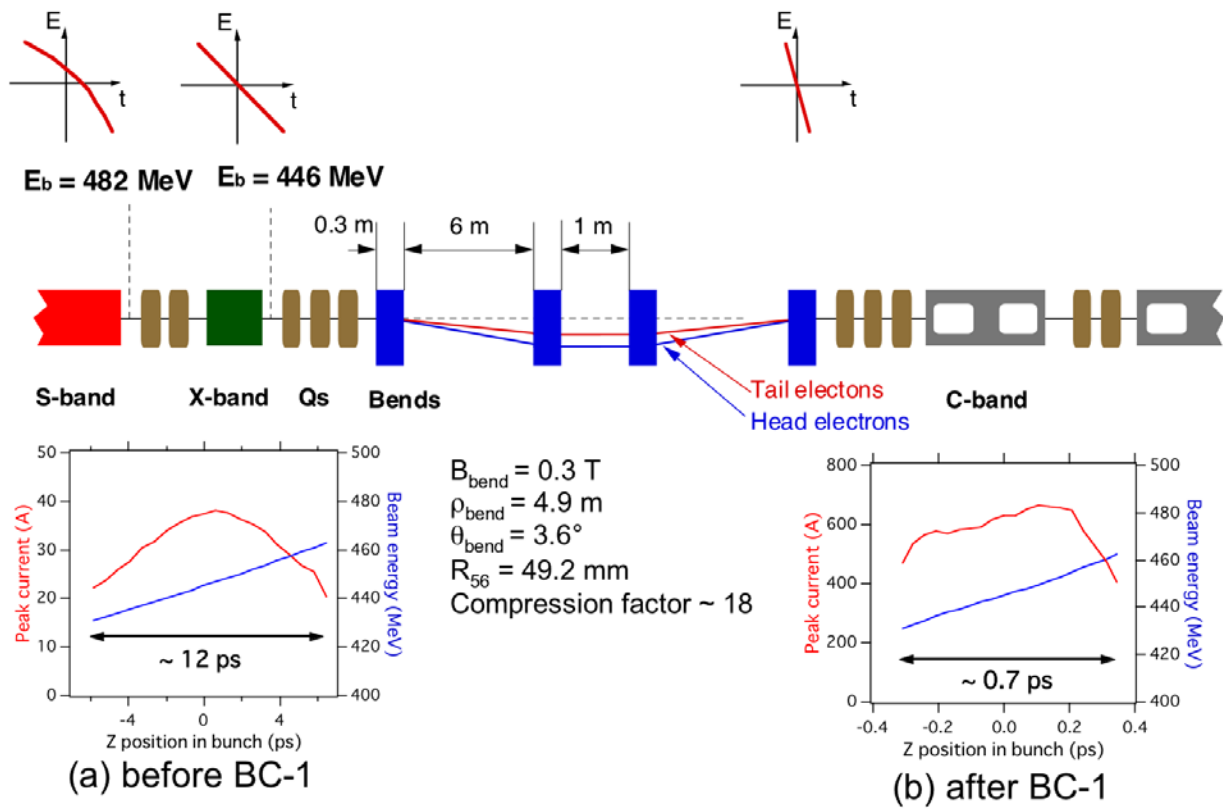


Fig. 9 Schematic layout and parameters of the first bunch compressor (BC-1). (a) and (b) are the electron bunch profiles before and after the BC-1 respectively.

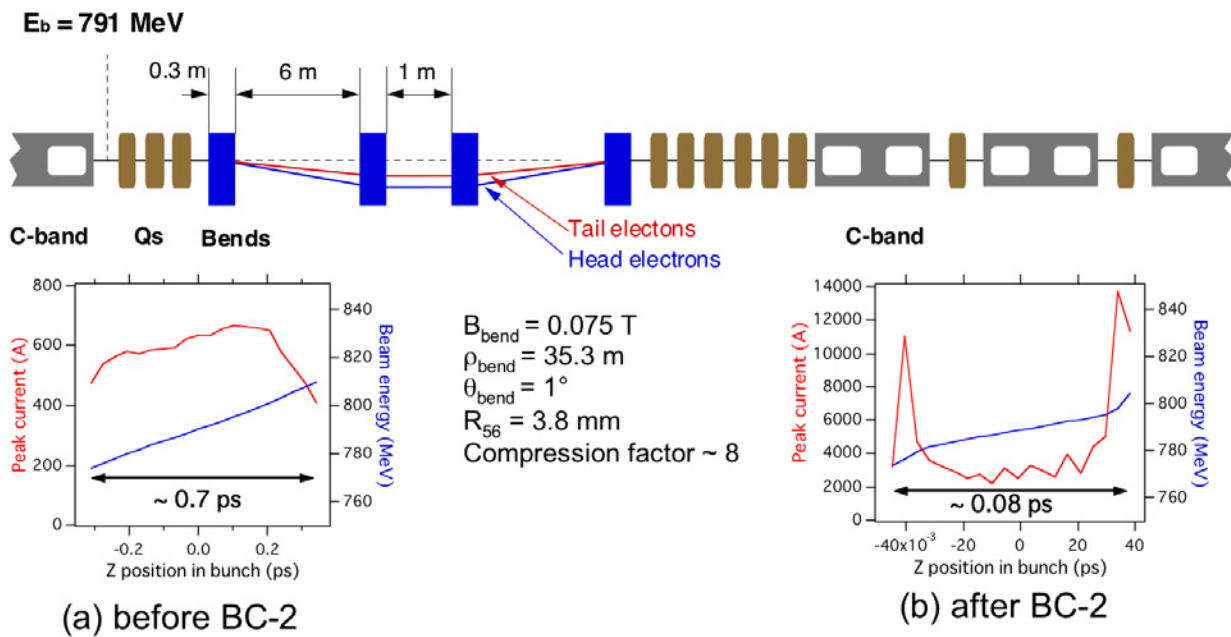


Fig. 10 Schematic layout and parameters of the second bunch compressor (BC-2). (a) and (b) are the electron bunch profiles before and after the BC-2 respectively.

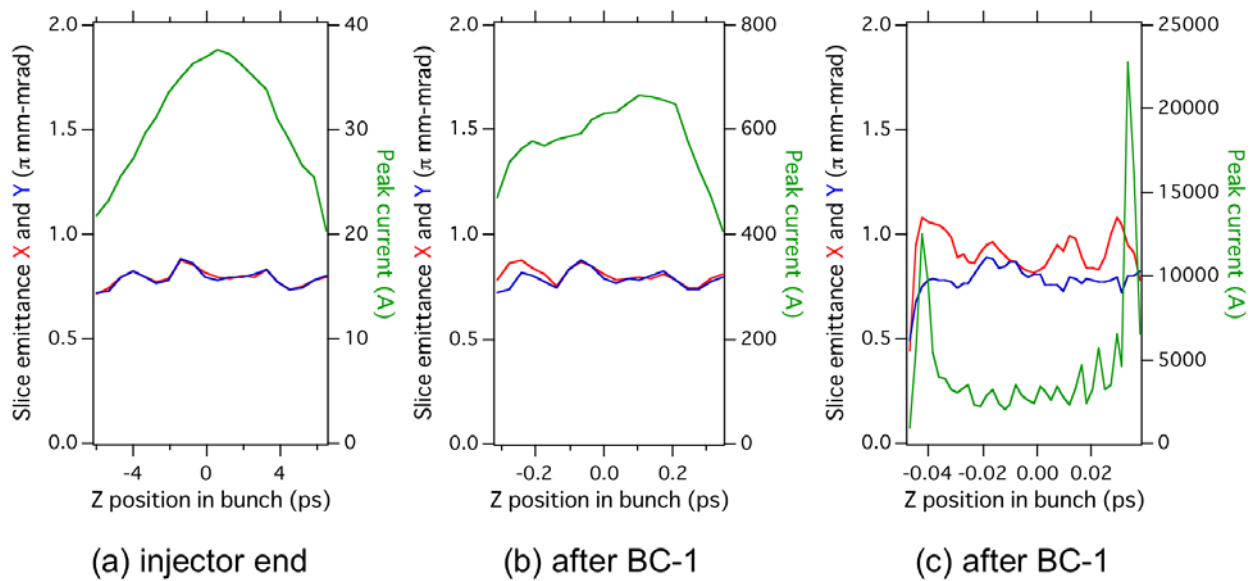


Fig. 11 Variation of normalized slice emittance at the two BCs, (a) at the injector end (~ 50 MeV), (b) after the first BC (~ 450 MeV) and (c) after the second BC (~ 800 MeV). Horizontal and vertical emittances are shown in red and blue lines respectively.

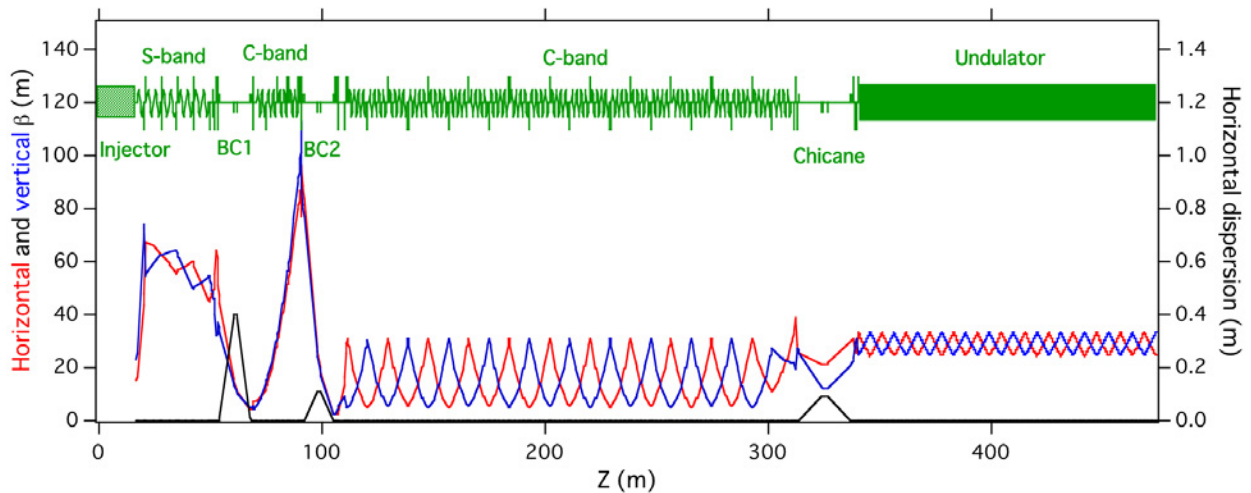


Fig. 12 Electron beam lattice of the 6 GeV accelerator, horizontal and vertical beta functions and horizontal dispersion are shown in red, blue and black lines respectively.

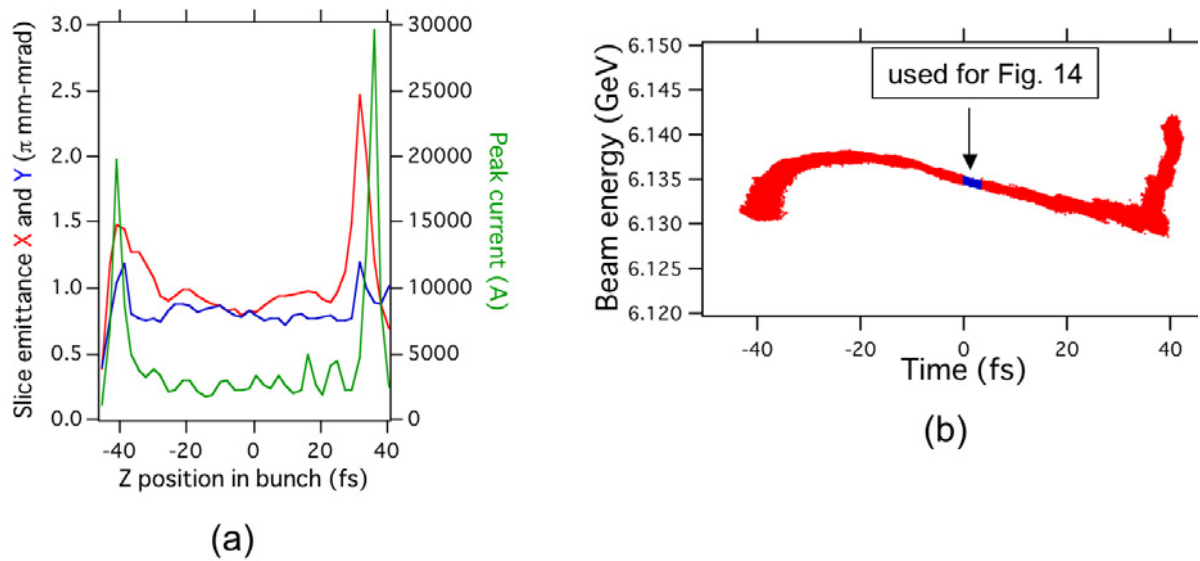


Fig. 13 Electron beam parameters at the entrance of the undulator, (a) normalized slice emittances (horizontal in red, vertical in blue) and peak current profile (in green), (b) longitudinal beam energy distribution are shown in red, blue and black lines respectively.

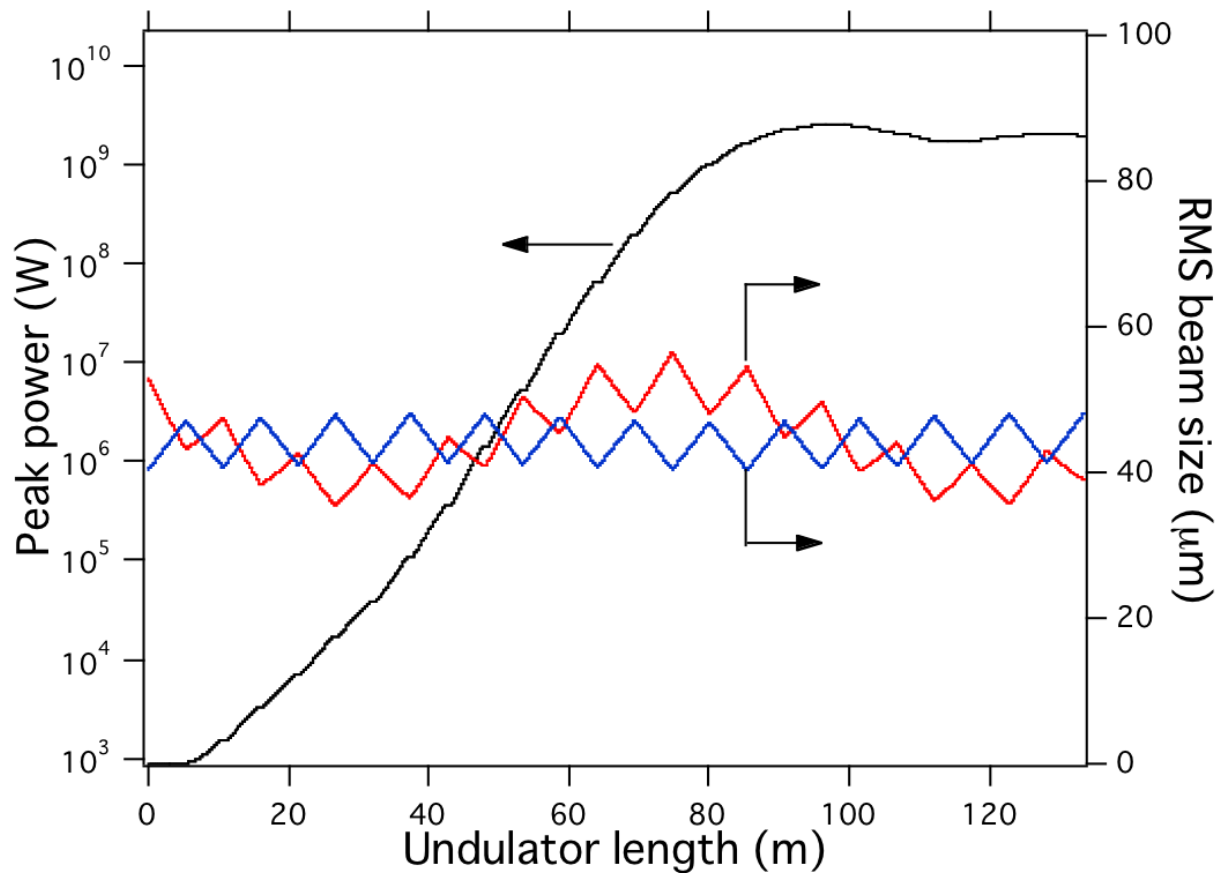


Fig. 14 Evolution of SASE radiation (in black) emitted from the blue part in Fig. 13 (b). Calculation is done in a time independent mode. Horizontal and vertical RMS electron beam sizes are shown in red and blue lines.

ELECTRON INJECTOR

In order to operate X-ray FEL in saturation region, the electron injector system is required to produce a very stable beam with low slice emittance (0.85π mm.mrad) and high peak current (40 A). We decided to use a thermionic high-voltage gun using a single-crystal CeB₆ cathode. Recently, a prototype gun was constructed and the normalized rms emittance of 1.1π mm.mrad has been experimentally demonstrated. This result is very hopeful for the X-ray FEL. In this section, we describe the design of the CeB₆ gun and the injector system.

CHOICE OF THERMIONIC GUN

In the X-ray FEL theory, it is well known that the quality of the internal structure of the bunched beam dominates the FEL gain, that is, the sliced emittance of the beam should be very low and the peak current should be of the order of kA to saturate SASE-FEL. Moreover from the FEL application point of view, the FEL light should be stable for long periods of operation.

Because the electron beam generated by the gun is directly injected to the long undulator and generates X-ray beam, any fluctuation of the electron bunch in transverse position, timing, size, charge, etc., will directly affect on X-ray lasing. This situation is quite different from the storage ring type machine. Therefore, to produce a stable X-ray FEL light, the stability of the electron gun is essential.

As we know well, the rf-photocathode gun has a big advantage to generate a short bunch with high peak current from the cathode directly. The rf-photocathode gun has been well studied and advanced recently. Using an emittance compensation solenoid, the emittance below 3π mm.mrad at 0.3 nC charge has been demonstrated [1]. However, the beam parameter is very sensitive to the conditions of the laser pulse and the photocathode surface. Generally speaking, the laser system introduces additional fluctuation source of the system. And, it is not easy to make and keep the uniform quantum efficiency of the photocathode, because it is very sensitive to vacuum and a dark current in the rf-cavity. A lot of efforts will be needed to stabilize these items.

For this reason, we decided to use a thermionic cathode followed by a buncher system [2]. The overall layout of the injector system is shown in Fig.

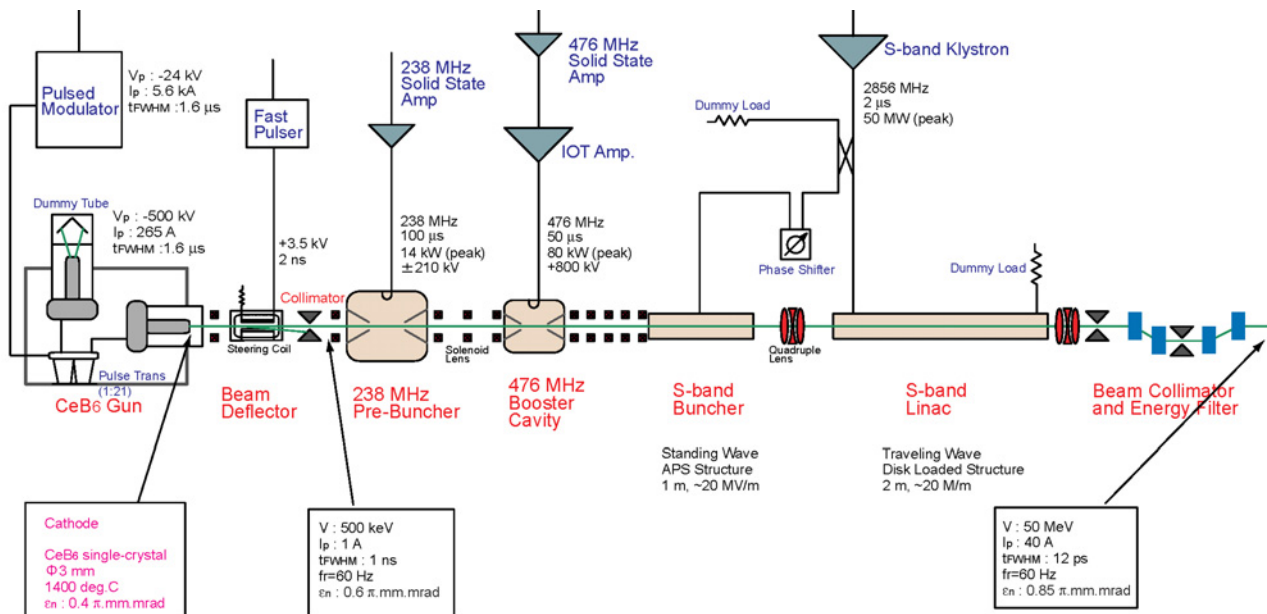


Fig. 1 : Injector system using thermionic cathode.

1. Basically, this is a traditional injector system for many types of electron accelerators. The stability and long lifetime has been well accomplished in the present injectors, however, the typical emittance is $\sim 30\pi$ mm.mrad or larger. In order to make the emittance low, we have added the following upgrade.

1) Small size cathode. The initial emittance of the gun dominates its cathode size. We use a single crystal CeB_6 cathode with 3 mm diameter. Theoretical emittance is 0.4π mm.mrad at $\sim 1400^\circ C$. High beam current of >1 A can be produced from the CeB_6 at this temperature for long lifetime.

2) Elimination of a control grid from the cathode. The emittance of the traditional thermionic cathode is broken due to the electric field distortion caused by the grid mesh.

3) Applying 500 kV on the cathode. In order to minimize emittance growth due to space charge, the gun voltage must be higher. We use 500 kV pulse with a few μ sec width.

4) Fast beam deflector. To form a nsec single bunch from the long pulse generated by the gun, we use a beam deflector with a fast pulser after the gun.

5) Adiabatic bunching and acceleration. In order to minimize emittance growth due to rf-field, a lower frequency is desirable. We use a 238 MHz sub-harmonic pre-buncher, followed by a 1.6 m drift section, then a 476 MHz booster cavity raises

the beam energy up to 1.1 MeV. S-band linac system is used to accelerate the bunch to 50 MeV before C-band main linac.

The design beam parameter at the gun exit and the end of the injector system is summarized in Table 1.

Table 1 : The design beam parameter at the gun exit and the end of the injector system

Gun exit	
Beam energy	500 keV
Peak current	>1 A
Pulse width (FWHM)	1.6 μ sec
Repetition rate	60 Hz
Normalized emittance (rms)	0.4π mm.mrad
Injector end	
Beam energy	50 MeV
Peak current	40 A
Bunch Length (FWHM)	12 ps
Normalized emittance (rms)	0.85π mm.mrad

THE CeB_6 GUN

We have designed and constructed a 500 kV electron gun with a CeB_6 cathode [3]. A side view of the prototype gun with an emittance monitor is shown in Fig. 2.

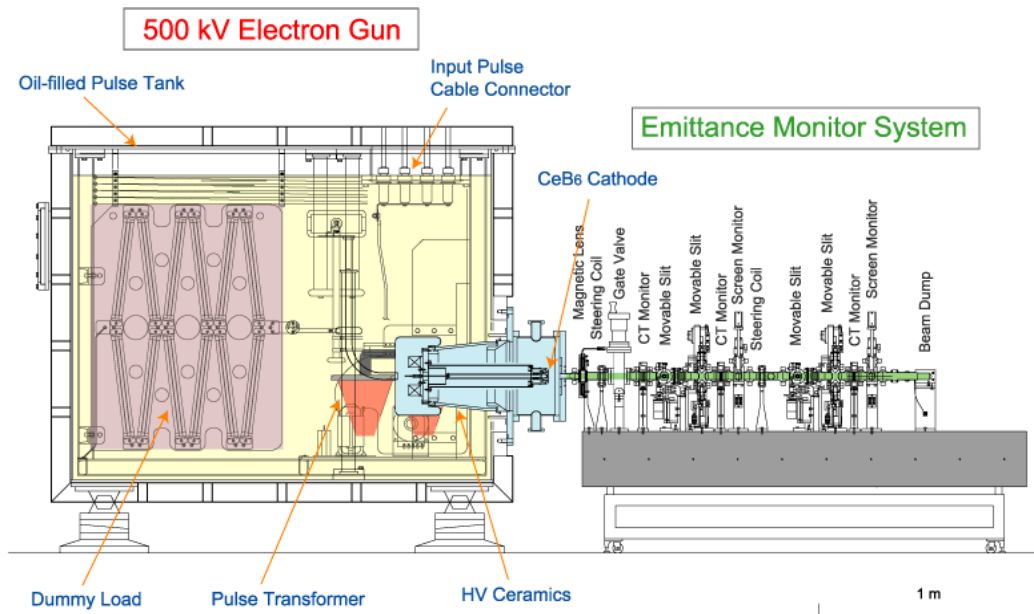


Fig. 2 : Prototype of the CeB_6 gun and emittance monitor.

CeB₆ Cathode

The normalized rms emittance of electrons emitted from a hot cathode is described by

$$\varepsilon_{n,rms} = \frac{r_c}{2} \sqrt{\frac{k_B T}{m_e c^2}},$$

where r_c is the cathode radius, k_B is Boltzmann's constant, and T is the cathode temperature. In order to obtain the required emittance of 0.4π mm.mrad at the temperature of $\sim 1400^\circ\text{C}$, the cathode diameter becomes 3 mm. On the other hand, the beam current is required to be >1 A, thus the emission density becomes >14 A/cm². Rare-earth hexaborides, that is, LaB₆ or CeB₆ can emit such a dense current for long lifetime. Recently, a single crystal CeB₆ cathode is widely used for electron microscope and the stability has been demonstrated [4]. It is reported that CeB₆ is very strong against carbon contamination compared with LaB₆. The operational temperature of CeB₆ becomes lower than that of LaB₆ because it has lower work function (~ 2.4 eV).

A single crystal is preferable to obtain low emittance. Its surface can be extremely flat (roughness ≤ 1 μm) with low porous after its material evaporation [5]. The emission density becomes uniform because the crystal direction is matched on the whole surface.

For the above reasons, we decided to use the single-crystal CeB₆ cathode with crystal face [100]. Fig. 3 shows the cathode assembly and the heating cathode in the test chamber. The CeB₆ crystal is mounted in a graphite sleeve. This produces a uniform electric field on the whole cathode surface. This is quite important for elimination of halo in beam emission from the cathode edge, which can cause damage to the undulator magnets.

We use a graphite heater rather than the conventional metallic filament made of tungsten or the like. Graphite is mechanically and chemically stable even at very high temperatures and does not evaporate like other metals. Since its electric resistance does not change much as a function of temperature, it is easy to control the heater power. The heater resistance is 0.18Ω .

A tantalum cylinder covers the graphite heater to shield the thermal radiation from its surface. A base plate of the cathode assembly is made of silicon nitride, which is mechanically strong against thermal stress.

The cathode was heated up to $\sim 1400^\circ\text{C}$ with 210 W of heater power in the test chamber (right side in Fig. 3). The reference temperature was measured at the graphite sleeve surrounding the cathode by means of a radiation monitor. We need more study to determine the cathode temperature precisely. Up to now, it has been operated for 10000 hours without failures.

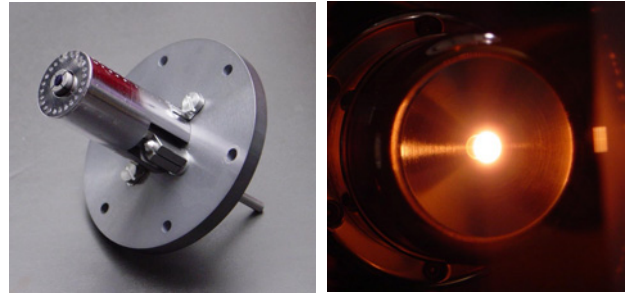


Fig. 3 : CeB₆ cathode assembly.

Accelerating Electrode

The accelerating electrode was carefully designed and manufactured because it affects the initial condition of low energy beam. We chose a flat Wehnelt rather than the common Pierce-type electrode. The reasons for this are as follows: (1) The Pierce electrode was originally designed to produce a parallel beam whose space charge field is balanced by a focusing electric field. However, if the cathode is not exactly centered due to misalignment of cathode mount or shifts in cathode position due to heating, the asymmetric focusing field acts on the beam. This may cause emittance growth. The flat Wehnelt does not have such an effect. (2) We planned to vary the beam current over a wide range in order to tune the accelerator system. The gun would be operated in a temperature limited region. The Pierce electrode is not suitable for such an operation, because at a low current, the beam is

over-focused, however, the flat Wehnelt does not over-focus the beam.

Space charge limited current is described by

$$I_{scl} = \frac{4}{9} \epsilon_0 \sqrt{\frac{2e}{m_e}} \frac{S}{d^2} V^{3/2} \cdot F,$$

where V is gap voltage, d is gap distance of the electrode and S is cathode area. In the case that the cathode radius is much smaller than d , the limited current becomes higher than that of an infinite parallel electrode. In order to take into account this effect, we introduced the enhancement factor, F , in Child's law. By performing analytical evaluation and computer simulation using EGUN code, it was found that the enhancement factor is a function of r/d . We set the gap distance to be 50 mm. In this case, F becomes 4.5 and the limited current is 10.5 A. It is much higher than the required current, namely, the cathode is operated in temperature limited region. The electric field near cathode surface becomes higher than that in space charge limited region. Since the beam near cathode is immediately accelerated, it is expected that emittance dilution due to space charge is minimized.

We performed a computer simulation for 500 keV, 1 A beam using the EGUN code. As shown in Fig. 4, the beam trajectory does not diverge much at the electrode gap. When the mesh size becomes small, the phase space plot becomes a straight line, and the emittance without initial thermal motion converges to less than 0.1 π mm.mrad below a mesh size of 0.05 mm.

The maximum field on the Wehnelt edge is calculated to be 26 MV/m at 500 kV using POISSON code. To avoid discharge problem at this high field, we carefully

manufactured the electrode. The ultra-clean stainless steel is used as the electrode's material. The surface was chemically etched and rinsed with ultra-pure water to remove the hydrocarbon contamination which causes discharge.

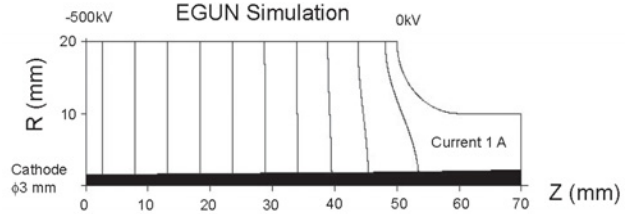


Fig. 4 : Beam trajectory at gun electrode.

High-voltage tank

Circuit diagram of the high-voltage tank is shown in Fig. 5. Basically, it follows a conventional klystron tank. Nowadays, 500 kV pulse is technically feasible in high power devices, such as X-band klystrons. We use the same model of the C-band klystron modulator [6] to feed -24 kV pulsed voltage to the high-voltage tank. The primary pulse is step-up to -500 kV by a pulse transformer, whose turn ratio is 1:21. In order to match the impedance of the gun to the modulator PFN circuit, a 1.9 k Ω dummy load is connected in parallel with the cathode. AC power for the cathode heater is fed

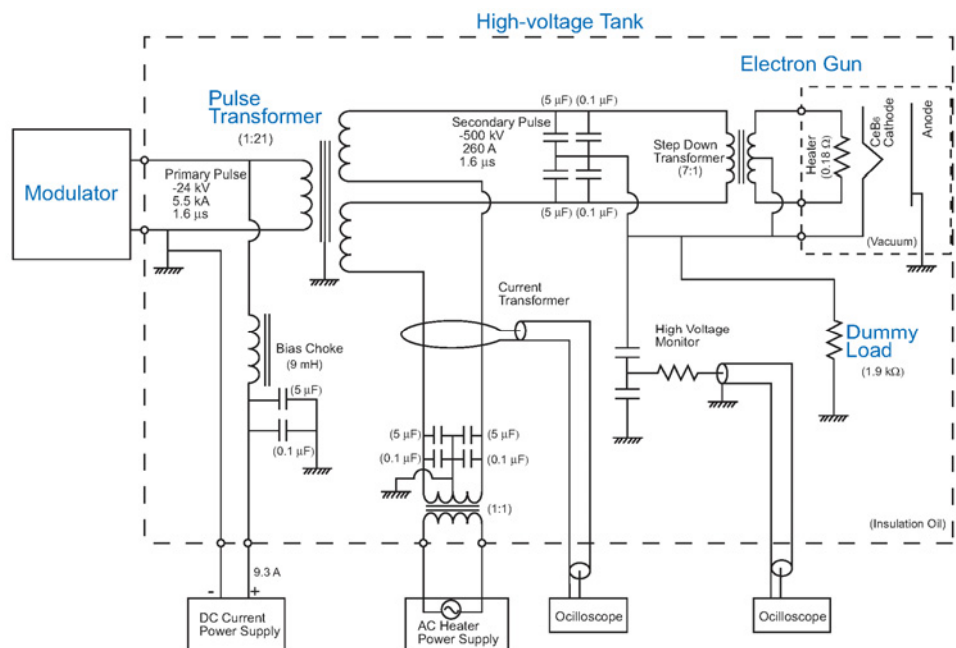


Fig. 5 : Circuit diagram of the high-voltage tank.

through the secondary winding of the pulse transformer. Since the heater current is very high (>30 A), the step-down transformer, whose turn ratio is 7:1, is used to reduce the power loss in transmission line from the power supply to the cathode .

Since we need to apply a -500 kV pulse voltage to the cathode, all the high-voltage components, namely, the ceramic insulator, pulse transformer, dummy load, etc., are immersed in insulating oil to eliminate discharge problems. Before operation, the high-voltage tank is pumped out to eliminate gases remaining in the oil and the high-voltage component .

First experimental results

We have performed the first experiment on the CeB₆ gun [7]. Fig. 6 shows the waveform of the gun voltage and the beam current. The beam current was measured by a current transformer (CT) located in the beam line right after the gun. The beam energy is 500 keV, and the peak current is 1 A. The flat-top portion of the pulse is about 0.8 μsec, which is enough to generate a 1 nsec bunch.

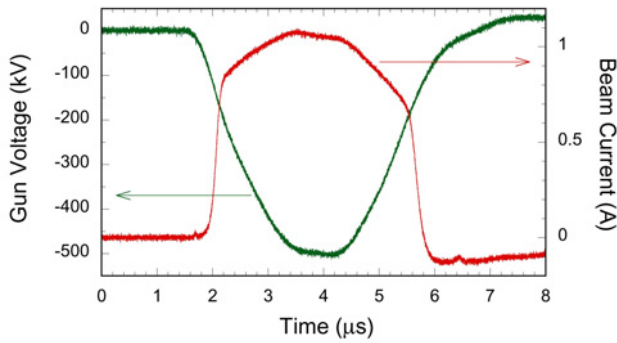


Fig. 6 : Waveform of the gun voltage and the beam current.

We measured the beam emittance by the so-called double-slits method. The upstream x-slit are located at 50 cm downstream from the cathode, followed by a 60 cm drift space and the downstream slit. Fig. 7 shows the 2-dimensional plot of the phase space profile (x-direction) measured for the 500 keV beam with 1 A peak current. The width for both the upstream and downstream slits was set to 50 μm and the scan step

was 0.25 mm for the upstream slit and 0.1 mm for the downstream slit. From the phase space profile, we analysed the normalized rms emittance, defined as

$$\varepsilon_{n,rms} = \beta\gamma\sqrt{\langle x^2 \rangle \langle x'^2 \rangle - \langle xx' \rangle^2} ,$$

where $\langle x^2 \rangle$, $\langle x'^2 \rangle$ and $\langle xx' \rangle$ denote mean square values weighted by current. The result was 1.1π mm. mrad. The beam parameter at the gun exit demonstrated in the experiment is summarized in Table 2.

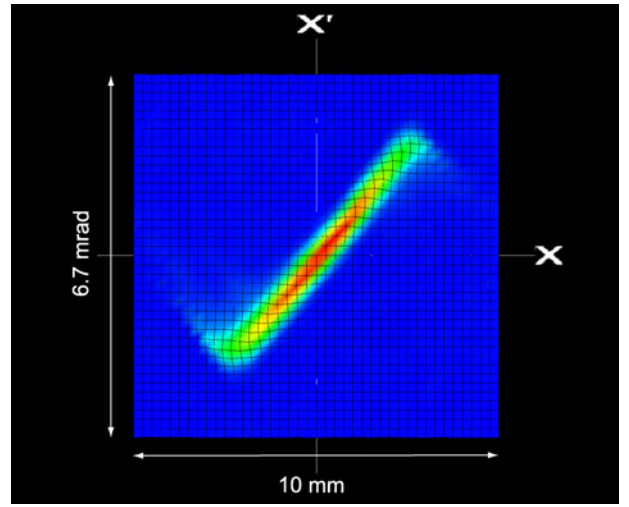


Fig. 7 : Phase space profile of 500 keV, 1 A beam.

Table 2 : Demonstrated beam parameter at gun exit

Beam energy	500 keV
Peak current	1 A
Pulse width (FWHM)	3 μsec
Repetition rate	10 Hz
Normalized emittance (rms)	1.1π mm.mrad

Improvements for real injector

Based on the experimental results, the following improvement will be done for the real injector system.

1) Emittance : We achieved very small emittance, but it was somewhat larger than the theoretical value. The small tail at the profile edge, which may be generated by the space charge effect, is a source of the emittance increase. The emittance without this tail can be roughly estimated by making the product of the rms diverging angle at the beam center (σ_x') and the rms beam radius ($\sim r/2$). The

obtained value of 0.6π mm.mrad is near the theoretical thermal emittance. Since the nonlinear tail comes from the edge part of the round beam, it can be removed using a beam collimator. We should realize the required small emittance less than 1π mm.mrad.

1) Beam current : We may need to increase the source current to satisfy the required peak current (1 A) after a collimator hole of the beam deflector, which is used to remove the beam edge. In the case that 2 A source current is needed, the increase of the cathode temperature is estimated to be $\sim 70^\circ\text{C}$.

2) Pulse width : The high-voltage pulse width became two times longer than the design value. The fairly big stray capacitance of the dummy load registers causes this long duration. As a result, the heat load of the high-voltage tank became heavy. The large size of the high-voltage tank is also determined by the registers. In order to shorten the pulse width and to make the tank compact, we are developing a dummy electron tube, instead of the dummy load register. The design of the new compact gun is shown in Fig. 8.

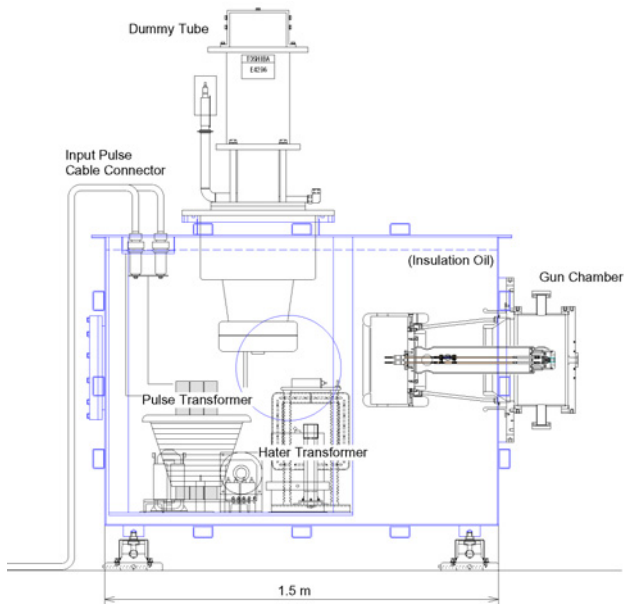


Fig. 8 : New compact gun with dummy tube.

BEAM DEFLECTOR

The single bunched beam is cut out from the long pulse by using a beam deflector and a fast high-

voltage pulser. The principle of the deflector is shown in Fig. 9. The deflector consists of two electrode plates in parallel and a steering coil. The pulser generates a high-voltage pulse (+3.5 kV) with short width (2 nsec) and fast rise time (~ 200 psec). The coil applies a horizontal magnetic field continuously in the beam line to deflect an unused part of the beam and to dump it to a collimator. At the timing that the flattop portion of the original beam pulse comes into the deflector, the high-voltage pulse is applied to the upper electrode to cancel the magnetic force, and the beam passes through the collimator hole. After the high-voltage pulse passes through the deflector plate, the beam is deflected to the dump again.

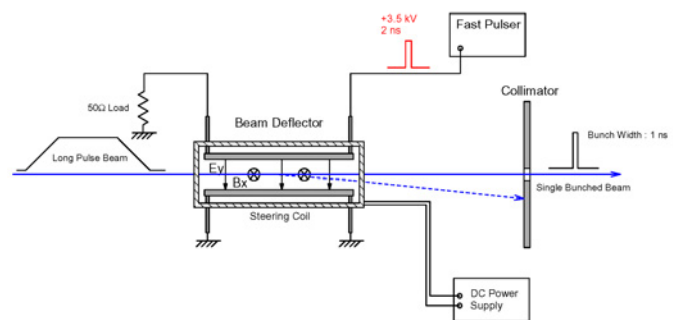


Fig. 9 : Principle of beam deflector.

The length of the deflector plates is 150 mm, and the gap is 20 mm. The magnetic field of the coil is 13 Gauss. In this case, the vertical displacement of the beam position at the collimator which located 150 mm downstream is 15 mm. It is enough large compared with the beam diameter of ~ 5 mm. We will prepare several sizes of the collimator holes to adjust the beam size. This collimator is also used to remove the beam edge which becomes the source of emittance increase.

238 MHz BUNCHER

As shown in Fig. 1, we will use a reentrant cavity for the sub-harmonic buncher. The resonant frequency is 238 MHz. The beam energy is modulated by ± 210 kV at the cavity, then the bunch is compressed after the following 1.6 m drift line.

The rf generated by the solid-state amplifier is fed through four rf couplers connected at the end plate of the cavity. The frequency is tuned precisely

by using two tuners. The dimension and the specification of the cavity is shown in Fig. 10 and Table 3, respectively.

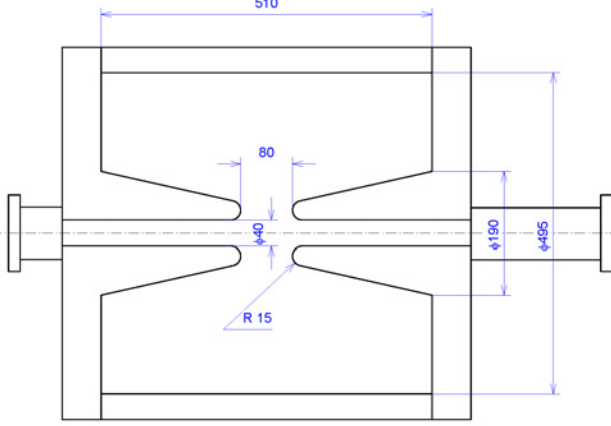


Fig. 10 : Dimension of 238 MHz buncher cavity.

Table 3 : Specification of 238 MHz buncher cavity

Frequency	238 MHz
Gap voltage	280 kV (max.)
Gap length	80 mm
Input power (peak)	14 kW (max.)
rf pulse width	100 μsec

FOCUSING LENS

The beam spreading due to transverse space charge force is given by

$$\frac{d^2 r}{dz^2} = \frac{2I}{(\beta\gamma)^3 I_0 r},$$

where I is a beam current and I_0 is Alfven current. It is obvious that the beam spreading can be dramatically reduced by increasing the beam energy. Since the beam energy of 500 keV is enough high, we decided to use some magnetic lenses to focus and transport the beam, rather than a series of big solenoid coils which is often used in conventional injectors to confine a low energy beam.

The emittance growth due to nonlinear focusing force of the magnetic field is described by

$$\Delta\mathcal{E}_{n,rms} \approx \frac{I}{96\sqrt{2}(\beta\gamma)} \left(\frac{e}{m_e c}\right)^2 \int \left(\frac{dB_{z0}}{dz}\right)^2 dz \cdot r^4,$$

where B_{z0} is longitudinal component of magnetic field on the z -axis [8]. It has strong dependence on the beam radius. In order to minimize the emittance

growth, the magnetic lens was designed so that the differentiation of B_{z0} becomes low. As shown in Fig.11, the inner diameter of the yoke is chosen to be fairly large to reduce dB_{z0}/dz . The emittance growth for this lens as a function of r is shown in Fig. 12. dB_{z0}/dz is calculated using POISSON code. This result shows that the emittance growth is negligible small for the beam with ~ 5 mm diameter.

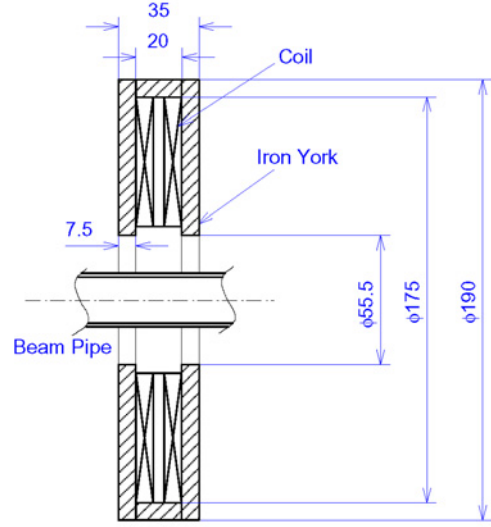


Fig. 11 : Dimension of magnetic lens.

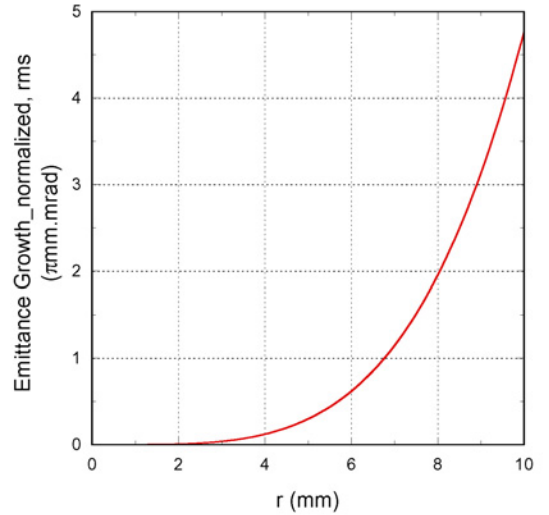


Fig. 12 : Analytical estimation of emittance growth due to nonlinear magnetic field. The plot is in the case that the center field $B_{z0}(0)$ is 825 Gauss.

BOOSTER CAVITY AND S-BAND LINAC

In order to reduce the space charge induced emittance growth of the bunched beam, the 476 MHz booster cavity is used to boost up the beam

energy from 500 keV to 1.1 MeV. A commercially available IOT-tube is used as an rf source, which generate 100 kW peak power level stably.

Before injecting the short bunch into the C-band main linac, the beam is accelerated to 50 MeV by S-band accelerator system. The first column is a standing wave accelerator with alternating periodic structure (APS). The second is a 2 m travelling wave accelerator with disk loaded structure. The rf phase between two columns is adjusted by a phase shifter located in the S-band circuit.

BEAM DIAGNOSTICS

At the end of the injector system, a diagnostic section will be prepared to monitor the beam qualities, i.e., the bunch charge, the bunch length, the energy spread, the transverse emittance etc. The beam is took off from the beam line by a bending magnet which works as an energy analyser, followed by a screen monitor. The slice emittance is measured at the screen by scanning a magnetic field of the quadrupole magnet located upstream of the energy analyser.

REFERENCES

- [1] D.H. Dowell et al., "Slice Emittance Measurement at the SLAC Gun Test Facility", Nucl. Instr. Meth. A 507 (2003) 327
- [2] T. Shintake et al., "SPRING-8 Compact SASE Source, SPIE2001, San Diego, USA, June 2001.
- [3] K. Togawa et al., "CeB₆ Electron Gun for the Soft X-ray FEL Project at SPRING-8", FEL2003, Tsukuba, Japan, Sept. 2003, to be published in Nucl. Instr. Meth. A
- [4] <http://www.feibeamtech.com/>
- [5] H. Kobayashi et al., Emittance Measurement for High-Brightness Electron Guns, 1992 Linear Accelerator Conference, Ottawa, Canada, August 1992
- [6] H. Matsumoto et al., "A Closed Compact Modulator for 50 MW C-band (5712 MHz) Klystron" 25th International Power Modulator Symposium and 2002 High Voltage Workshop, Hollywood, USA, 2002, ISBN 0-7803-7540-8
- [7] K. Togawa et al., "Emittance Measurement on the CeB₆ Electron Gun for the SPRING-8 Compact SASE Source FEL Project", APAC2004, Gyeongju, Korea, March 2004
- [8] K. Togawa, private note

C-BAND MAIN ACCELERATOR

We chose normal-conducting accelerator technology rather than the super conducting technology for the SPring-8 X-FEL machine because of its lower construction cost and ready to start construction today. The operating rf frequency is 5712 MHz in C-band, which is twice higher than the conventional S-band 2856 MHz. Since the shunt-impedance of the rf accelerating structure becomes higher at higher frequency, C-band system has superior performances than the conventional S-band (3GHz) system, and provides higher accelerating gradient as high as 40 MV/m for single bunch operation and 35 MV/m for multi-bunch, which makes the accelerator length short and the facility construction cost lower. XFEL will be operated in the single bunch mode at 60 Hz for the first phase, while the C-band system is capable to accelerate multi-bunch beam, this will be a candidate for future upgrade to multi-beam line option and higher average brightness.

BRIEF HISTORY OF C-BAND ACCELERATOR

The C-band (5712MHz) accelerator technology was firstly proposed by Shintake in 1992 [1], and developed at KEK (Tsukuba, Japan) under the R&D program in the future e+e- collider project for the high energy physics research [2].

Energy transfer efficiency of rf energy to electron energy of the accelerating structure in steady state condition can be estimated by the shunt-impedance parameter, which scales as rf frequency:

$$\eta \propto r \propto f^{0.5} \quad (1)$$

When we raise the operating rf frequency twice higher, the energy efficiency become 1.4 times better, in steady state condition (CW or long beam pulse). However, in the single bunch mode, the energy efficiency is inversely proportional to the stored RF energy per unit length, which scales as

$$\eta \propto 1/w \propto f^2 \quad (2)$$

Actual machine operation mode is in between the CW mode and single bunch mode, thus the efficiency scaling is

$$\eta \propto f^{0.5} \square f^2 \quad (3)$$

Therefore, from the efficiency point of view, higher frequency is desirable. This is the reason why C-band (5.7 GHz), X-band (11.4 GHz) or even higher 17 GHz was proposed as the drive frequency in the e+e- linear collider project. However, size of each

microwave component becomes smaller at higher frequency, and mechanical machining becomes harder. Also, to generate higher accelerating field gradient, the rf energy density becomes higher, which cause potential risk of damage in high power components. After compromising between the energy efficiency and the technical difficulty in fabrication and risk of damage, we chose the C-band (5712 MHz) as the optimum frequency.

During the R&D period (year 1996~2000), we have developed:

(1) 50 MW class pulsed high-power C-band klystron.

(2) A compact pulse power supply for the klystron, named "Smart-Modulator"

(3) RF pulse compressor using low thermal expansion material, which generates a flat output compressed power.

(4) C-band accelerating structure using choke-mode type higher-order-mode damper.

(5) C-band waveguide components (travelling-wave type ceramic window, 3 dB hybrid coupler, etc).

(6) Cavity type beam position monitor, which has high spatial resolution (~20 nm@1nC) and high center position accuracy (a few μm).

In the year of 2002, KEK C-band group jointed to RIKEN SPring-8 and started the SCSS R&D

program [3], where we continued upgrading and debugging hardware components.

In 2004, we firstly tested the C-band accelerator of choke-mode damper design with SiC loads, where we confirmed there is no serious problem up to 31 MV/m. We found rather high dark-current emission than we expected. We are currently studying the beam collimation system to eliminate the dark-current.

In 2001, the C-band R&D group for KEK-B upgrade was started separately at KEK [4]. In 2003, the first C-band accelerating structure of conventional disk-loaded design was installed in the existing KEK-B injector, and tested with beam. Accelerating gradient up to 40 MV/m was achieved and energy gain was confirmed with electron energy measurement. The system is continuously used to inject beam in KEK-B operation. In this test, frequent high-voltage breakdowns were found near the input coupler. It is believed that a sharp edge of coupling iris emits dark-current due to high-density rf current, which initiates the break-down in the main cavity. A new version is designed and under fabrication, which has rounded corner in the coupling iris.

We started collaboration with KEK-B team to share knowledge and hardware resource. This will be very important for design and construction of 6 GeV XFEL.

SYSTEM CONFIGURATION

Fig. 1 shows system diagram of one unit of C-band accelerator, and whose parameters are listed in Table-1. Two 50 MW klystrons are used in parallel, whose input rf phases are controlled by digitally to

Table-1 C-band system parameter for 6 (8) GeV XFEL.

Final beam energy at undulator	6	8	GeV
Energy gain required for C-band with 10% margin, injection energy 450 MeV 6GeV...(6000 - 450 MeV) x1.1= 6105 MeV 8GeV...(8000 - 450 MeV) x1.1= 8305 MeV	6105	8305	MeV
Active length required. 6GeV...6105 MeV / 32 MV/m = 191 m 8GeV...8305 MeV / 32 MV/m = 260 m	191	260	m
Accelerator tubes 6GeV...191 m / 1.8 m = 106.111 --> 108 8GeV...260 m / 1.8 m = 144.4 --> 144	108	144	
C-band unit 6GeV...108/4 = 27 8GeV...144/4 = 36	27	36	
Klystron and Modulator 6GeV...27 x 2 = 54 8GeV...36 x 2 = 72	54	72	
C-band Accelerator Length (80% packing efficiency) 6GeV...108 x 1.8 / 0.8 = 243 m 8GeV...144 x 1.8 / 0.8 = 324 m	243	324	m
Wall plug power for C-band accelerator 6GeV...95 kW x 27 = 2565 --> 2.6 MW 8GeV...95 kW x 36 = 3420 --> 3.4 MW	2.6	3.4	MW
Wall Plug Power per unit at 60 pps Inverter capacitor charger 35 kW x 2 = 70 kW Klystron focusing solenoids 5 kW x 2 = 10 kW Klystron heater 300 W x 2 = 0.6 kW Thyratron heater 600 W x 2 = 1.2 kW Thyratron reservoir 50 W x 2 = 0.1 kW Core Bias 200 W x 2 = 0.4 kW Control system 0.5 kW Water temp-control heater 1 kW x 5 = 5 kW Q-magnet power supply 5 kW Steering magnet 1 kW Vacuum pumps total 1 kW Total per c-band unit 95 kW			

make feed-forward type feedback on the rf pulse compressor, and generates compressed power with a flat top, which was initially designed to accelerate multi-bunch beam (80 bunches, total duration 200 nsec) in the e+e- linear collider. XFEL will be operated in the single bunch mode at 60 Hz for the first phase, while the C-band system is capable to accelerate multi-bunch beam, this will be a

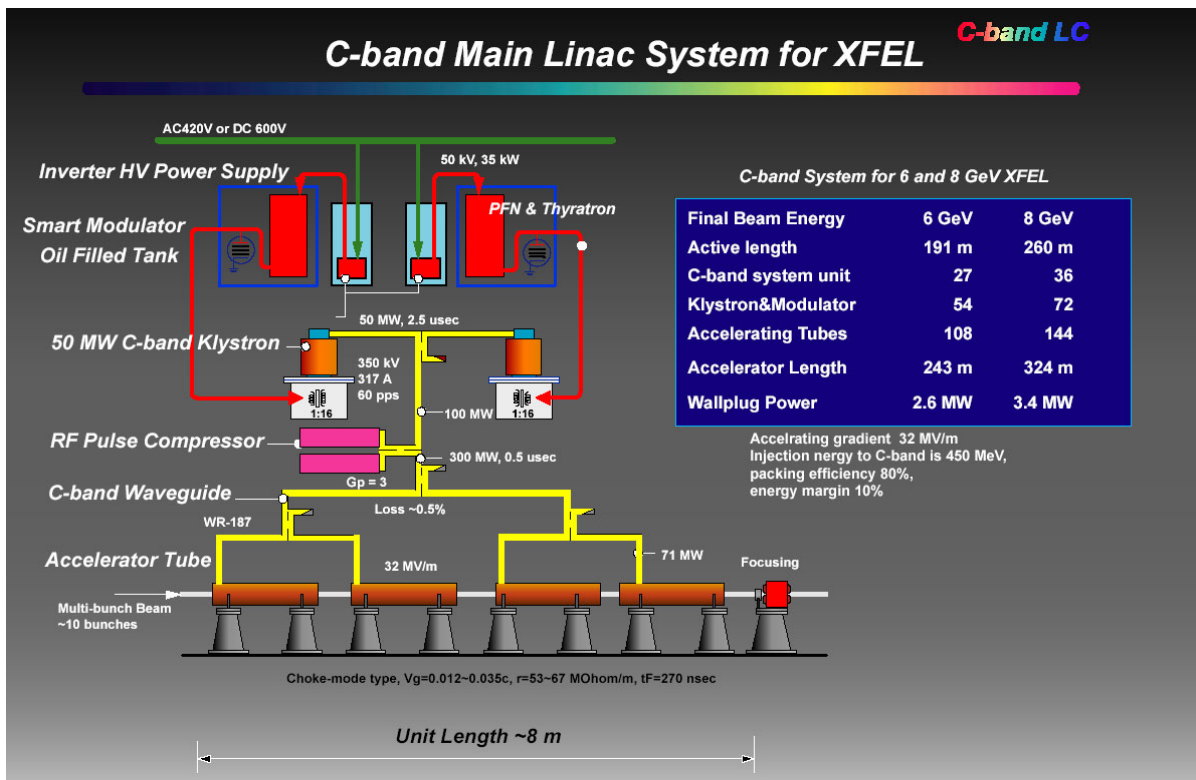


Fig. 1 C-band RF acceleration system designed for 6 GeV (or 8 GeV) XFEL at SPring-8.

candidate for future upgrading of average brightness and multi-beam line option.

As summarized in Table-I, the C-band main accelerator generate 32 MV/m for multi-bunch. For 6 GeV (8GeV) XFEL, we use 27 (36) units of this system, where 54 (72) klystron, 54 (72) modulators, and 108 (144) accelerating structure will be used.

DIFFERENT REQUIREMENTS FOR LINEAR COLLIDER AND XFEL

In the first phase R&D on C-band main accelerator for linear collider (1995~2000), the first priority was to demonstrate reliable high-power operation of the rf acceleration system. Also the energy efficiency was one of the first priority. To enhance energy efficiency the multi-bunch beam acceleration scheme was introduced, and handling technique of multi-bunch beam became an important subject, where wakefield effect and beam loading compensation were intensively studied in world wide linear collider community. According to the construction cost, it was assumed that fabrication cost will be drastically reduced by mass-production

effect and also the reliability will be increased by learning effect.

On the other hand, in XFEL the first priority is the machine stability and reliability because it will be a multi-user facility. Especially very high energy stability is required. If we realize energy stability in the order of 10^{-5} , the spectrum analysis without monochrometer becomes possible. In the today's electron linear accelerators, the beam energy stability is around 10^{-3} , which will not be enough for XFEL operation.

In the XFEL design work, we took the following subject as the first priority.

- Beam energy and intensity stability.
- Higher reliability and maintainability.
- Smaller size and lower production cost.

In SASE-FEL, the power gain is fairly small, thus we need a very long undulator line to saturate X-ray beam. The gain is very sensitive to beam parameter, specially, the beam trajectory in the undulator line. Accuracy requirement on the beam alignment in undulator line is only 4 μ m. To maintain the trajectory straight, electron beam position

Table-2. Inverter HV capacitor charger.

Maximum Charging Voltage	50	kV
Maximum Charging Rate	1.5	A
Average Output Power	35	kJ/sec
Peak Output Power	75	kJ/sec
Voltage Regulation /1 minute	0.12	%
Power Efficiency	85	%
Power Factor	0.85	

$$I_{out} = Q / \tau = CV / \tau = 1.5 \text{ A (constant current)}$$

$$P_{peak} = I_{out} \times V_{max} = 75 \text{ kJ/sec}$$

$$P_{average} = \frac{1}{2} CV^2 / \tau = 35 \text{ kJ/sec}$$

Thanks to the today's advancing IGBT solid-state technology, we can realize such power converter with small size, as shown in Fig. 2. The total size was reduced more than ten times from the traditional

monitoring and feedback, and HeNe laser alignment system will be implemented. And also X-ray beam based alignment will be used as the fine tuning. To perform these procedures, machine stability is the most important key.

The details R&D work on each hardware components will be described following sections.

HV Capacitor Charger (Inverter Power Supply)

We developed the switching inverter HV generator to charge capacitor bank in PFN (pulse forming network) of the klystron pulse power supply (klystron modulator). Fairly high peak output power is required in order to charge the PFN capacitor of 400 nF (total) up to 50 kV in 15 msec (1/60 pps = 16 msec, and 1 msec rest time), peak output power capability becomes 75 kJ/sec.



Fig. 2 Inverter type HV capacitor charger for pulse modulator for klystron and electron gun.



Fig. 3 Pulse modulator for 50 MW klystron and electron gu.

swing-charge capacitor-charging circuit having a large volume transformer and series inductor.

Table-2 shows the specification and performance of the developed inverter power supply.

Pulse Modulator Power Supply (Klystron Modulator)

The klystron modulator was the most expensive and troublesome part among all hardware components in the pulse electron accelerator. Traditional modulator design was

- Large size.
- Large EM noise source.
- Requires large amount of cooling air, blow fan (sometimes short-life).
- Accumulated dust on HV parts cause leakage current, and discharge.
- Humidity in air cause HV leakage current.

In order to solve these problems, we employed metal shield box installed all HV components and filled with insulator oil. With this design,

- Smaller size W1.7 m x D 1.2m x H 1.2 m
- Good EM shield. Metal enclosure forms,
- No cooling air is required. Heat is removed by insulation oil and cooling water pipe.
- HV circuit is perfectly shielded from the humidity and dust.

Figure 3 shows the klystron modulator, whose tank is made by stainless panels commonly used in the standard water supply. All HV components are suspended to the top flange, as shown in the figure. For maintenance, by simply lifting up the top flange we may access to the circuit components.

To realize this scheme, we have checked reliability of all HV circuit parts: the HV capacitor, thyatron, diode, resistor, cable and sockets. Especially the thyatron is the most unreliable component, thus we have carefully selected tube type and triggering circuit [5].

50 MW C-band Klystron

The pulse C-band klystron has been developed under linear collider R&D at KEK collaborating with TOSHIBA Co., which is named E3746 tube, and now on the TOSHIBA's product line [6].

The klystron basic parameter is designed by scaling existing S-band klystron, such as, SLAC 5045 and TOSHIBA E3712 tubes. We assumed frequency scaling law on the handling power limit,

$$W = P\tau \propto f^{-2} \quad (4)$$

The breakdown limit of the klystron in pulse mode operation is basically limited by the following two factors.

- (1) The high voltage breakdown across the electron gun gap, and high voltage insulator.
- (2) Meltdown of copper surface of beam pipe structure due to electron collision.

The first limit can be tolerated by reducing the field gradient by enlarging cavity gap, or the HV insulator. However, the second limit is tight. To avoid feedback parasitic oscillation, we need to use small beam pipe to cut off the higher order modes. On the other hand, the tube meltdown limit is given

Table-4 C-band 50 MW klystron parameter (TOSHIBA E3746).

Peak rf output power	50	MW
Beam to rf power efficiency	46	%
Nominal pulse length	2.5	μsec
Max. pulse repetition frequency	60	Hz
Electron gun voltage	350	kV
Electron beam current	316	A
Beam micro-perveance	1.5	$\mu\text{A}/\text{V}^{1.5}$
Number of output cavity	3	cell
Number of output ceramic window	2	Parallel

by surface density of energy deposition in one pulse. From these conditions, we find the scaling law on the power handling capability in pulsed klystron as Eq. 4.

Higher frequency klystron has lower power capability. By scaling from existing klystron data at-band frequency we chose, 50 MW peak and 2.5 μsec as the basic parameter of our C-band klystron. Table-3 is the parameter list of the developed C-



Fig. 4 TOSHIBA 50 MW C-band klystron.

Table-5 RF pulse compressor.

Cavity dimension.	153Dx430L	
RF Mode	TE _{0,1,15}	
Q-factor	180	x10 ³
Compression factor	5	
Power gain for flat pulse 200 nsec ramping for beam loading compensation 250 nsec for multi-bunch beam	3.1	
Peak output power	300	MW
Power efficiency	60	%

band klystron (TOSHIBA E3746). We designed the gun voltage at 350 kV, which is quite safety number in the high voltage breakdown point of view, and also in the power supply design. Since 1996, more than ten tubes of this design have been developed and used in high power test stands at C-band linear collider R&D, Super-KEK-B, and SCSS XFEL at RIKEN. There is no trouble reported, so far, and no dead tube until now (April 2005).

As listed in Table-1, total number of 54-tubes for 6 GeV XFEL (72 for 8 GeV).

RF Pulse Compressor

In the linear collider R&D, to accelerate multi-bunch beam train, beam loading compensation inside the train was required. In the C-band design, digital phase-modulators were implemented at the klystron input. The phase modulation was converted to amplitude modulation by combining two klystron

powers as shown in Fig. 1, then fed into the rf pulse compressor. The rf pulse compressor possess three energy storage cavities in series in each arm, and generates a flat pulse output with ramping waveform for beam loading compensation.

Three-cavity design was introduced to improve energy efficiency. However, in XFEL, machine scale is not huge, and it is not necessary to push energy efficiency higher. To make simple the system, we chose the traditional SLED design (single cavity) for XFEL project. The parameter of the SLED type pulse compressor is listed in Table-5.

Accelerating Structure

In order to stably accelerate multi-bunch beam, we need to cure the beam instability due to the long-range wakefield in the accelerating structure. Since the electron linear accelerator uses periodic structure, this wakefield effect, specially the long range wakefield (high-Q higher order modes) does the major role on beam instability. In order to damp the HOM (higher order mode), the choke-mode structure was devised by T. Shintake in 1991 [7]. As shown in the cut view of Fig. 5, when an electron bunch runs through the accelerating structure, it generates wakefield, which propagates outward and damped with ring-shaped microwave absorber in each cell. The rf accelerating field is monochromatic, which is inductively reflected by the choke structure resonating at the rf drive frequency.

The first model of the choke mode cavity was developed for S-band frequency and tested with high power rf in 1994. With 120 MW peak input power, the beam was accelerated at 50 MV/m, where no rf breakdown was observed inside the structure [8].

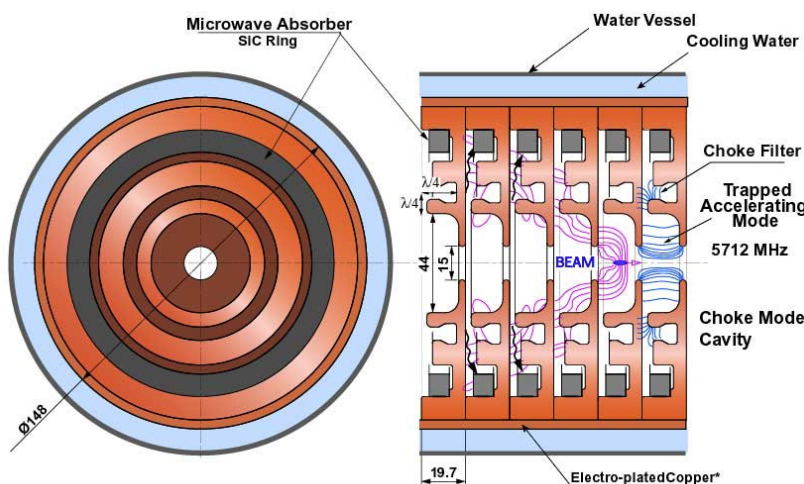


Fig. 5 The choke mode accelerating structure concept.

The first C-band accelerating structure of this type was developed in 1998 for the linear collider project, whose HOM damping performance was tested with driving-probe-beams in ASSET facility at SLAC in 1998. With this test measurement, we confirmed basic performance of the choke-mode structure[9]. There are small resonance at 18 GHz was found in the test, which was a trapped mode in the structure. To solve this resonance problem, we slightly modified cavity dimensions, and 1.8 m long structure was developed in 2002 for SCSS XFEL project as shown in Fig. 6 and Table-6.

In 2004, we firstly tested the C-band structure with high power rf in the high-power test stand at Spring-8 site[10]. We tested the structure up to 31 MV/m average accelerating gradient (limited by available power, no rf pulse compressor was used). No serious rf break down was observed during the test, and no fatal damage was found inside the structure after test. The dark current was found to be larger than our expectation, but it still allowable level if we correctly implement beam collimator in several

Table-6 C-band Accelerating structure.

Frequency	5712 MHz
Phase shift per cell	$3\pi/4$
Field distribution	semi C.G.
Number of cells	91 cell
Active length	1791 mm
Iris aperture (2a) : up-stream	17.4 mm
: down-stream	12.5 mm
Cavity diameter : up-stream	45.3 mm
: down-stream	43.3 mm
Disk thickness: t	3.0 mm
Quality factor: Q	$10.7-1 \times 10^3$
	0.3
Group velocity : up-stream	0.035 c
: down-stream	0.012 c
Average shunt impedance: rs	53-67. MΩ/m
	3
Attenuation parameter	0.53
Filling time: T _f	286 nsec

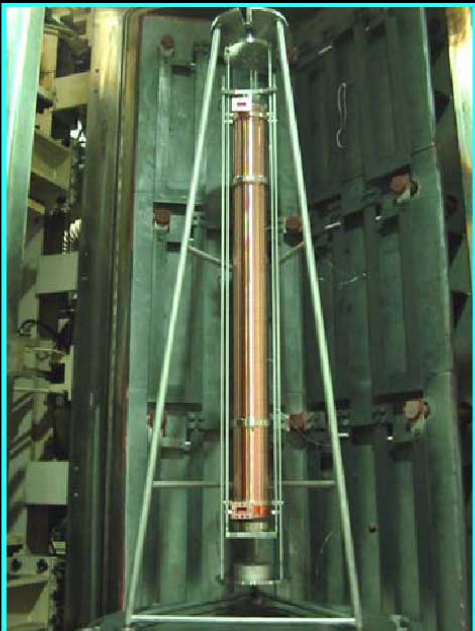
points in the main linac.

Digital RF Signal Control

As discussed in the previous section about the rf pulse compressor, to obtain the flat pulse output rf

C-band Accelerating Structure for SCSS

X-ray FEL Ver. 2002



- HOM Damping by Choke-Mode Cavity
- 1.8 m long, 91 Cells, CG-structure
- $3\pi/4$ -mode
- Brazing Bonding
- SiC by Tungsten wire-spring.
- Double-feed Coupler
- High-power test will be Summer 2003

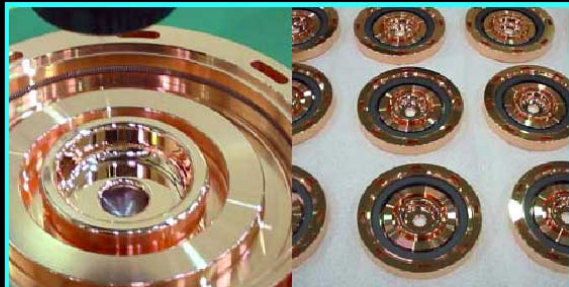


Fig. 6 C-band accelerating structure for SCSS. In each cell, the microwave absorber made by SiC was loaded to damp higher order modes.

power, we need to compensate the impulse response of the resonance circuit, which has normally a spike peak at beginning and followed by exponential decay. To do this, we apply amplitude modulation on the pulse compressor input. However, when the klystron is operated in the linear regime, i.e., not in saturated condition, the output power is very sensitive to the gun voltage, and temperature change, and also aging of cathode. In the saturated condition, it becomes very stable, and power efficient. Therefore, we apply phase modulation on the klystron input and combine two klystron outputs. When phase signs are opposite each others, a sum of two rotating vectors gives amplitude modulation.

Required speed of the phase modulation is given by time response of the system. The system bandwidth is limited by the accelerating structure. When an electron bunch passes through the accelerating structure, it gains energy from all accelerating cells,

$$V = \sum V_n \cdot e^{j\phi_n} \quad (5)$$

where V_n is the accelerating voltage in each cell. In the disk-loaded structure, rf power is fed from upstream end, and propagates down along the series of cavity chain as a slow wave structure, and reach

to the downstream end, then rest of the rf power is damped in dummy load. When the rf power reached to the downstream end, the electron beam comes. The electron runs through one accelerating structure in a few nano-seconds only, whereas it takes a few 100 nsec for rf power to fill the accelerating structure, since the rf energy propagation speed is much slower than speed of the light (0.01c~0.02c). Therefore, what electron sees is a time integration of the rf power during the rf filling time, it is 230 nsec in C-band accelerator.

For the digital modulation system, the sampling speed about ten times faster than the filling time will be enough. By taking another factor two for Shanons sampling theorem, the required sampling frequency becomes,

$$F_{sample} = 20 \times \frac{1}{230 \text{ nsec}} = 100 \text{ MHz} \quad (6)$$

The vertical resolution is defined by the required energy resolution. Most important SASE FEL application is the diffraction imaging, which requires energy resolution $\sim 10^{-3}$. When we use seeding laser injection, which will improve coherency, were energy resolution of 10^{-4} will be required. As discussed above, we have 20 samples in filling time, and electron will see the average value of those, the

required resolution is given by 20 times of 10^{-4} , i.e., 10^{-3} , which is 10 bit. By taking one bit for plus and minus sign, and one bit for a room of dynamic range (nominal peak output voltage comes 50% of dynamic range), finally 12 bit digital system is required.

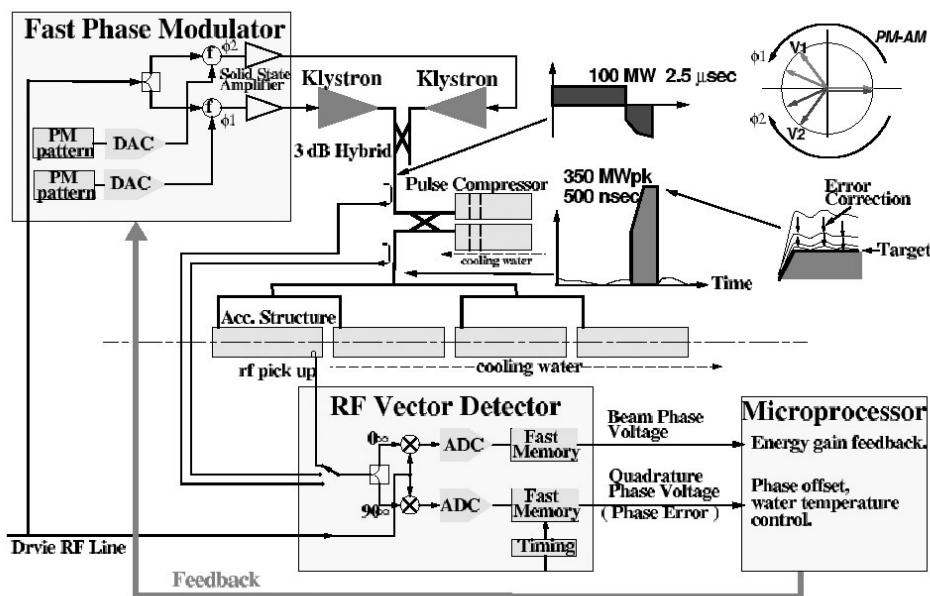


Fig. 7 Digital feed back system for C-band accelerator. By sampling rf vector voltage, DA and AD cards computes feedback and apply to the next pulse.

12 bit 128 MHz

are underdevelopment, for details refer later chapter. In order to perform feedback on successive pulses by self-learning from previous sampled data, it is required to precisely apply feedback on the same

timing in the rf pulse, to do this, the sample frequency is chosen at 128 MHz and phase locked, which is half integer of lowest rf 238 MHz in pre-buncher cavity.

REFERENCES

- [1] T. Shintake, "JLC-I", KEK Report 92-16, December 1992, A/H/M
- [2] T. Shintake and H. Matsumoto, "Results from Hardware R&D on C-band RF-System for e+e- Linear Collider", Proc. LINAC98
- [3] T. Shintake et.al, "SPRING-8 Compact SASE Source (SCSS)" SPIE, Sandiego, CA 2001
- [4] T. Kamitani et.al., "Development of C-band Accelerating Section for SuperKEKB", LINAC2004, Lubeck Germany, Aug. 2004
- [5] H. Matsumoto et. al., "A Closed Compact Modulator for 50 MW C-band (5712 MHz) Klystrons", Proc. Power Modulator Conf. & High Voltage W.S., 2002
- [6] T. Shintake et.al., "Development of C-band 50 MW Pulse Klystron for e+e- Linear Collider", PAC97, Vancouver, Canada, May 1997
- [7] T. Shintake, "The Choke Mode Cavity", Jpn. J. Appl. Phys. Vol.31, p.1567, No.11A, 1992
- [8] T. Shintake et.al., "High Power Test of HOM-Free Choke-Mode Damped Accelerating Structure, LINAC94, August 21, 1994, Tsukuba, Japan
- [9] T. Shintake et.al., "The First Wakefield Test on the C-band Choke-Mode Accelerating Structure", PAC99, March 29 - April 2, 1999, New York City, New York
- [10] T. Inagaki, "High Gradient Test of the C-band Choke-Mode Type Accelerating Structure (In Japanese)", Proc. of 1st Accel. Society of Japan 2004

UNDULATOR LINE

The undulator line is that section of the SCSS accelerator that actually produces the intense X-ray beam of the FEL system; it is composed of undulators, beam position monitors (BPMs), steering magnets, and quadrupole magnets. After being accelerated to 6 GeV by the main linac, the electron beam is injected into the undulator where the SASE process takes place. The undulator consists of 18 segments each 4.5 m long, between which the other components are installed. The electron beam is focused by the quadrupole magnets to preserve optimum betatron functions over the undulator line. The electron trajectory is monitored by the BPMs and corrected by the steering magnets so that trajectory error does not degrade the FEL amplification.

UNDULATOR

The SCSS undulator consists of 18 segments, each of which is 4.5 meters long. In contrast to the way undulators are typically used in synchrotron radiation facilities, the magnet gap will not be scanned to change the photon energy, but rather be fixed at a nominal gap (~3.5 mm). With a fixed gap, the injected electron energy will be varied to tune the photon energy. Nevertheless, the gap can be opened and closed since a variable gap positioning system is necessary for several operating utilities, and is moreover necessary to allow a full-open state for the initial commissioning of the electron beam and mechanical alignment of the beam position monitors (BPMs) using the optical laser light. The undulator parameters are summarized in Table 1.

Table 1: Main Parameters of SCSS Undulator

Periodic Length		15 mm
Length/Segment		4.5 m
Number of Periods		300
Gap	Minimum	25 mm
	Nominal	3.5 mm
	Maximum	2 mm
K Value	Maximum	1.8
	Nominal	1.3
Magnet Material		NdFeB

A prototype undulator segment with the parameters as given above has been constructed and tested [1]. The undulator mechanical structures and

magnetic properties are reported in the following sections.

Mechanical Frames

The mechanical frame is composed of 4 units, each of which supports the top and bottom iron I-beams holding the magnet jaws. Two stepping motors drive the top and bottom I-beams independently, which enables vertical centring for the on-beam alignment of the undulator. The linear vertical motion of each I-beam is transmitted by 8 ball screws driven by the stepping motor, by varying the screw starting positions, both vertical position and tilt along the longitudinal direction can be set independently for each unit. The beam elevation above the floor level of the SCSS accelerator is designed at a rather low 800 mm in order to minimize component mechanical vibration and position drift. Thus, the SCSS undulator is required to have a more compact structure than that of more standard undulators such as used in the SPring-8 storage ring.

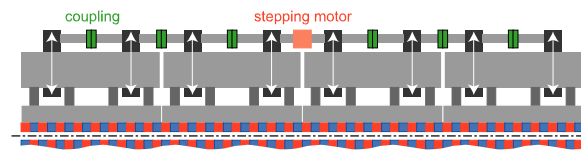


Figure. 1 Schematic Illustration of SCSS undulator mechanical structure

In-vacuum Structure

Because of the short length of the magnetic period, a very narrow gap is needed to obtain sufficient

magnetic field strength. An in-vacuum structure where the magnetic arrays are placed inside the vacuum chamber can provide a narrower gap than the conventional outside-vacuum structure, because there is no vacuum chamber between the magnet gaps. But it is also important for SCSS project that a wide vertical aperture (25 mm) can be realized by fully opening the magnet gap. This will help with the initial commissioning of the electron beam in the undulator line. In addition, a laser light beam can be passed through entire undulator line (~80 m in total), this will help with the necessary precision fine mechanical alignment of the BPMs installed in the undulator line.

Because of the in-vacuum structure, the magnet blocks would be exposed directly to the electron beam if no countermeasures were taken. Therefore, the magnet surface is first covered by a thin metal foil made from copper to reduce the resistive wake fields which will be described later. In addition, the copper foil has a nickel plating thus providing an attractive force between the magnet blocks and the foil; this improves thermal conductivity for reduced heat deposition in the foil.

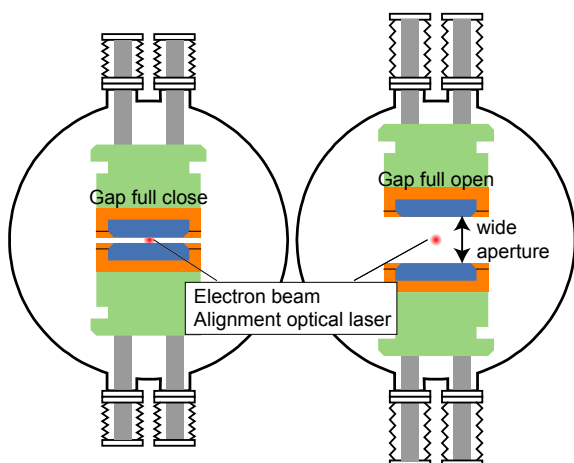


Figure 2: Cross sectional view of the in-vacuum structure of the SCSS undulator.

Magnetic Structure

Because they must be installed in the vacuum, out-gassing considerations prohibit the use of glue in assembling the magnets. Therefore the magnet

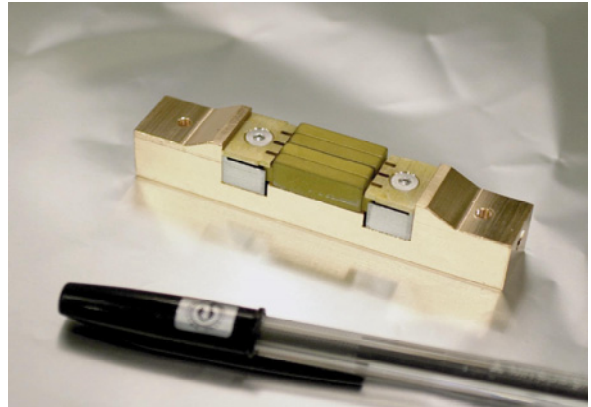


Figure 3: Photograph of a single unit of the SCSS undulator magnet.

pieces must be fixed together mechanically. However, the short period (implying thin magnet pieces) makes the clamping of each piece quite difficult (impractically small screw size). To overcome this problem, four magnet pieces are assembled in one block as shown in Fig. 3. If the usual Halbach configuration is adopted, the poles of the four magnets would be orientated as shown in Fig 4(a). However, the magnetic field that results after initial assembly of the magnet unit is usually not satisfactory. Therefore it is necessary to make trial and error changes in the assembly configuration until the resulting field satisfies the several criteria for proper undulator performance. At SPring-8, the field correction is carried out with an "in-situ sorting" technique based on rearrangement of the magnet units by flipping and swapping. However, with the Halbach scheme the allowable configuration possibilities are limited because of lack of symmetry. Instead, we have adopted a configuration of magnets with its easy axis inclined 45-degrees as shown in Fig. 4(b). The result is twice as many possibilities for flipping directions. An example magnetic field calculation for such a configuration is given in [2], it shows a slightly higher peak field is obtained when compared with the usual Halbach type even while keeping the effective K value the same. We also calculated the magnetic field from blocks with the SCSS undulator dimensions and found that the difference was very small (~3%).

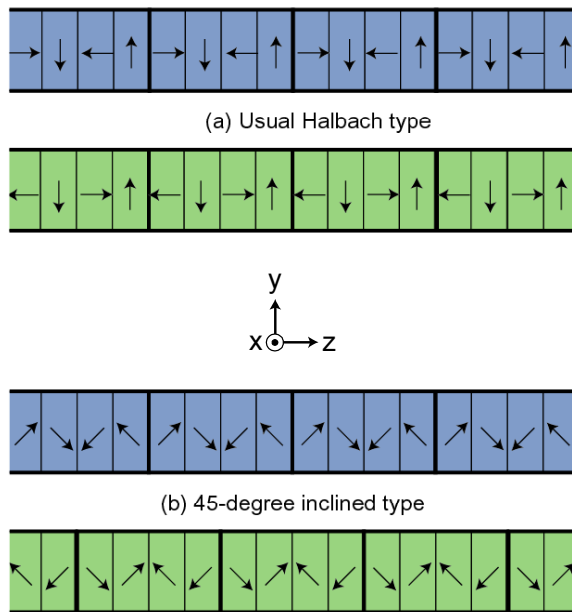


Figure 4: Two ways of assembling the four magnet blocks into a single unit: (a) normal Halbach configuration and (b) 45-degree inclined configuration providing increased symmetry.

Field Corrections

After delivery to the Spring-8 site, the beam axis vertical and horizontal magnetic fields were measured using a 1 mm thick Hall probe. The result was that the magnetic properties were found to have undesirable systematic errors induced by the gap differences between units and/or tapering within a single unit (gap misalignments). It should be noted that a precision mechanical alignment had already been performed before starting the field measurement and corrections. Thus we see that the magnetic measurement was more sensitive to the gap misalignment than the conventional mechanical position sensors used for the precision mechanical alignment. In fact, magnetic properties, especially the phase error, was found to be sensitive to even a $1\mu\text{m}$ gap misalignment. These gap misalignments were carefully corrected so that to the limits of measurability, the systematic error was completely removed.

After correcting gap misalignments, field corrections through in-situ sorting were performed. This is

the standard method for insertion device field correction used at SPring-8. The method was originally developed for field correction of the in-vacuum undulators where the common shimming technique is not allowed because the resulting uneven magnet surfaces created by the shimming would cause undesirable effects on the electron beam in the storage ring. The main purpose of the field correction is to reduce the orbit deviation and phase error. In the FEL process, the former will degrade the overlap between the photons and electrons, while the latter will affect the formation of micro bunches.

Figures 5(a) and 5(b) show the undulator properties calculated with the magnetic field measured at the initial (just after assembly) and final alignment and sorting. It is found that both the electron orbit and phase error are improved significantly. The r.m.s. phase error of 2.76 degree obtained after the final correction would make this undulator quite adequate for use as the light source in a synchrotron radiation (SR) facility. In fact, it is

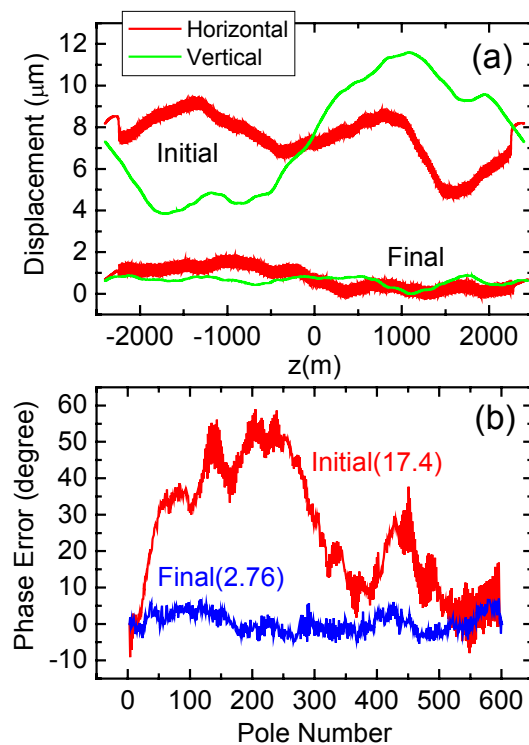


Figure 5: Results of field corrections in terms of (a) the electron trajectory and (b) phase error.

found by a numerical computation that the spectral intensity degradation is just 5% at the 5th harmonic and 30% at the 13th harmonic.

FEL Simulations

As shown in the preceding section, prototype undulator segment as constructed was found to have good magnetic performance as the light source in a SR facility, i.e., as the spontaneous-radiation source. For the next step, we need to investigate its practical performance in an FEL system. An FEL simulation code has been developed for such a purpose [3]; it can take into account the effects resulting from error components included in a practical magnetic field. Simulations were performed for the ideal error free magnetic fields and with the two different magnetic fields as measured before and after correction.

The parameters used in the simulations are summarized in Table 2. It was assumed that all the undulator segments were identical copies of the prototype segment and had the same designed or measured magnetic field distribution, so as to identify clearly the effects due to the error components of the magnetic field. The simulation results are shown in Figs. 6(a) and 6(b) in terms of the peak radiation power and bunching factor. The results show that the FEL performances obtained with the final corrected magnetic fields are nearly equivalent to those with ideal error free magnetic fields, and that the field correction has significantly improved the undulator performance as an FEL driver.

Table 2. Parameters used in the simulations.

Electron Energy	6 GeV
Peak Current	3 kA
Energy Spread	1×10^{-4}
Normalized Emittance	0.7π mm.mrad
Average Betatron Function	30 m

EFFECTS DUE TO WAKEFIELD

Wakefields are electromagnetic fields induced by the interaction between the electron beam and the

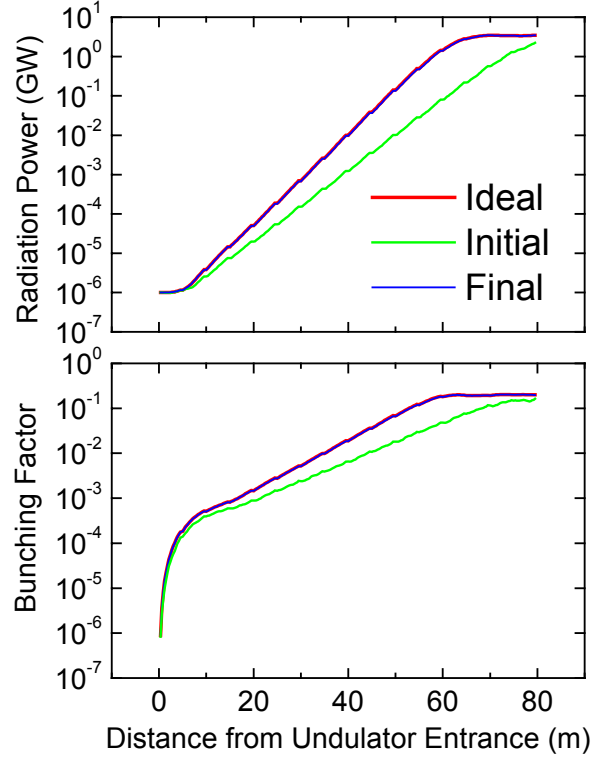


Figure 6: Results of FEL simulations to check the performance of the constructed undulator segment as an FEL driver: (a) peak radiation power and (b) bunching factor are shown as functions of the distance from the undulator entrance.

surrounding environment. Depending on the orientation of the electric field, wakefields can be classified into two types, i.e., longitudinal and transverse wakefields. The former causes an increased energy spread, while the latter causes emittance growth.

It should be noted that the emittance growth caused by a transverse wakefield only occurs when the electron beam has a transverse position offset. In other words, it can be neglected if the electron beam moves along a trajectory on the undulator axis with only small deviations (excepting sinusoidal oscillation.) We may expect that this condition will be satisfied by the beam guidance system, so that the trajectory error does not affect the FEL amplification. Thus, the effects due to the transverse wakefields can be neglected and only the longitudinal wakefields affect the FEL amplification process.

The electron beam injected into the undulator passes through a space whose narrowest dimensions are set by the top and bottom magnet arrays covered with the copper foil. Because the nominal gap distance (~ 3.5 mm) is much shorter than the width of the copper foil (~ 50 mm), it is reasonable to assume that the copper foil dominates the environment that encloses the electron beam. In such a case, we should consider two component wakefields induced by interaction with the copper foil, i.e., the resistive wall and surface roughness wakefields. While it is certainly not the case for the SCSS in-vacuum undulator, for a first approximation in order to simplify the problem, we use the analytical formulae for wakefields in a cylindrically symmetric enclosure. This should give us some order of magnitude estimates for the effect of the wakefields.

Resistive Wall Wakefield

An expression for the resistive wall wakefields generated by a point charge is analytically derived in [4] and is given as

$$W_r(s) = -\frac{4cZ_0}{\pi a^2} \times \left[\frac{\exp(-\hat{s})}{3} \cos \sqrt{3}\hat{s} - \frac{\sqrt{2}}{\pi} \int_0^\infty \frac{x^2 \exp(-x^2\hat{s})}{x^6 + 8} dx \right],$$

with

$$\hat{s} = s \left(\frac{2a^2}{Z_0\sigma} \right)^{-1/3},$$

where Z_0 is the vacuum impedance, c the speed of light, σ the conductivity of the copper foil, and s the distance from the point charge. The parameter, a , is in general the radius of the beam pipe surrounding the electron; here we will use the nominal half gap of the SCSS undulator.

Surface Roughness Wakefield

The functional form for the surface roughness wakefield cannot be expressed by a simple formula such as the resistive wakefield because the

"roughness" of the surface is essentially non-systematic random noise. In order to make a close estimate of the wakefield caused by the surface roughness, it would be necessary to measure the surface profile very precisely and then solve the Maxwell equations numerically with boundary conditions from the measured sample. In general this is a very time consuming and non-insightful calculation. Instead, Stupakov [5] has derived a quasi-analytical formula to describe the surface roughness wakefield by assuming that the surface is not like a steep mountain but rather like a gentle hill with a very slowly varying slope (small-angle approximation).

His expression for the surface roughness wakefield using the small-angle approximation is [5]

$$W_s(s) = \frac{cZ_0}{\sqrt{\pi}a^2L} \times \iint dk_x dk_z |k_z|^{3/2} |p(k_x, k_z)|^2 w(k_x, k_z, s),$$

with

$$w(k_x, k_z, s) = \frac{(2qs - 1) \cos qs - (2q + 1) \sin qs}{2s^{3/2}},$$

$$q = \frac{k_x^2 + k_z^2}{2|k_z|},$$

where $p(k_x, k_z)$ is the Fourier transform of the surface profile in the xz plane and L is the longitudinal length for Fourier transform. It is therefore necessary to measure the surface profile in order to calculate the surface roughness wakefield; and this has not yet been performed for the SCSS undulator copper foil. Lacking data, instead we assume that the surface profile consists of randomly distributed bumps. Averaging over the distribution function, the quantity $|p(k_x, k_z)|^2$ is replaced by

$$\frac{aL}{2\pi} R(k_x, k_z)$$

where R is the Fourier transform of the correlation function for the surface roughness. Assuming a Gaussian spectrum with the r.m.s. height of d and correlation length l_c , R can be expressed as

$$R(k_x, k_z) = \frac{l_c^2 d^2}{2\pi} \exp\left(-\frac{k_x^2 + k_z^2}{2} l_c^2\right).$$

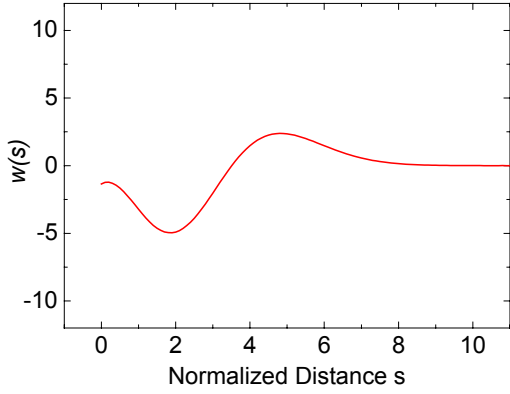


Figure 7: Function w for surface roughness wakefield as a function of the normalized distance.

Thus we finally have

$$W_s(s) = \frac{cZ_0 d^2}{8\pi^{5/2} a l_c^3} \left(\frac{s}{l_c}\right)^{-3/2} w\left(\frac{s}{l_c}\right),$$

with

$$w(\hat{s}) = \iint d\hat{k}_x d\hat{k}_z \sqrt{|\hat{k}_z|} \exp\left(-\frac{\hat{k}^2}{2}\right) \times \left[\left(\hat{k}^2 \hat{s} - |\hat{k}_z|\right) \cos \hat{q} \hat{s} - \left(\hat{k}^2 \hat{s} + |\hat{k}_z|\right) \sin \hat{q} \hat{s} \right]$$

$$\hat{k}^2 = \hat{k}_x^2 + \hat{k}_z^2, q = \frac{\hat{k}^2}{2|\hat{k}_z|}.$$

The function w dominating the surface roughness wakefield is calculated numerically and is plotted in Fig. 7. Now we can estimate the surface roughness wakefield using the above equation and the roughness height d and correlation length l_c .

Estimation of Wakefield Effects by Simulations

The resistive and surface-roughness wakefields described above cause an energy modulation in the electron bunch as shown in Fig. 8, where examples of the energy gain per unit length are plotted as functions of the position along the bunch. For calculation of each wakefield, the parameter a , or the pipe radius, has been substituted by the half gap width 1.75 mm. The correlation length l_c and r.m.s. height d to specify the surface roughness have been assumed to be 50 μm and 1 μm , respectively. Time-

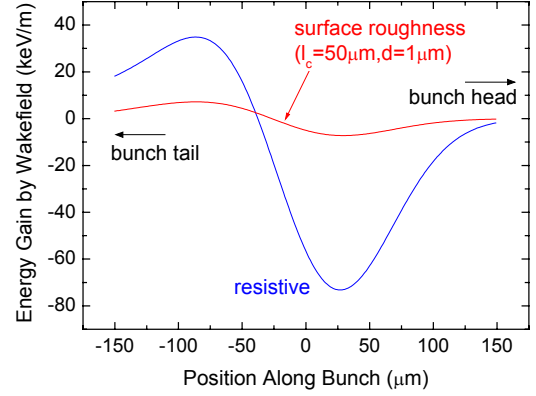


Figure 8: Examples of the energy modulation by the resistive (blue line) and surface roughness (red line) wakefields.

dependent simulations have been performed to estimate the gain degradation due to the energy modulation brought by the resistive and surface-roughness wakefields, the results of which are shown in Figs 9(a) and 9(b), respectively. In each

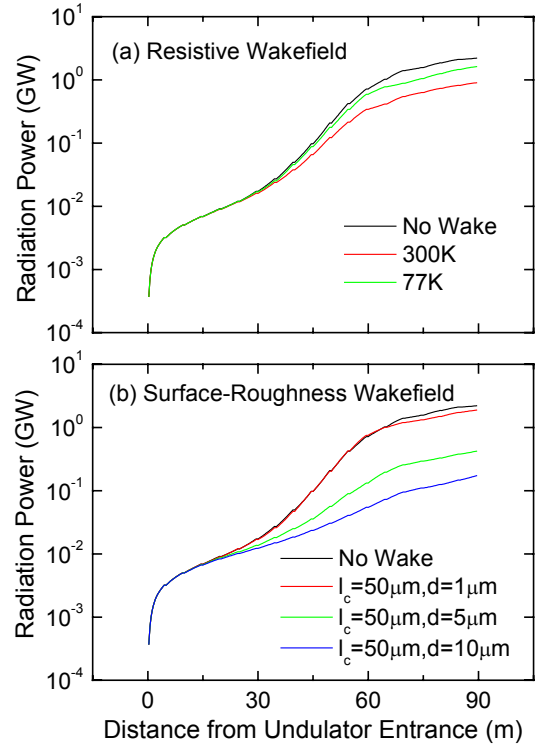


Figure 9: Results of time-dependent simulations to investigate the effects due to (a) the resistive and (b) surface-roughness wakefields, respectively.

figure, the gain curve without any wakefield effects is shown in the black line. We find that the effects due to the wakefields are not too small to be neglected. In particular, the rough surface of the copper foil to cover the magnet blocks may result in a significant gain degradation. It is therefore important to finish the surface of the copper foil as smoothly as possible. In addition, the surface profile should be measured to obtain information on the roughness.

As for the resistive wakefield, we can reduce the effects by decreasing the operating temperature of the undulator magnets. For example, the conductivity of copper at 77 K is better than that at 300 K by about one order of magnitude, which results in a significant improvement of the output power as shown in Fig. 9(a).

It should be noted that the above simulation results overestimate the effects of the wakefields because the analytical formula implemented in the simulation are those for the cylindrical enclosures. We need to evaluate the wakefields under the conditions of the in-vacuum undulator structure for more precise estimations of the effects due to wakefields.

LATTICE FUNCTIONS

The electron beam is focused by quadrupole fields while it is transported through the undulator line in order to ensure the FEL amplification process to take place. The optimum betatron function with the SCSS beam parameters is estimated at around 20 m on average. We have considered two kinds of focusing-magnet structures to achieve this condition

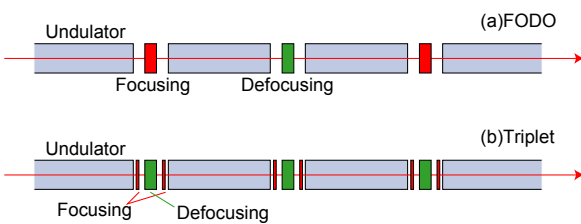


Figure 10: Schematic illustrations of two different focusing-magnet structure: (a) FODO lattice and (b) triplet quadrupole.

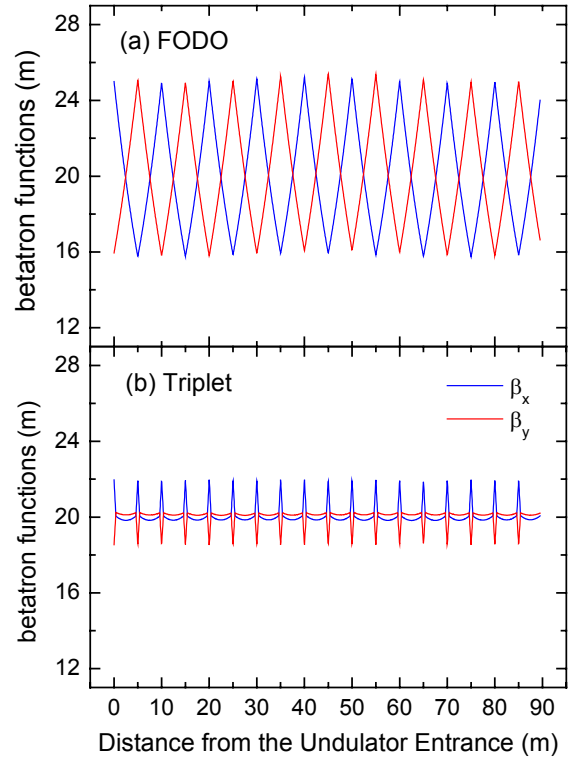


Figure 11: Betatron functions with the average value of 20 m calculated for the (a) FODO lattice and (b) triplet quadrupole magnet.

as shown in Fig. 10. One is the FODO lattice, where the focusing and defocusing quadrupole magnets are installed alternatively. The other is to install the triplet quadrupole magnets in each drift section.

The lattice functions calculated with the above two magnet structures that give the average betatron functions of 20 m in the horizontal and vertical directions are shown in Fig. 11. The integrated field gradient for each quadrupole-magnet structure are summarized in Table 2. Note that the distance between the focusing and defocusing magnets in the triplet quadrupole is assumed to be 0.2 m.

Table 2. Integrated field gradient required to achieve the average betatron function of 20 m.

	FODO	Triplet
Focusing Field Gradient (T)	1.85	6.50
Defocusing Field Gradient (T)	1.75	3.23($\times 2$)

The advantage of exploiting the triplet quadrupole is that the deviation of the betatron functions from

the nominal value of 20 m is very small in each undulator segment. On the other hand, it brings a stringent restriction on designing the quadrupole magnet because higher field gradients and longer drift sections for installation are required than that of

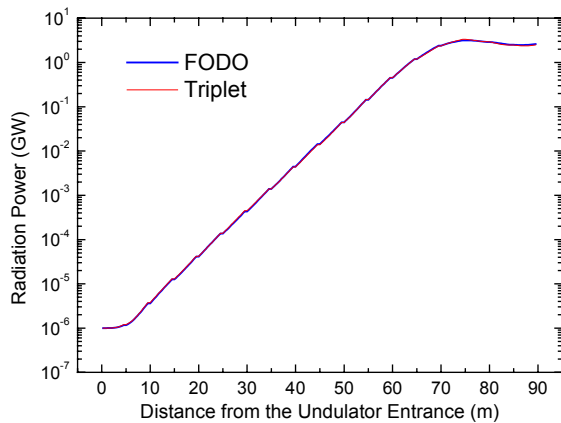


Figure 12: Results of FEL simulations with (a) the FODO lattice and (b) the triplet quadrupole.

the quadrupole magnets for the FODO lattice.

In order to determine which lattice should be chosen, we have performed FEL simulations with the two lattice functions. The results are shown in Fig. 12, where we can find little difference between the two. It is therefore possible to choose the FODO lattice without any performance degradation.

REFERENCES

- [1] T. Tanaka, K. Shirasawa, T. Seike and H. Kitamura, Proc. 8th Int. Conf. Synch. Rad. Instrum. (SRI2003), 227 (2004)
- [2] M. N. Smolyakov, Nucl. Instrum. Meth. A467-468, 207 (2001)
- [3] T. Tanaka, Proc. Int. Conf. FEL (FEL2004) to be published; see also <http://radiant.harima.riken.go.jp/simplex/>
- [4] K.L.F. Bane and M. Sands, SLAC-PUB 95-7074
- [5] G. V. Stupakov, Phys. Rev. ST-AB 1, 064401 (1998)

UNDULATOR TO EXPERIMENTAL AREA: X-RAY TRANSPORT SYSTEM

Abstract: The conceptual design of x-ray transport system at SCSS is described. Conventional designs are adopted for spatial filtering components, vacuum systems, and beam shutter. Theoretical and technological developments are progressed for fixing final specifications of components which are directly exposed in the on-axis XFEL radiation, such as mirror, monochromator, and absorber.

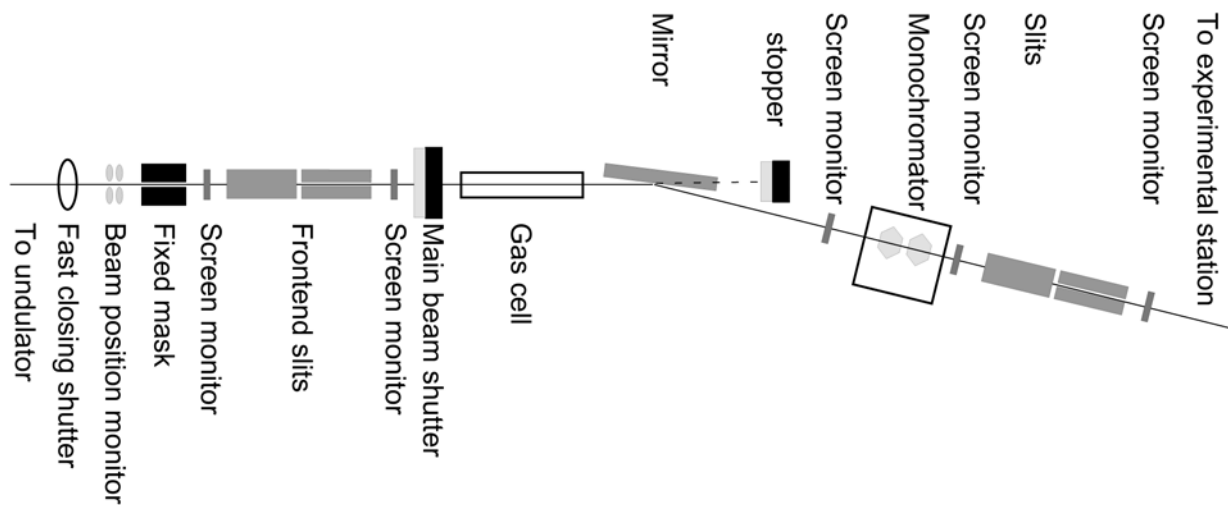


Figure 1: Schematic layout of the x-ray transport system.

GENERAL

A main purpose of the x-ray transport system is to deliver XFEL beam to the experimental station after conditioning x-rays to demand user requirements. This is realized by spatial/spectral filtering system which removes unnecessary radiation especially included in spontaneous light. The second issue is to diagnose photon beam properties (e.g. position, direction, intensity, etc.) and to provide information to the feedback system for the accelerator operation and to user experiment. Diagnostics tools for the initial commissioning are also included. The third purpose is to assure human safety. The possibility of radiation exposure should be completely eliminated by shielding, shutters, and the interlock system.

LAYOUT

In addition to usual radiation safety for x-rays, direct hit of the electron beam from the linear accelerator to the users must be avoided. Two types of the beamline layout are considered. One design is usage of a deflecting mirror. In case of an accident to the electric power of the bending magnets at the beam dump, the mirror intercepts the electron beam. In the other design, permanent magnets are set between the end of the undulator and the beam dump. The permanent magnets deflect electron beam slightly but sufficient angle so that the electron beam does not reach the beamline if the beam transport is long enough.

A schematic view based on the former design is shown in Figure 1. A front end section includes spatial filtering components and evacuation systems and terminates with a differential pumping system. A main beam shutter (MBS) follows the section. A gas

Table 1: FEL x-ray beam characteristics

FEL energy range	< 22 keV (8 GeV electron beam)
Pulse width	500 fs (FWHM)
Repetition	60 Hz
FEL x-ray beam characteristics at E=12.4 keV (6 GeV electron beam)	
Peak power	3 GW
Average power	0.09 W
Average power density	560 kW/mrad ²
Photons/pulse	7.6×10^{11}
Beam size at the source	50 $\mu\text{m}\phi$ (STD)
Beam divergence	0.40 μrad (STD)
Bandwidth	6×10^{-4} (FWHM)

cell for attenuating beam intensity is placed with another differential pumping system in the downstream. A mirror and a double-crystal monochromator (DCM) work as main optical components. Several types of diagnostics systems are used for daily operation as well as for initial commissioning.

The layout is basically applied for the latter case, with modification of the mirror section and the optical axis in the downstream of the mirror.

DETAILS

Front-end section

The front-end section is designed for removing off-axial spontaneous/thermal radiation and for keeping high vacuum condition. The total power and power density of the peripheral radiation is not so extreme. Thus the design is based on that developed for the SPring-8 undulator beamlines [1,2] except on-axis components. A sequence of fixed masks and a front-end slit gradually decreases spatial widths of the incident beam. These components are made of metals (e.g. GlidCop) in grazed angle geometry with water cooling. They are not intended to receive on-

axis XFEL radiation. Thus the minimum gap of the front-end slit should be controlled to avoid intercepting XFEL beam. The use of low-Z material may be considered for smaller gap operation. The maximum gap is determined by the aperture (\sim several millimeters) of the differential pumping system located in the downstream.

The section is directly connected to undulator chambers without any windows or apertures. Thus vacuum level under 10^{-7} Pa should be kept with ion pumping system. A fast closing shutter (FCS) is installed at the entrance of the section in order to protect transmission of vacuum trouble to the upstream. The exit of the section is connected to the downstream through a differential pumping system. Be-windows, which is widely used for vacuum separation in present x-ray beamlines, are not adopted in order to avoid unwanted modulation of beam intensity caused from inhomogeneity of the material.

Main Beam shutter

The Main Beam Shutter (MBS), which stands for a pair of a photon absorber and a beam shutter, is installed after the front-end section of the beamline.

It works to decide whether the photon beam is introduced to the transportation channel or not. The photon absorber and the beam shutter intercept the thermal and the radiational constituents of synchrotron radiation, respectively.

As shown in Figure 2, there are two paths lined up vertically inside the absorber body, which is made of copper. The upper one of the closed mode stops the photon beam, whereas the lower one of the open mode passes it through a fixed aperture. Each path will be moved on the beam axis by a pneumatic driven support on which the photon absorber is mounted. The photon beam is absorbed using popular grazed angle geometry, because an average power level on the absorber will not be problematic. The resultant absorbed power will be dissipated by cooling water. However, since the peak power density per unit solid angle is extremely huge of about 3 MW/mrad^2 , there is a possibility that we have to reconsider this design including a selection of the material considering a photon-induced damage. On the other hand, Figure 3 shows the inside of the beam shutter, which is installed downstream side of the photon absorber. The intercepting body for radiational constituent, made of tungsten, is connected to the pneumatic driven cylinder.

The mechanical motions of both components shall be linked each other by an interlock system. When the signal of closing the MBS is inputted, at first the photon absorber would travel downwards to stop the photon beam thermally. After the limit switch indicating the closed position of the absorber is activated, the intercepting body of the beam shutter would start to move on the beam axis sequentially. In case of the signal of opening the MBS, the reverse sequential movement would be operated.

A similar combination of the components is used as fixed beam stoppers located after the mirror and the first crystal of the DCM.

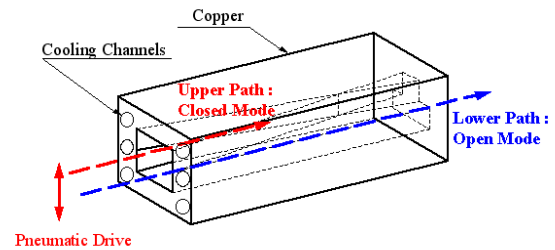


Figure 2: Conceptual drawing of the photon absorber, which intercepts the thermal constituent of the beam axis, namely intercepts the radiational constituent.

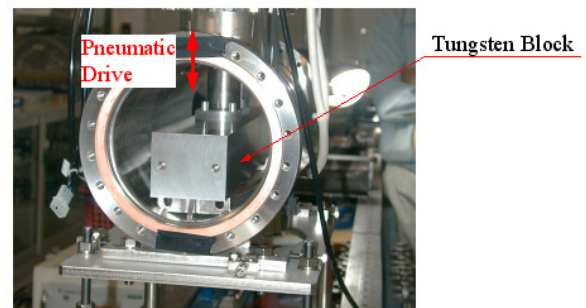


Figure 3: Internal photograph of the beam shutter. In this case, the intercepting body, made of tungsten, is set on the beam axis, namely intercepts the radiational constituent.

Beam attenuation system

The beam attenuation system is composed of a gas cell for attenuating beam intensity if necessary. Several types of gases can be introduced to the cell with controlling its pressure. The section is connected to downstream through a differential pumping system.

Mirror

A main purpose of the mirror is to eliminate high energy radiation which largely comes from higher-order spontaneous radiation. Figure error of mirror surface should be minimized to suppress unwanted intensity modulation. Ultrahigh precision technologies for figuring surface, such as elastic emission machining (EEM) and plasma chemical

vaporization machining (PCVM) [3], are quite useful for the purpose. Silicon is used as a substrate material. Coating of high-Z material is not preferable because of increasing peak dose. Theoretical study from acceptable dose is required to determine final design including coating material, incident angle, and total length.

Another role of the mirror from the viewpoint of safety is to separate paths of x-rays and electron beam accidentally injecting from the accelerator. The mirror can be removed from beam path with usage of permanent magnets, as previously mentioned.

Monochromator

The double-crystal monochromator is used when experiments need to scan the energy or longer temporal coherence than that achieved by the 6×10^{-4} bandwidth of the FEL. Otherwise the monochromator is shifted to pass the FEL beam through it. If the deflecting mirror is omitted from the beamline layout, the γ -stopper set downstream the monochromator is shifted together with the monochromator.

The monochromator crystal must be selected from the viewpoint of radiation damage and preservation of spatial coherence. Table 2 summarizes the melt limit [4] and estimated radiation dose under normal incidence for relevant materials. Considering the radiation damage and the available quality of crystal, only diamonds are suitable for the monochromator crystals. Synthetic type IIa diamonds are good candidate within several variations of diamonds [5]. However there are still problem of perfectness and size at this point. Silicon crystals might be used at higher energies than 12.4 keV, when the energy resolution of diamonds is too high. Cryogenic cooling of the crystals may be unnecessary owing to the low repetition frequency of 60 Hz at SCSS [6].

Table 2: Normal incidence peak energy dose at 50 m from the source

Material	Melt (eV/atom)	Dose (eV/atom)	
		12.4 keV	6 keV
Li	0.1	0.00005	0.0002
Be	0.3	0.0001	0.0007
B	0.5	0.0003	0.002
graphite	0.9	0.0005	0.004
diamond	-	0.0004	0.004
Al	0.2	0.01	0.1
Si	0.4	0.02	0.1
Cu	0.3	0.3	0.2

Diagnostics system

In the front-end section, a beam position monitor (BPM) is installed to measure beam position in shot-by-shot. Combination with another BPM in downstream section enables to determine beam direction.

An intensity monitor is set downstream the monochromator. The monitor must be transparent to avoid disturbing the beam coherence, and be sufficiently fast to measure the intensity shot by shot. One possible design is a combination of a gas chamber and a pin photodiode. Elastically scattered x-rays are monitored by the pin photodiode.

There are several insertable fluorescence screen monitors, which are used for check of the beam axis and rough alignment of optical components, such as the collimator, the front-end slit, the first mirror, and the monochromator. These screen monitors are used only in the alignment mode, where sufficiently weak unsaturated beam is delivered using one of the fifteen segments of the undulator. To avoid accidental exposure to the saturated beam, the screen monitors is operated through the interlock system.

REFERENCES

- [1] Y. Sakurai *et al.*, Rev. Sci. Instrum. 66 (1995) 1771.
- [2] S. Takahashi *et al.*, Nucl. Instrum. Methods A 467-468 (2001) 758.
- [3] Y. Mori *et al.*, Proc. SPIE 4501 (2001) 30.
- [4] “Linac Coherent Light Source (LCLS) Conceptual Design Report”, SLAC-R-593, SLAC, Stanford (2002)
- [5] International Workshop on “Diamond Single Crystal For 3rd and 4th Generation X-ray Sources”, ESRF, Grenoble (2004).
- [6] L. Zhang, A. K. Freund, T. Tschentscher, and H. Schulte-Schrepping, AIP Conference Proceedings 705 (2003) 639.

BEAM TRAJECTORY CONTROL AND ALIGNMENT

One of the most challenging issues in SASE-FEL machine at X-ray wavelength region is the accurate beam guiding along the very long undulator line (~80 m). In order to maintain overlap of the electron beam on the X-ray beam, the electron beam trajectory has to be kept in a very straight line. The tolerance is typically 4 micron-meter transverse for each undulator segment (4.5 m long). To achieve this accuracy, we will perform the alignment in three steps. (1) Align cavity-type electron beam position monitor (cavity-BPM) by means of HeNe laser, (2) measure electron beam position and correct error using corrector magnets, (3) By observing the X-ray radiation pattern, perform fine tuning of the beam trajectory and phase matching, which is separately discussed in the FEL commissioning part..

REQUIRED ALIGNMENT

It will be practically impossible to keep the electron trajectory in a straight line within ten micron-meters along whole 80 m long undulator line. To find realistic solution, the study of trajectory error in the undulator line was performed (see chapter of undulator line), and it was found that the followings criterion. The gain degradation by the single kick errors (SKE) effect was analytically investigated in reference [1], where it was found that a critical angle θ_c , which gives the criterion for allowable SKE to maintain a certain level of the FEL saturation power.

$$\theta_c = \sqrt{\frac{\lambda}{L_{g,3d}}}. \quad (1)$$

With the SCSS parameters, θ_c is found to be 5.5 μ rad. The trajectory slope of the electron beam in the undulator segments should be smaller than this value. Thus, the accuracy of the BPM alignment should be better than several microns.

The worst case is the zigzag trajectory as shown in Fig.1 (a), where the trajectory must be kept in a zone width less than $L\theta_c$. By FEL simulations, the allowable error on BPM alignment was found to be 4 μ m. If the single kick errors have the same polarity, the trajectory becomes a curved line as shown in Fig. 1(b). Even if the trajectory offset from an ideal accelerator axis becomes very large, we will obtain a certain amount of gain when each single kick error is smaller than θ_c . This means that we do not need to align all BPMs along a perfect

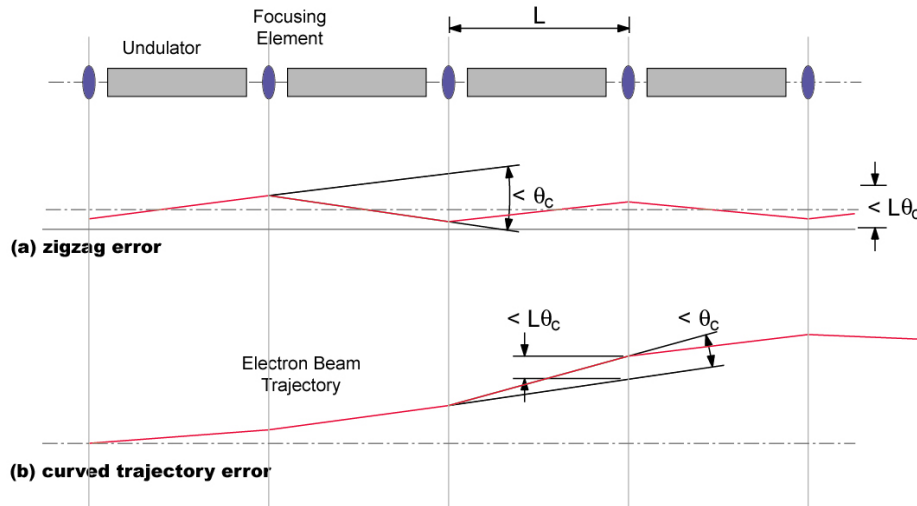


Fig. 1. Trajectory error model. (a) zigzag error, (b) curved trajectory error.

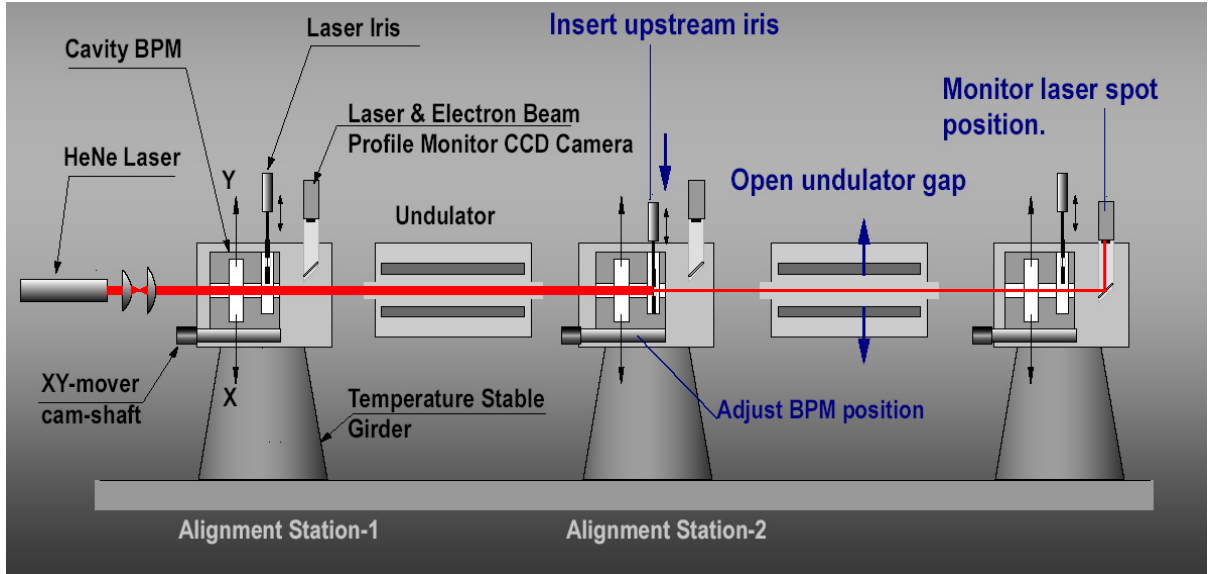


Fig. 2. Alignment stations in the undulator line are distributed in each 5 m separation. When we use HeNe laser alignment system, we open the undulator gap.

straight-line, but we need to keep the angle error smaller than θ_c .

Process of applying alignment procedure is equivalent to making a smooth trajectory by eliminating kick errors. We assume alignment error budget as Table-1. To achieve this tight accuracy, we are currently performing R&D on high accuracy BPM using cavity type detector and laser alignment system.

Table-1. Error budget on cavity-BPM alignment.

Error Source	Error Budget
Position error of alignment iris.	2 μm
BPM resolution	< 0.5 μm
Alignment iris to BPM electrical centre.	2 μm
Total	4 μm

ALIGNMENT TOOL

To achieve required alignment tolerance, we perform the following procedure (refer Fig.2).

- (1) Align BPM positions by using HeNe laser with 2 μm accuracy in a straight line.
- (2) Measure electron beam position using cavity type BPM, with resolution better than one micron meter at 0.1 nC or higher, and absolute accuracy better than 2 μm

referred to mechanical center, which is aligned by procedure (1).

- (3) Control beam trajectory by a corrector magnet on upstream focusing magnet.
- (4) Fine tuning: optical beam based alignment by monitoring radiation from undulator.

It will be probably necessary HeNe laser alignment procedure once per day, while electron beam position feedback will be always applied during beam run. The fine tuning (4) will be performed after procedure (3), and correction data will be used to refine the residual error in the alignment system.

LASER BEAM ALIGNMENT SYSTEM

HeNe Laser Beam Transport

For mechanical alignment of the cavity-BPM, we use laser beam alignment system. To avoid beam pointing instability due to the air turbulence, we need to transport the HeNe laser light in vacuum. If we prepare a separate vacuum pipe in parallel to the beam line, same as the SLAC two mile linac, we can stably transport a laser beam for fairly long distance, and we can align optical instruments, such as using a Fresnel lenses, in a straight line with fairly good accuracy, in a few tens-micron meter in transverse. However, a problem will arise when we

copy the mechanical position from the aligned Fresnel lens to a BPM center located in the electron beam line. Even if using invar material as mechanical structure to support the BPM and the Fresnel lens, small errors will build up at each mechanical contacts, and rotational error of the structure will also contribute, finally, cause a large error.

To solve this problem and achieve accuracy better than 4 micron-meter, we conclude the best solution is to introduce HeNe laser beam in the same line as electron beam, and directly align instrument at the same location, whose concept is illustrated in Fig. 2. The in-vacuum undulator is variable gap design, so that we can open the gap when we perform the laser beam alignment. With fully open the gap of 25 mm, we have enough room to transport the HeNe laser beam for a long distance.

Fig. 3 shows the envelop variation along beam propagation distance for various beam waist size, where we assume the laser beam has Gaussian profile. As well known, for a small beam waist, beam diverges quickly due to the diffraction effect. To transfer beam for a long distance, we need a large beam size. However, a small fraction of Gaussian beam tail will be lost due to the beam pipe aperture, and diffracted wave causes interference

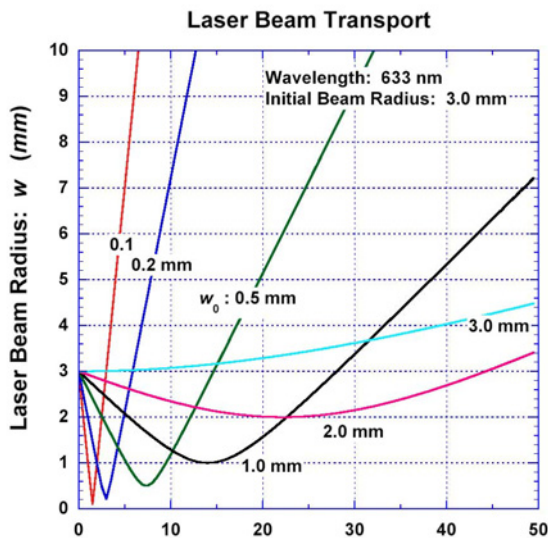


Fig. 3. Laser beam envelop variation along propagation assuming Gaussian beam.

fringe, resulting in generating alignment error. To avoid this effect, we have to choose laser beam size smaller.

To make beam power profile fitting to Gaussian function with better than $\pm 1\%$, the noise amplitude due to the diffraction effect has to be 0.5%, which corresponds to 2.5×10^{-5} . To keep the diffraction intensity less than 2.5×10^{-5} , we need to choose the beam size about five times smaller than the beam aperture. Since the minimum aperture is 20 mm at the cavity BPM, the laser beam size has to be smaller than 4 mm. From Fig. 3, we can transport 3 mm laser beam for 45 m long distance at waist size of 2 mm. This is shorter than 80 m long undulator line in XFEL project. Therefore we need to use chain of focusing lenses to transfer laser beam. As we discussed in the beginning of this chapter, aim of alignment process is to make smooth electron trajectory, therefore, if we stagger the chain lenses we may reduce alignment error.

Laser Alignment Tool

As shown in Fig. 2, the alignment stations are prepared at each drift-space between undulator segments, on which the cavity-BPM and focusing Q-magnet, and OTR profile monitor will be located. Retractable round iris will be mounted in the same block of the cavity-BPM. The transverse position of the cavity-BPM can be adjusted by remote control mover (see later sections for details). In order to minimize position drift due to ambient temperature change, the support stand is made by a special low-thermal expansion material (cordierite ceramic).

When we perform alignment of cavity-BPM, we open the undulator gap to provide enough aperture for the laser beam pass. Inserting alignment iris and monitoring its image on CCD camera at downstream, we can find mean center of the iris at upstream. Adjust the iris position together with the cavity-BPM position, and bring the iris image to the reference position on the CCD sensor. Repeat the same process on the series of alignment stations.

Airy Disk Image of Alignment Iris

To find a straight line of a laser beam, traditionally the Fresnel lens was frequently used, since the image position is insensitive to tilt angle error and easy to make a large lens. In the present case, the required longitudinal distance of one alignment span is not so long, it is basically two times of the undulator magnet as seen in Fig. 2, that is, about 10 m. In practice, to make efficient the system, and using a minimum number of CCD, we perform alignment for 20 m long section with one CCD.

When a laser beam is incident on a circular aperture of radius a , it generates diffraction image on a screen at downstream. When Fresnel number is much smaller 1, the circular aperture creates Airy disk, whose intensity is given by [2]

$$I(y) = \left[\frac{J_1(\alpha y)}{\alpha y} \right]^2, \quad (2)$$

$$\alpha y = \frac{2\pi a}{\lambda} \cdot \frac{y}{L}$$

Fig. 4 shows example Airy disk image. Using intensity data from a CCD camera, we calculate mean position by simply taking average as follows.

$$x_0 = \frac{\sum I_i x_i}{x_i}, y_0 = \frac{\sum I_i y_i}{y_i} \quad (3)$$

To make the smooth image, we need a small aperture, i.e., small Fresnel number (Fraunhofer

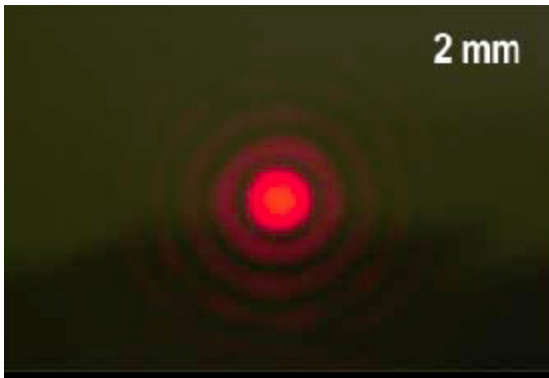


Fig. 4. Airy disk of 2 mm diameter aperture. HeNe laser image on CCD located 3 m downstream from a circular aperture of 2 mm diameter. Small aperture cleans up the error field of incoming laser beam. Fresnel number is 0.53.

diffraction limit),

$$F = \frac{a^2}{\lambda L} < 1 \quad (4)$$

The diameter (FWHM) of the first Airy disk can be derived from eq. (2) as follows.

$$D_A = \frac{\rho_{11}}{2\pi} \cdot \frac{\lambda L}{a} = \frac{\rho_{11}}{2\pi} \cdot \frac{a}{F} = \frac{\rho_{11}}{2\pi} \sqrt{\frac{\lambda L}{F}} \quad (5)$$

or, the distance which gives D_A is

$$L = \left(\frac{2\pi}{\rho_{11}} \right)^2 \cdot \frac{F D_A^2}{\lambda} = 2.7 \cdot \frac{F D_A^2}{\lambda} \quad (6)$$

where $\rho_{11} = 3.83$ is the first zero of Bessel function $J_1(x)$.

In order to avoid error field due to diffraction wave, the Airy disk diameter has to be much smaller than the beam pipe diameter (20 mm). We assume $D_A < 3$ mm, and use $F = 0.5$, which gives the minimum tail field. From eq. (6), we find $L < 19.1$ m, and from eq. (4), $a = 2.5$ mm, thus the iris diameter is 5 mm. In X-ray FEL, we prepare one CCD sensor for each four or five segments.

To fit well with a CCD sensor with industry standard, 1024 x 1024 pixels and 10 x 10 micron pixel size, we zoom down the beam size by a reducer lens in front of a CCD sensor. Be zooming factor of 1/2, the Airy disk diameter becomes 1.5 mm (FWHM). The number of pixels in this image

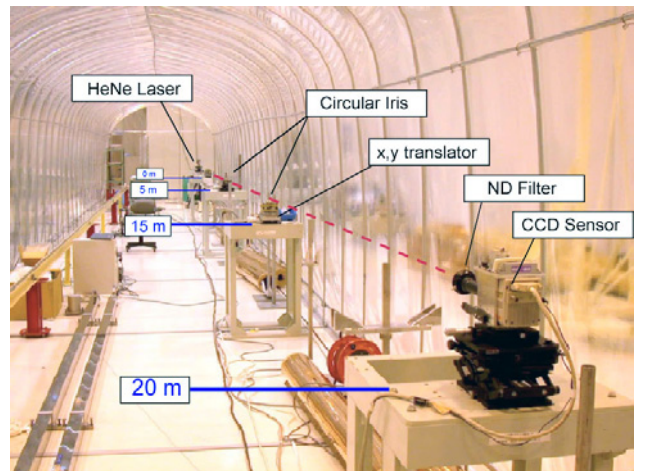


Fig. 5. Experimental setup of laser alignment. Circular irises are located at 5 m and 15 m downstream from the laser, and CCD sensor is at 20 m.

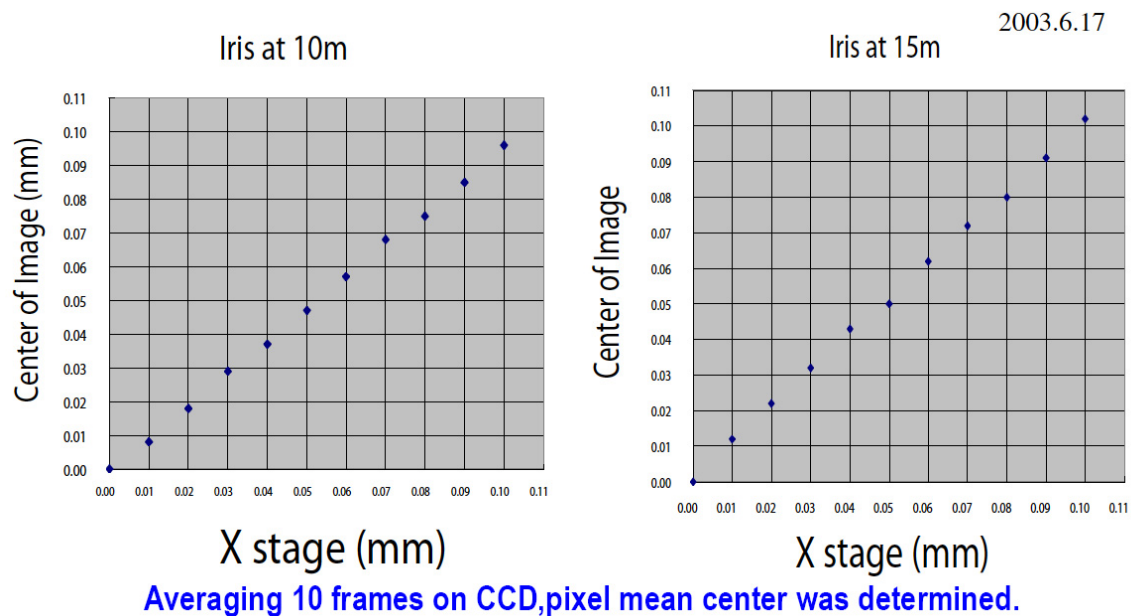


Fig. 6. Experimental test results on image response of iris movement. Each 10 μm step, ten frames of the CCD images were averaged and its mean center was determined.

is about $150 \times 150 = 22,500$ pixels. Using 10 bit digitiser (9 bit linear), and taking pixel average by eq. (3), we have very high resolution better than 20 nm (worst case).

Experimental Demonstration of Alignment

In order to demonstrate feasibility of the alignment using HeNe laser, we tested simple measurement. As shown Fig. 5, we made experimental setup in air with vinyl tunnel shield. We located a HeNe laser in one side, and measured laser spot from other side using CCD sensor, and put circular iris with 3 mm diameter. Distance from iris to CCD sensor is 10 m and 15 m. By moving iris position x- and y-direction, we measured movement of the mean center calculated by eq. (3). By eliminating air turbulence effect, we took multiple images for 10 times. To reduce noise, we cut low level noise at 5% intensity. Fig. 6 shows the result. We can clearly see 10 μm step movement, and points are fairly linear.

We conclude this method has special resolution better than a few μm and linear response in 100 μm range. Further R&D will be required on

- (1) Accuracy crosscheck. Comparing with other technique, such as, the laser

alignment tool using interferometer method. High precision water level will be also useful to check vertical alignment, and stretched wire for horizontal alignment.

- (2) Long term stability test, and repeatability test, specially the alignment iris setting repeatability.
- (3) Test vacuum chamber effect. Laser beam tail will be cut by limited aperture of beam pipe (20 mm), or reflected back, and create interference fringe on the beam core.

Those tests will be performed in the SCSS Test Accelerator.

Engineering Design of Alignment Circular Iris

Laser alignment system discussed above will provide position reference at the center of circular iris. One problem is how to copy the position reference to the center of the cavity-BPM. As discussed next section, cavity-BPM utilizes electromagnetic resonance in a pill-box cavity, and its electric field leaks into beam pipe for a certain distance. It exponentially decays as distance from the cavity center due to cut-off effect. To make 10^{-3}

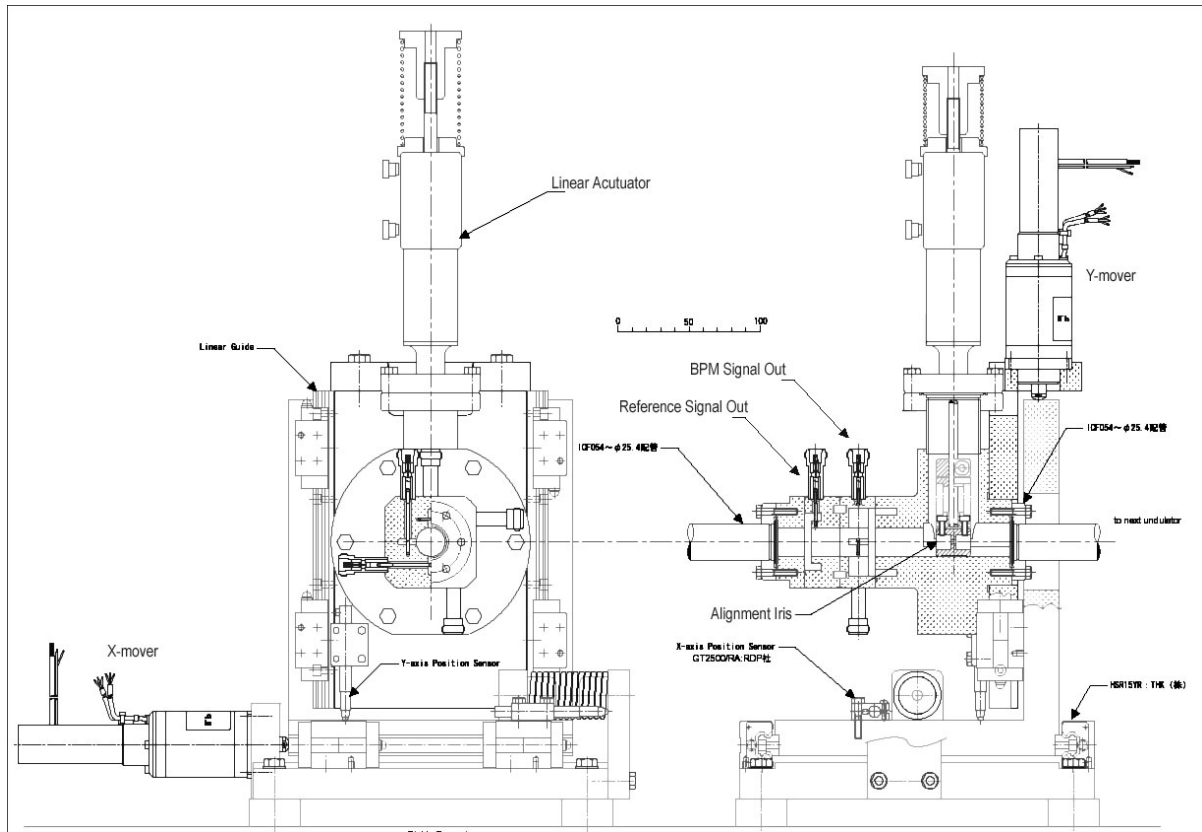


Fig. 7. The cavity-BPM assembly with laser-alignment iris.

amplitude, we need locate the iris 50 mm away from the cavity-BPM.

Figure 7 shows the alignment iris and cavity-BPM mounted on transverse mover. Cavity-BPM and alignment iris chamber are made in one block. Half cell of the cavity-BPM and the alignment block are fabricated from one piece of stainless rod on a turning lathe, thus they are aligned co-axis with accuracy better than a few micron-meter. Left-half cell of the cavity-BPM will be jointed by brazing technique. With careful geometry design of brazing boundary, we may keep alignment between two half cells within a few micron-meter. Modern machining center is capable of cutting 3D structure on the left half cell with accuracy better than a few micron-meters.

When the circular iris is inserted into the chamber, it mechanically contacts with inner surface of the beam pipe (20 mm), and pressed with air-pressure, and automatically aligned. A test will be required to verify repeatability of position setting.

If the cavity-BPM block axis is not well aligned with the beam line axis, it will introduce a position error between the iris center to the cavity-BPM center. To make this error less than $1 \mu\text{m}$, we need to place those instruments within $10 \mu\text{-radian}$ angle accuracy ($10 \mu\text{-radian}$ multiplying 100 mm spacing gives $1 \mu\text{m}$). We can align pitch by means of a water level. To align yaw, we can use the optical autocollimator, which typically can measure the angle in 0.01 second range, or, 50 n-radian. In

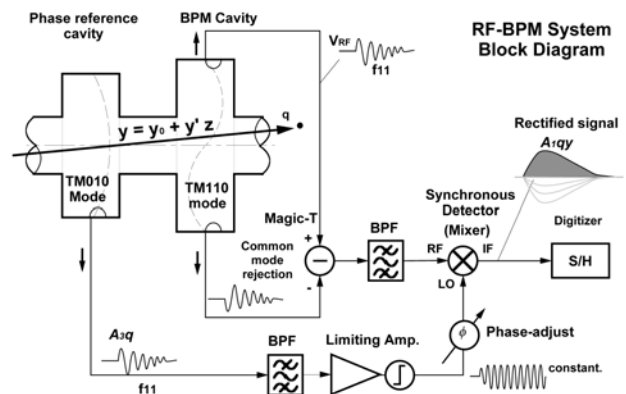


Fig. 8. Cavity type beam-position-monitor concept.

combination with 90-degree reflector (commercially available penta-prism has accuracy 0.8 seconds), we may look into a flat mirror placed on the side surface of the cavity block from a telescope located upstream about one meter offset horizontally, and align yaw within 1 second or 5 μ -rad.

CAVITY BPM

The highest position resolution and highest absolute position accuracy were achieved by the cavity-BPM type electron beam position monitor. The concept of this type of position monitor is schematically shown in Fig. 8. It uses TM110-mode, whose longitudinal electric field becomes zero at the cavity axis, and varies linearly with radial position r .

$$E_z = AJ_1(k_{11}r) \cdot \cos \phi \quad (7)$$

When the beam passes through the BPM cavity, it generates electro-magnetic field, which is sometimes called the wake field. The output voltage has the following components.

$$V_{RF} = A_1 q y + j A_2 q y' + j A_3 q + V_N \quad (8)$$

where,

$A_1 q y$ is the beam-position signal, which is the in-phase component of TM110 mode;

$j A_2 q y'$ the beam angle signal, which is 90 degree out-of-phase from the beam current;

$j A_3 q$ the common-mode leakage of TM010 mode through the band-pass filter; and

V_N the thermal noise in the detector circuit.

As seen in eq.(8), the beam slope and common-mode leakage signal has 90 degree offset from the beam position signal, which cause beam position error. In order to reject those unwanted signal, we use the synchronous detection circuit as shown in Fig. . The reference cavity operating at the same frequency, but TM010 common mode, is used to reject those error signal and detect the relative phase, from which, we may determine the position polarity using the synchronous detection circuit.

Position Resolution

The output signal into 50 Ω cable connected to the BPM cavity is derived using the equivalent circuit

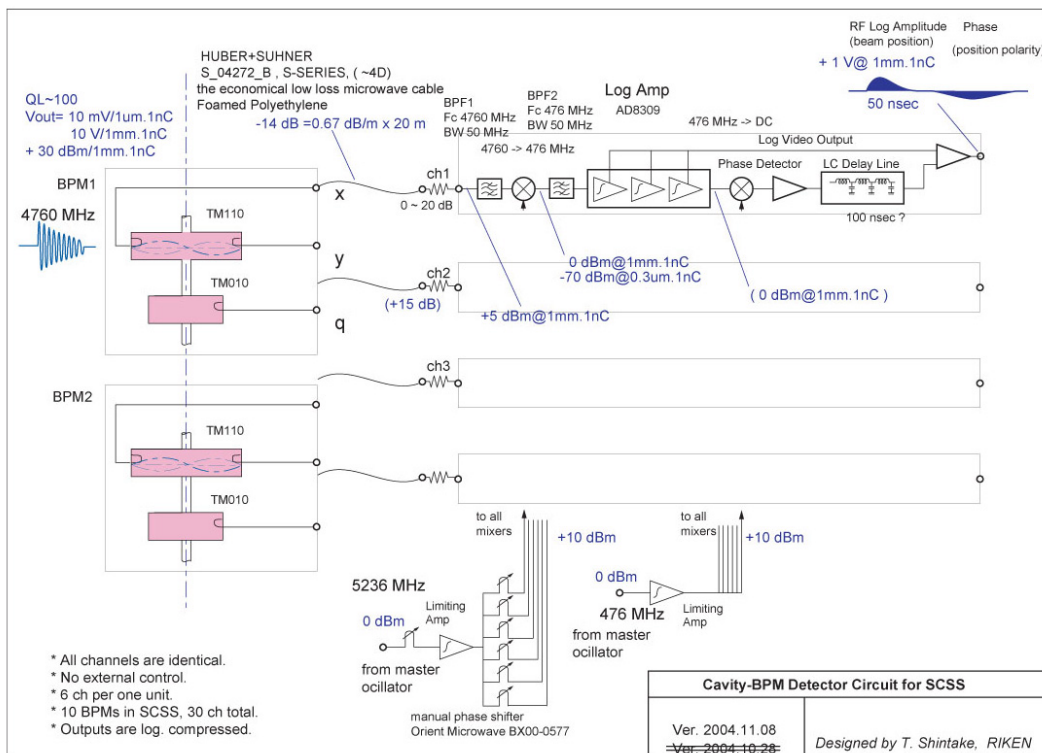


Fig. 9. Cavity-BPM detection circuit for XFEL.

model as follows.

$$\Delta V_{50} = \sqrt{\frac{Z_{50}}{(R/Q)_{11}^{cir} \cdot Q_e}} \cdot \Delta V_{11}(y) \cdot e^{-t/\tau} \cos(\omega t) \quad (9)$$

$$\begin{aligned} \Delta V_{11}(y) &= \frac{1}{C_{11} V_1} \cdot \int_{-\infty}^{+\infty} q \mathbf{E} \cdot \mathbf{v} dt \\ &= q \omega (R/Q)_{11}^{cir} \cdot \int_{-\infty}^{+\infty} E_z e^{jkz} dz / V_1 \\ &= q \omega (R/Q)_{11}^{cir} \cdot T(\theta_e) \cdot \frac{J_1(k_{11} y)}{J_{1,max}} \propto y \quad (10) \end{aligned}$$

Details of these equations are given in reference [3]. As seen these equations, near the beam axis, the output voltage is proportional to the beam charge and position displacement from the axis.

Different from the button type BPM electrode, the cavity type BPM has much larger beam-to-circuit coupling coefficient, this is due to fact that all of the wall current associated with beam interacts with cavity field. Therefore the intrinsic beam position resolution defined by the S/N ratio to the thermal noise in the detector circuit can be very high.

The equivalent thermal noise is given by

$$V_N = \sqrt{4kT\Delta B R N_F}, \quad (11)$$

where k is the Boltzman constant,

T the absolute temperature (K),

ΔB the bandwidth (Hz),

R the circuit resistance (Ω), and

N_F the noise figure of the head amplifier.

For 50 Ω impedance at room temperature, the noise level becomes

$$V_N = 1 \times \sqrt{N_F} \text{ (nV}/\sqrt{\text{Hz}}). \quad (12)$$

Using the cavity parameter listed in Table -2, the theoretical resolution for an ideal setup is 0.6 nm, assuming a noise figure of 3 dB in the head-amplifier. In a practical setup, by including the signal losses of rf-cables, magic-T, filter, attenuator, mixer and waveform shaping loss in filters, the total signal loss becomes -20 dB, thus the expected resolution becomes 6 nm.

In the course of R&D program for e+e- linear collider project, experimental test was performed in FFTB beam line at SLAC in 1998 [4]. Using three cavity-BPMs, reading beam position at the same

time and compare the position readout, the beam position resolution was determined as 25 nm. This is four times larger than the theoretically expected resolution, however, it is quite enough for practical application to the XFEL project, where the required resolution is 1 μ -meter level.

Position Accuracy

In principle, the cavity type beam position monitor has a highly accurate electrical center position to the mechanical center of the cylinder cavity. This is due to the TM110-mode has zero-field point at the cavity center, whose position is defined by average position of cylinder wall of the BPM cavity, which can be machined on a turning lathe, thus the

Table-2 Cavity-BPM Parameter

Single bunch charge: q	~ 1 nC
TM110 frequency: f_{11}	4760 MHz
Cavity radius : a	30.0 mm
Cavity length : l	5.0 mm
Beam hole diameter : D	20.0 mm
Effective cavity length : l_e	25 mm
Loaded Q factor : Q_e	130
Circuit shunt-impedance : $(R/Q)_{11}^{cir}$	22 Ω
Longitudinal impedance : $(R/Q)_{11}^l$ (numerical simulation by MAFIA)	410 $k\Omega/m^2$ (502 $k\Omega/m^2$)
Induced voltage in the cavity: V_{11}	120 $\mu\text{V/nC/nm}$
BPM signal output into 50 Ω : V_{50}	16 $\mu\text{V/nC/nm}$
Band-pass filter : ΔB	50 MHz
Thermal noise into 50 MHz : V_N	7 μV
Noise figure of detection circuit	3 dB
Signal loss in cable from BPM cavity to the detector circuit	-20 dB
Theoretical resolution : Δy	6 nm
Observed resolution at FFTB	25 nm

electrical center position is well agreed with the mechanical center, in practice, within a few μ -meter easily.

An important error source on electrical center location is signal mixing from the common-mode TM010, whose resonance frequency is lower than the BPM mode of TM110, which has 90 degree phase offset from the BPM signal as shown in the third term in eq. (8). In Fig. 8, the magic-T was prepared to reject the common mode signal. If the detection circuit is ideal, it does not cause position error. However, performance of the magic-T is not perfect, and the phase tuning of the synchronous detection circuit is not perfect, thus it cause certain amount of position error.

In order to eliminate this type of error, special geometry was designed as the BPM cavity, where the BPM signal is picked-up by means of antennas located inside the longitudinal slots, which separate the BPM signal from mixed rf-signals with the common mode in the cylindrical cavity.

Using a thin wire simulating a beam, the BPM response was measure with test rf-signal, and center position discrepancy was found 3 and 7 μ m for two BPM model cavities.

Detection Circuit

In XFEL, highest accuracy on beam trajectory control is required in the undulator line, where the maximum allowable error is five μ -meters for 1 A operation as discussed in the first section in this chapter.

In the machine operation, at the beginning, we transport beam through the undulator line with the undulator gap full open, and tune the corrector magnet to bring the beam to center position at each cavity BPMs. Realistic initial position error will be a few mm, and finally we have to adjust the beam within five μ -meters. Thus the detection circuit has to have 1000-times dynamic range during this process.

In order to compress the dynamic and reduce the required number of digit in ADC, we designed a detection circuit using the logarithmic rf amplifier as shown in Fig. 9. As shown in the sensitivity diagram of logarithmic response of Fig. 10, the detail position near the axis is magnified by the logarithmic circuit. Therefore we may precisely detect the beam position near the axis in one fixed rf-gain and ADC-range, where no gain adjustment is required from mm- to μ m-range. The rf logarithmic amplifier is designed to detect the rf-amplitude by the source current flows into the cascaded amplifiers, thus the phase has to be detected separately by the phase detector at the end of this cascade amplifier. A single chip logarithmic amplifier is commercially available in low cost, originally designed for telecommunication systems. Some of those products posses a very high performance, that is, the logarithmic function accurately extends up to 70 dB (1: 3000).

A SAW-filter was implemented to delay the rf signal at the end of logarithmic amplifier, and provides the phase information, which is detected by the same ADC with different timing. In this way, phase and amplitude is digitized in the same ADC.

We should not use the rf-acceleration frequency 5712 MHz as the BPM signal, because the dark-current emission from the high-gradient accelerator has the bunch train structure at rf-periods, and its frequency spectrum has a sharp peak peaks at 5712 MHz. We chose 4760 MHz as the BPM signal, which is the higher harmonic frequency of the sub-harmonic bunching frequency of 238 MHz in the electron injector. There are 5236 MHz rf-signal distributed in the accelerator, which is used as the local rf-signal to mixer in IQ-modulator and de-

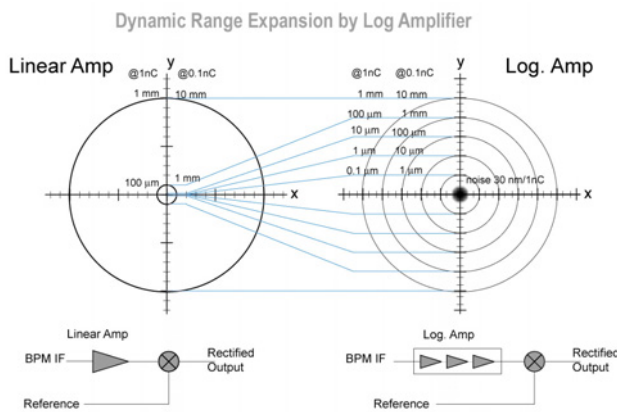


Fig. 10. Dynamic range extension by rf-logarithmic amplifier.



Fig. 11. Stable support stand for alignment station made by low-thermal-expansion ceramic.

modulator. Therefore, it is convenient to chose 4760 MHz as the BPM frequency, since the IF frequency 476 MHz is directly down-converted from 5712 MHz by mixing the distributed local frequency of 5236 MHz.

Ceramic Support Stand

We have to maintain cavity-BPM and focusing element stable in few μm range. We made the special design as follows.

- (1) Height of the beam-line from the floor as 800 mm, which is roughly half of traditional design. Lower beam-line height makes position movement and vibration smaller.
- (2) We made the support stands using a low thermal expansion material: cordierite ceramic, which has about ten times lower thermal expansion coefficient: $2 \times 10^{-6} / \text{deg-C}$. Thus, 1 deg change of 800 mm height becomes $1.6 \mu\text{m}$.

Figure 11 shows the support stand for the cavity BPM and focusing element, which is made by the cordierite ceramic. Interior cavity of the support stand is filled with sands to damp the vibration associated with the cooling water system, etc.

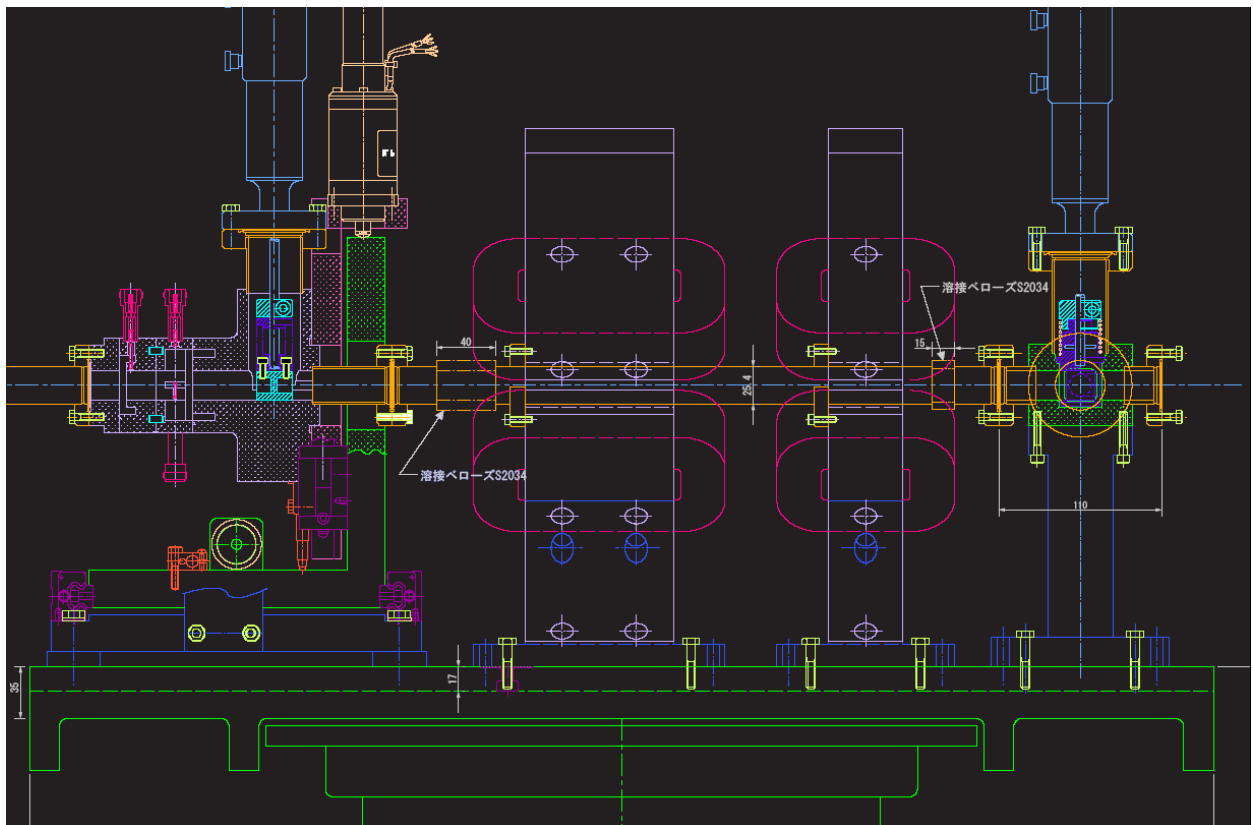


Fig. 12. Beam alignment station. (from left to right) Cavity-BPM, alignment iris, mover, Q-magnets, OTR profile monitor.

Fig. 12 shows the alignment station, where the cavity-BPM with the laser alignment iris on XY-mover, Q-focusing magnets, and the OTR profile monitor will be mounted on the ceramic support stand.

REFERENCES

- [1] T. Tanaka, H. Kitamura and T. Shintake, Nucl. Instrum. Meth. A528 (2004) 172.
- [2] elsewhere on textbooks for classical optics.
- [3] T. Shintake, "Development of Nanometer Resolution RF-BPMs", Proc. HEAC 1999,
- [4] T. Slaton and T. Shintake, "Development of Nanometer Resolution C-band Radio Frequency Beam Position Monitor in The Final Focus Test Beam", SLAC-PUB-7921, 1998.

FEL COMMISSIONING

Along with the undulator itself, a great many components must be installed throughout the 100 m of the undulator line, as a result there are many possible error sources acting to degrade the FEL gain. It is not easy, and may not even be possible, to reduce these errors to acceptable levels through an off-line alignment alone. It is therefore necessary to perform an on-beam fine tuning of components in the undulator line after installation and mechanical alignment, in order to reduce possible errors that will affect the FEL amplification process. Commissioning procedures using electron and photon beams will be described in the following sections which will enable us to adjust very finely the parameters of each component and reduce the residual errors to negligible levels.

INTRODUCTION

The FEL process actually takes place in the undulator line, but there are many key components composing the line: undulator, focusing magnets, and BPMs. Even if the performance of each component itself were to be perfect, there remain several error sources arising from their combined positioning and interaction which may greatly affect the FEL performance of the undulator line. Naturally some of these errors can be considerably reduced by employing the methods and procedures describe in previous chapters. Initial installation and setup procedures such as the undulator field corrections and BPM alignment technique using the optical laser can be done without an electron beam. It is important, however, to perform an on-beam commissioning to precisely check the performance of each component in the FEL driver and improve the overall performance as necessary. Let us call this live beam process the “FEL commissioning.”

ERROR SOURCES AND TOLERANCES

The principle error sources which may degrade the FEL gain of the undulator line are summarized in Table 1. Before describing the procedure for FEL commissioning that will reduce these errors, let us consider acceptable tolerances on each error source. It is difficult to derive an analytic expression for FEL gain which takes these errors into account. Therefore, we have performed simulations to investigate these effects numerically by using SIMPLEX, an FEL simulation code developed at

Spring-8 [1]. For a tolerance criterion, we rather arbitrarily look for an error level that would degrade the output power by half. Table 1 previews the tolerances that resulted from the simulations with the half power criterion.

Table 1. Error sources to be considered and acceptable tolerances for each.

Error Source	Tolerance
Field Discrepancy	$ \Delta K < 6 \times 10^{-4}$
Phase Mismatch	$ \Delta \phi < 40$ degree
Environmental Field	$ \mathbf{B}_g < 0.4$ Gauss
BPM Misalignment	$ \Delta x, y < 4 \mu\text{m}$

Field Discrepancy between Segments

The average magnetic field of each undulator segment is not exactly the same but deviates about a nominal value because of differences between segments in the average gap and/or in the operating temperature. This results in a difference in the average of the longitudinal electron velocity between segments and therefore causes gain degradation. In order to estimate the acceptable deviation (ΔK) from the nominal K value (=1.3), 500 sets of undulator line models were created with the K value of each segment being distributed from $K - \Delta K$ to $K + \Delta K$ randomly and uniformly, and FEL simulations were performed for each set. The results are shown in Fig. 1 as histograms of the output power for different values of ΔK . Note that the output radiation power is estimated at about 3 GW without any error sources. It is found from the

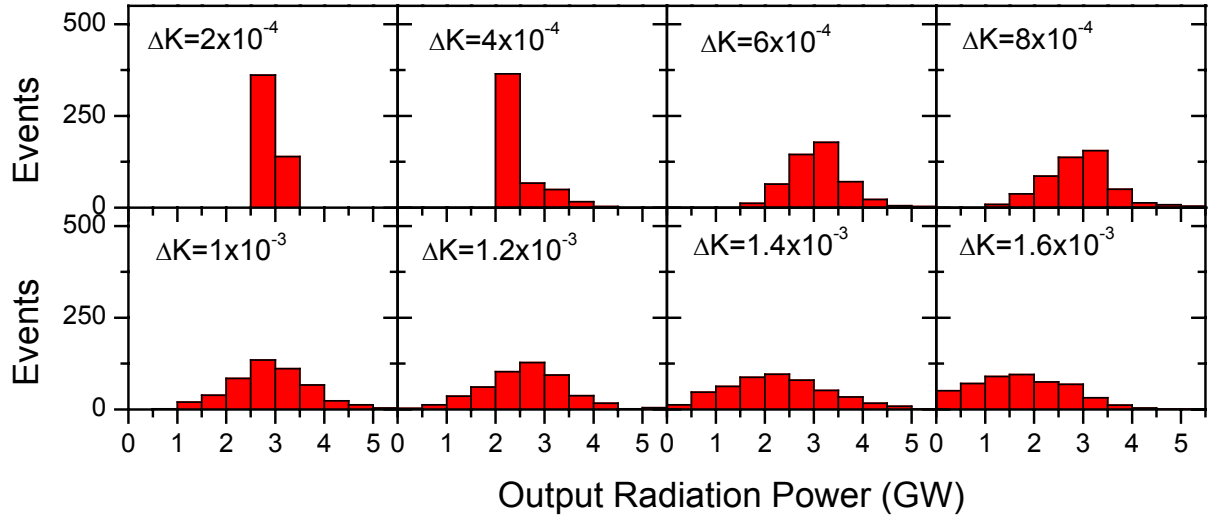


Figure 1: Histograms of the output power for different values of the K-value error ΔK .

figure that the histogram has a smaller mean and a larger variance for larger ΔK value. For example, the output power is found to be in the range from 2.5 GW to 3.5 GW when $\Delta K=2\times 10^{-4}$, while it extends from 0.5 GW to 4.5 GW for ΔK of 1.2×10^{-3} . This means that ΔK of 1.2×10^{-3} degrades the radiation power by 1/6 at worst. According to our tolerance criterion, we find the acceptable value of ΔK to be 6×10^{-4} .

Mismatched Phase in the Drift Section

The electron path length in the drift section between segments should satisfy the condition that the phase accumulated over the distance of the drift

section is an integer multiple of 2π . Achieving that insures good phase matching between the electrons and the radiation emitted in the each segment. It has been shown in [2] that this condition is not crucial to an FEL system that needs only a few segments for saturation, but this is not the case for SCSS. Thus, the phase slippage between segments should be adjusted to satisfy the phase-matching condition by some means: for example by inserting a magnet bump with an adjustable field. It should be noted, however, that the phase slippage cannot be adjusted perfectly to satisfy the phase matching condition, i.e., it will be some errors (mismatched phase).

In order to investigate the effects of the

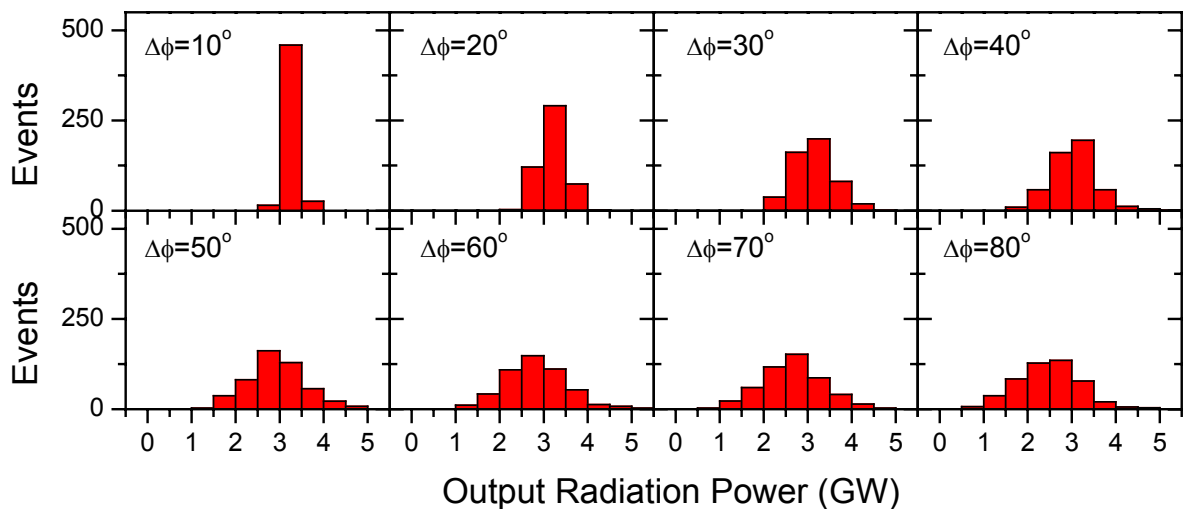


Figure 2: Histograms of the output power for different values of the mismatched phase $\Delta\phi$.

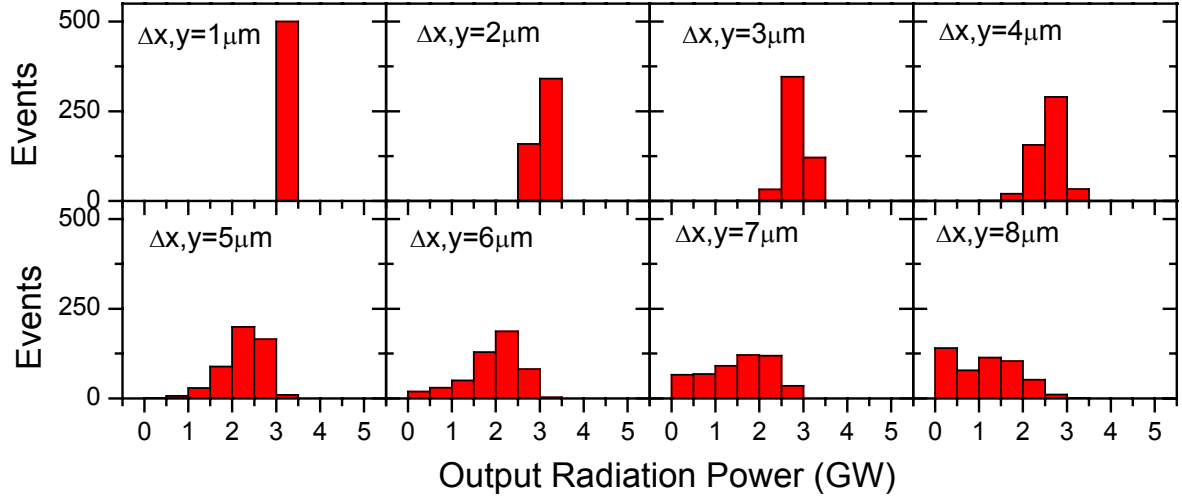


Figure 4: Histograms of the output power for different values of the BPM alignment accuracy $\Delta x, y$.

mismatched phase introduced in the drift sections, 500 sets of undulator line models were created with the mismatched in phase being distributed from $-\Delta\phi$ to $\Delta\phi$ randomly and uniformly and simulations were performed. The results are shown in Fig. 2 as histograms of the output power. The statistical trends are similar to those in Fig. 1. According to the criterion of tolerance, we find an acceptable value of $-\Delta\phi$ to be 40 degree.

Environmental Field

The geomagnetic field is very weak being at most 0.5 Gauss, however, it causes a parabolic electron

orbit that is not negligible in the FEL amplification process. For example, a uniform field of 0.5 Gauss over a length of 4.5 m results in a 50 μm displacement of a 6-GeV electron, which is larger than the electron beam size (1σ) of SCSS. This cannot be corrected for by the steering magnets installed between undulator segments. In addition, injection of an electron beam with a vertical position offset causes an error orbit similar to that induced by the geomagnetic field due to the natural focusing of the undulator magnetic field. Let us call these error fields the “environmental field.”

In order to estimate the effects of the environmental fields on the FEL amplification, we performed simulations to calculate the gain length (L_g) as a function of the environmental-field strength (B_g). The results are shown in Fig 3. The abscissa shows the strength of the environmental field, and the ordinate shows the gain length growth, $L_g(B_g)/L_g(0)-1$, in %. Assuming an exponential growth of the radiation power, we have an equation to determine the acceptable value of B_g according to our tolerance criterion as follows

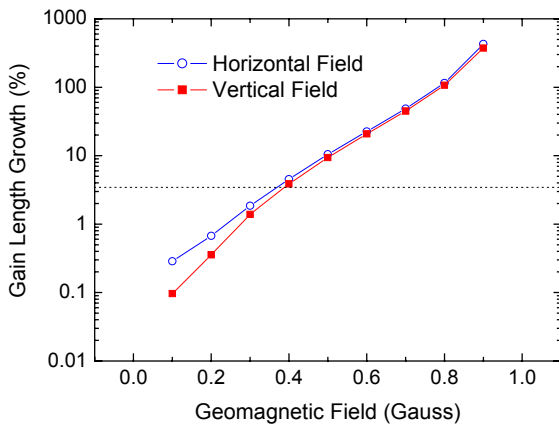


Figure 3: Growth of gain length due to residual uniform field.

$$\frac{L_g(B_g)}{L_g(0)} = 1 - \frac{L_g(0)}{L} \ln 2$$

where L is the total length of the undulator. Substituting $L_g(0) = 3.8$ m (estimated from the

simulation) and $L = 81$ m (4.5 m \times 18 segments), we have $L_g(B_g)/L_g(0) - 1 = 0.034$, which is indicated by the dotted line in Fig. 3. Thus, the acceptable value of B_g is found to be 0.4 Gauss, in both horizontal and vertical directions.

Trajectory Error

As shown in the ‘‘Undulator’’ section, the trajectory error within a single undulator segment can be significantly reduced by means of the field-correction technique described before. It should be noted, however, that this does not mean that trajectory straightness is ensured over the entire undulator line. In practice, the trajectory is monitored by the BPMs located between undulator segments and the electron beam is steered so that it goes through the origins of the BPMs. Thus, the accuracy of the BPM alignment is crucial to the trajectory straightness over the undulator line. In this case, dipole fields in the drift sections, or single kick errors (SKE) located between undulator segments, bring about a trajectory error. The gain degradation by SKE effects was analytically investigated in [3] and a critical angle θ_c , which gives the criterion for the SKE to be small, has been derived as follows

$$\theta_c = \sqrt{\frac{\lambda}{L_{g,3d}}}$$

With the SCSS parameters, θ_c is found to be 5.5 μ rad. The trajectory slope of the electron beam in the undulator segments should be smaller than this value. Thus, the accuracy of the BPM alignment should be better than several microns.

For quantitative estimation of an acceptable tolerance for the BPM alignment accuracy, FEL simulations were performed on 500 sets of

undulator line models with the BPM alignment errors ranging from $-\Delta x,y$ to $\Delta x,y$ randomly and uniformly. The results are shown in Fig. 4. The statistical trends are found to be similar to those in Figs. 1 and 2. According to the criterion of tolerance, we find the acceptable value of $\Delta x,y$ to be 4 μ m, being consistent with that obtained from the above analytical formula for the critical angle.

COMMISSIONING STRATEGY

Having obtained an acceptable tolerance for each error source, let us now describe the details of the FEL commissioning. A schematic illustration of the procedure for the FEL commissioning is shown in Fig 5. It is based on the effects of each error source on the optical properties of the spontaneous undulator radiation. Only one or two undulator segments are activated at a time, the resulting spontaneous undulator radiation is monitored at the photon diagnostics station located far from the undulator line. The station contains a spectrometer to measure the spectrum of undulator radiation and a slit assembly to extract the photon beam and measure the spatial profile of radiation. Because the electron beam emittance at 6 GeV (5.96×10^{-11} m.rad) is comparable to the optical natural emittance at 1 \AA ($\lambda/4\pi = 7.96 \times 10^{-12}$ m.rad), the coherent property of undulator radiation is less smeared than would be found in synchrotron radiation (SR) facilities. This enables a precision adjustment of the parameters to correct the error sources in the undulator line under consideration. It should be noted that the electron emittance can be reduced by inserting a collimator before the undulator line if the charge in the electron bunch is not of concern; which would makes the commissioning result more reliable.

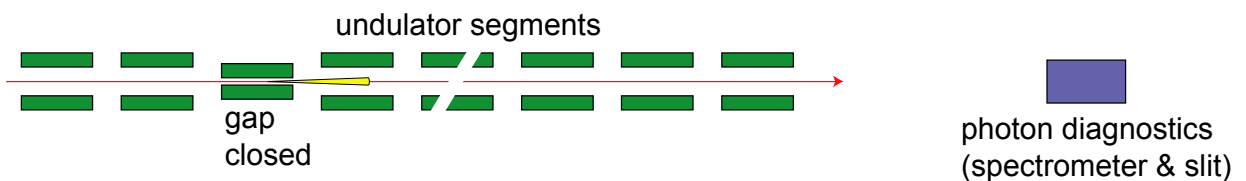


Figure 5: Schematic illustration for FEL commissioning. Only one or two undulator segments are activated to monitor the photon beam at the diagnostics station.

PROCEDURE AND ACCURACY

In the following, the procedures for correction of the error sources as listed in Table 1 will be discussed. The procedures are all based on the measurement of the optical properties of spontaneous undulator radiation from one or two segments. The electron beam parameters to be used are summarized in Table 2. The calculation of SR properties is performed using SPECTRA, a SR calculation code developed at Spring-8 [4].

Table 2. Electron beam parameters used in the calculation.

Emittance (x,y)	5.96×10^{-11} m.rad
Energy Spread	2.0×10^{-4}
Average betatron function	30 m

Field Discrepancy between Segments

The average field in the undulator determines the photon energy of the fundamental radiation. It is therefore possible to reduce the average field differences by comparing the peak energy of spontaneous radiation from a specific segment with that of a reference segment. In practice, it is more convenient to fix the photon energy for the flux density measurement of the spontaneous radiation, and then scan the gap of the undulator to change the K value while looking for the intensity peak.

Figure 6 shows the flux density as a function of

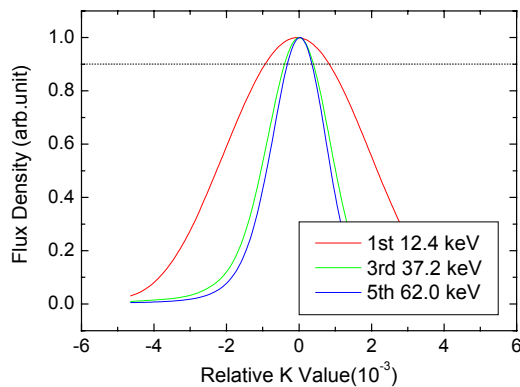


Figure 6: Flux densities at the peak energies of the 1st, 3rd and 5th harmonic as functions of the K value error with respect to the nominal value.

the K value for photon energies fixed at the peaks of the 1st, 3rd and 5th harmonics. The K value is indicated as a difference (ΔK) from the nominal value, 1.3. A FWHM value of 4.4×10^{-3} and 1.6×10^{-3} is obtained for the 1st and 3rd harmonics, respectively. It is intrinsic to undulator radiation that a narrower profile is obtained for the higher-harmonic radiation. This is, however, no longer valid for the 5th harmonic because the energy spread of the electron beam broadens the peak width.

It is easy to adjust the gap of each undulator segment so that all segments have the identical K values. However, the accuracy of adjustment is dependent on the S/N ratio of the measurement system. Let us assume that a 10% difference in intensity can be distinguished (10% criterion). Then the resolution is found to be 9×10^{-4} and 4×10^{-4} for the 1st and 3rd harmonics, respectively. In this way, we can reduce the error using the 3rd harmonic measurement to our acceptable level of 6×10^{-4} that has been previously determined.

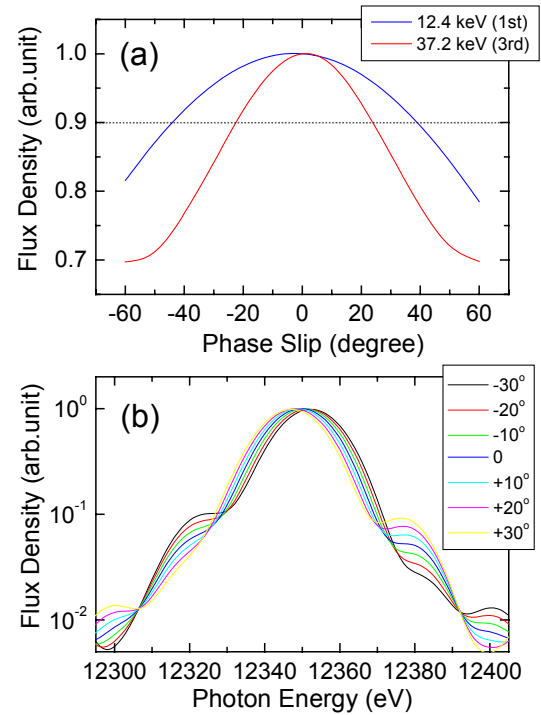


Figure 7: Effects of the phase slip in the drift section between segments: (a) flux densities as functions of the phase error at two energies of the 1st and 3rd harmonics and (b) variation of spectra around the 1st harmonic.

Mismatched Phase in Drift Section

The intensity of spontaneous radiation from two consecutive undulator segments is strongly dependent on the phase slippage between the two segments. Figure 7(a) shows the dependence of the flux densities on the phase slippage at the 1st and 3rd harmonics. Using the 10% criterion, the accuracy in specify the phase-matching condition is found to be 45 and 25 degree for the 1st and 3rd harmonics, respectively. These values can be improved by monitoring the variation of the spectrum as shown in Fig. 7(b), where growth of the sub-peak due to the mismatched phase is found. Thus it is possible

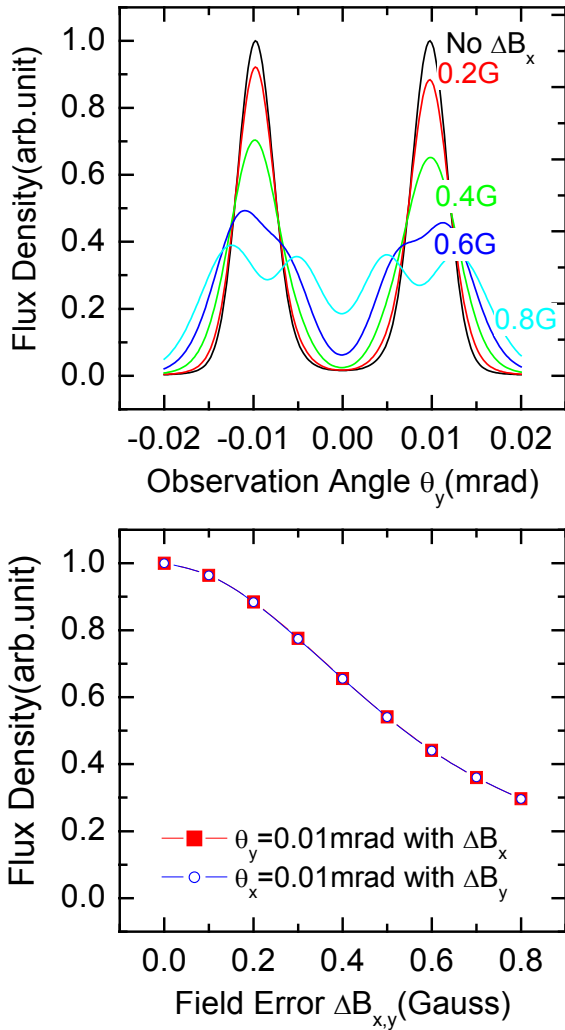


Figure 8: Effects due to the environmental field on the radiation intensity. (a) Angular profiles for different values of the environmental field. (b) Intensity variation as a function of the environmental field strength.

to adjust more accurately the electron path in the drift section to satisfy the phase-matching condition.

Environmental Field

The environmental field, being essentially uniform, can be corrected by long coils surrounding the undulator segment. There are several effects on the optical properties of undulator radiation caused by a uniform field, among which the off-axis peak in the angular profile is the most sensitive. Figures 8(a) and 8(b) show the effects due to the environmental field on the photon flux at 12.26 keV, slightly lower than the fundamental energy of undulator radiation, 12.4 keV. The flux is normalized by the peak values without the environmental field. As the strength of the environmental field increases, the off-axis peak is more broadened. Thus, the environmental field can be cancelled by adjusting the current of the long coil so that it maximize the flux at the off-axis peak. Using the 10% criterion (indicated by dotted lines in the figure), the residual uniform field can be

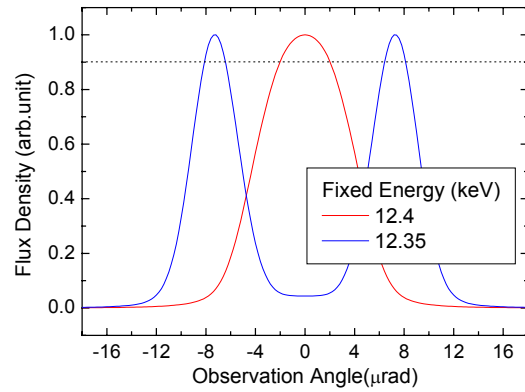


Figure 9: Angular profile for two difference photon energies around the 1st harmonic.

reduced to 0.15 Gauss or less in both directions.

Trajectory Error

The spontaneous undulator radiation has a good directivity if the undulator has a great number of periods; it is therefore possible to estimate the slope of the electron beam passing through a specific segment and correct it by monitoring the angular

profile of the spontaneous radiation from that segment. Figure 9 shows the angular profile from a single undulator segment at two different photon energies around the 1st harmonic. The peak has a narrower width at lower photon energy, which results in a more accurate adjustment of the trajectory slope in the undulator segment. Using the 10% criterion, the slope error can be reduced to 0.8 μ rad using 12.35keV radiation. This corresponds to the BPM alignment error of 2 mm.

REFERENCES

- [1] T. Tanaka, Proc. Int. Conf. FEL (FEL2004) to be published; see also <http://radiant.harima.riken.go.jp/simplex/>
- [2] T. Tanaka, H. Kitamura and T. Shintake, Phys. Rev. ST. AB 5, 040701 (2002)
- [3] T. Tanaka, H. Kitamura and T. Shintake, Nucl. Instrum. Meth. A528 (2004) 172
- [4] T. Tanaka and H. Kitamura, J. Synchrotron Rad., 8, 1221 (2001); see also <http://radiant.harima.riken.go.jp/spectra/index.html>

SCSS CONTROL SYSTEM CONCEPTUAL DESIGN

1. Overall Design

(1) Control Organization

The SCSS control system will use the MADOCA (Message And Database Oriented Control Architecture) operating system which has a proven record at SPring-8. MADOCA operates the linac, booster synchrotron and 8GeV storage rings, and beam lines at SPring-8; and at two other mid-scale machines in Japan, the NewSUBARU and HiSOR; it is operating reliably and has shown itself to a proven control system fully capable of supporting operations for all these accelerators.

Because it has all the flexibility and power needed to fill the needs of running all of the various operational modes at an accelerator facility, MADOCA can certainly control the combined operations of the SCSS accelerator and its insertion device light sources. Also, it could operate SCSS either from the SPring-8 central control room or from another control room located closer to the SCSS site. Turning to the beam line, where there are many users and a changing and unpredictable usage environment, with MADOCA it is possible to implement a flexible operating control system yet with the appropriate access limitations and security checks. The SCSS controls architecture will be based on the standard model for accelerator control systems, conceptually divided into 3 layers: man-machine upper level, device control layer, and low level device interfaces. The control devices will be interconnected by a high speed wide area network. This is the same control architecture employed at SPring-8 and as implemented in MADOCA.

The entire SCSS accelerator will be assigned a single device group name, with device subgroups identified under it appropriately for operational and maintenance purposes. Depending on the level of the device and the device unit under control, control message groups can be defined and registered with

MADOCA. In the development process, the SPring-8 Message Guide Lines – as separately documented and as implemented in include header files which define the C language prototype declarations both in format and grammar should be referenced. From the beginning, strict adherence to these standards in matters of group names, error codes and the like will make possible to produce an integrated control system with is both efficient, error free and safe.

(2) Man-Machine Computer System

For the man-machine interface layer, computers running the UNIX OS are unsurpassed in terms of stability. Tools, Builder Wizards and Application software packages have all achieved satisfactory levels, both in quality and cost. From the viewpoint of hardware reliability and OS support, a control system composed of workstations running a commercial UNIX version such as HP-UX would be desirable, but it could also be implemented in PCs running Linux. Software development for this project will primarily be done in C. There is no particular reason why C++ has to be used; depending on the purpose, it as well as other languages such as Python, FORTRAN or Java would not be precluded. Microsoft WINDOWS OS is probably not suited for application to mainstream accelerator controls because of its questionable stability, and proclivity to virus infections and other malware attacks. However, there is a sole exception in the case of commercial subsystems for measurement or device control that are available only for the Windows OS. The machine operation control panels will be made with the same GUI builder used in standard MADOCA practice.

(3) Server Computers

Dedicated machines will be provided for the obvious system servers: database, file, and web

servers. In particular, the device database server is absolutely indispensable for normal accelerator operation. Further, beam diagnosis, failure analysis and repair strategy planning are all greatly assisted by an excellent database server. The database server will be able to support machine operation because it will store and have access to many tables containing parameters and device organization and interconnection map data, setpoints and current readout values, alarm records and so forth. In order to make the data in the database easily accessible, a web-server will be set up so that device status can be inspected, and data log analysis can be done from anywhere on site. The executable programs for accelerator operation will be created within the same common development environment already used at SPring-8. Programs, setpoint data etc. will be stored and maintained at a central location on a file server, from which they can be exported as NFS files for remote access.

(4) Device Controllers

Besides remote control operation from the central control room, the device control system is required to support local control in order to facilitate bringing up the equipment, maintenance and failure analysis. Anything which can be done with local controls should also be able to be done remotely from the central control system. Depending on the control characteristics of the individual device, either a PLC or VMEbus based system can be used. When hardware reliability is considered to be most important, PLC solutions are appropriate. Where there is a coherent grouping of function, such as for the C-Band klystron modulators, or vacuum systems, there is merit in having each subgroup having its own PLC or VMEbus subsystem for unified control. Doing this also has the advantage that independent operation or tuning etc. of entire groups can more easily be done. PLCs besides executing the specific device control fixed sequential ladder program, will also communicate with the upper layers of the control system via a VMEbus interface. High speed controls, and

overall control will use VMEbus systems, thus making advanced functionality available for operations. When using PLCs, all of the control applications logic should be implemented in Ladder Logic; it would be most desirable if each device developer or responsible person was able himself to maintain and extend the code functionality as needed. For any PLC to be considered for adoption, conformance to open communications standards is necessary, while inter-operability with other network and system components is a sine qua non for selection.

As a general rule, GPIB will not be used for device control. When a VMEbus crate is operated with a GPIB interface board inserted, not infrequently reliability problems arise. If there happens to be measurement instrument which only has a GPIB interface, it should be used over the network through a GPIB-Ethernet converter.

(4-1) VMEbus System

In terms of system composition and control software creation, the VMEbus system can provide a great deal of flexibility. System development becomes easy since a great variety of resources such as CPU boards, I/O boards, device drivers are already available and in use at SPring-8. CPU boards should use an Intel CPU, and not require a forced air cooling fan. Low power CPU versions are better in helping to control heat dissipation. The OS should be either Solaris8 or Solaris9, with capability of booting from a Compact Flash card. In the cases where high speed analog processing is required, such as for waveform analysis, it should not be done by dedicated front-end electronics circuitry, but rather a board should be developed which can be read out by a back-end VME system. When high speed feedback, real-time response (particularly for synchronized operation) is required, VME based shared memory should be used. For places where the noise environment is very severe, an optical fiber based high speed remote I/O VME system could be used as a field bus.

(4-2) PLC, Fieldbus, etc.

PLCs are programmable control devices with reliability comparable to hardware logic. PLCs execute a fixed control sequence; usually a local control capability is also implemented to support maintenance and monitoring of the controlled device. A display panel is provided for local control for this reason. Because a PLC is provided for each set of subsystem devices, the amount of signal cable wiring is reduced. Depending on the situation, if DeviceNet or other fieldbus is used for interconnection, the cabling does not need to depend on the where the controlled device is physically located and there is much more flexibility in the way wiring can be done. Because it is desirable to use an open standards based communications protocol between PLCs, the FL-net as proposed by the Japan Electrical Manufacturers Association will be used. FL-net is based on Ethernet, using token-passing, time-division multiplexed rotating slots, or messaging between addressed stations. VME boards have been developed with FL-net interfaces so as to facilitate using VME as a gateway between the fieldbus and the upper level Ethernet system. Using this option for PLC-VME interconnection, PLCs can continue to execute their control sequences without interference, yet data is available over FL-net to be collected and processed at high speed by the VME processor. In general PLC programs will be implemented in “ladder logic”, but the option exists to create applications with C or other higher level languages, and execute them in the PLC network computer.

2. Individual Components

(1) Network

Figure 1 shows the overall SCSS control system network. A fully redundant dual star topology set of optical fibers connects the network nodes inside

the control room to wherever the individual controlled devices are located. The network main trunk line is also a redundant pair of Giga-bit Ethernet cables. As a general rule, branch line twisted pair cable will be run from the position of each controlled device node back to its controlling VME crate. But, in places where the noise environment might be thought to be particularly bad, optical fiber can be used.

Separately from the above control network, a maintenance network will also be laid out to the accelerator building. Using this network, it will be possible to do maintenance while reviewing stored log file data, or to automate some of the maintenance procedures by going through the control system.

The program software development servers will be placed in the DMZ with a firewall interposed between them and the control and the office networks. Doing this, software development can be carried out from the office network, yet control network can be effectively cut off from the outside world. This architecture provides security and helps prevent the spread of computer viruses into the control network.

Since network technology is advancing rapidly it may be possible to later provide a wide area network even faster than Giga-bit Ethernet, and as accelerator operations also become more sophisticated and demanding, such an increase in network capabilities may be required. Therefore the fiber installation and device selection will be done now with this eventuality in mind.

(2) Operator's Console

HP-UX and Linux are supported for the operator's console OS. Specifically, HP workstations running HP-UX 11.0 and PC's running Red Hat Linux (RHL) have both been used, and performed reliably. For SCSS, 10 or so HP workstations running HP-UX 11.0 on the 64 bit PA-RISC will be provided. Operating programs will be developed using X-Mate, a GUI creation tool. All programs will be written in the C language, will be

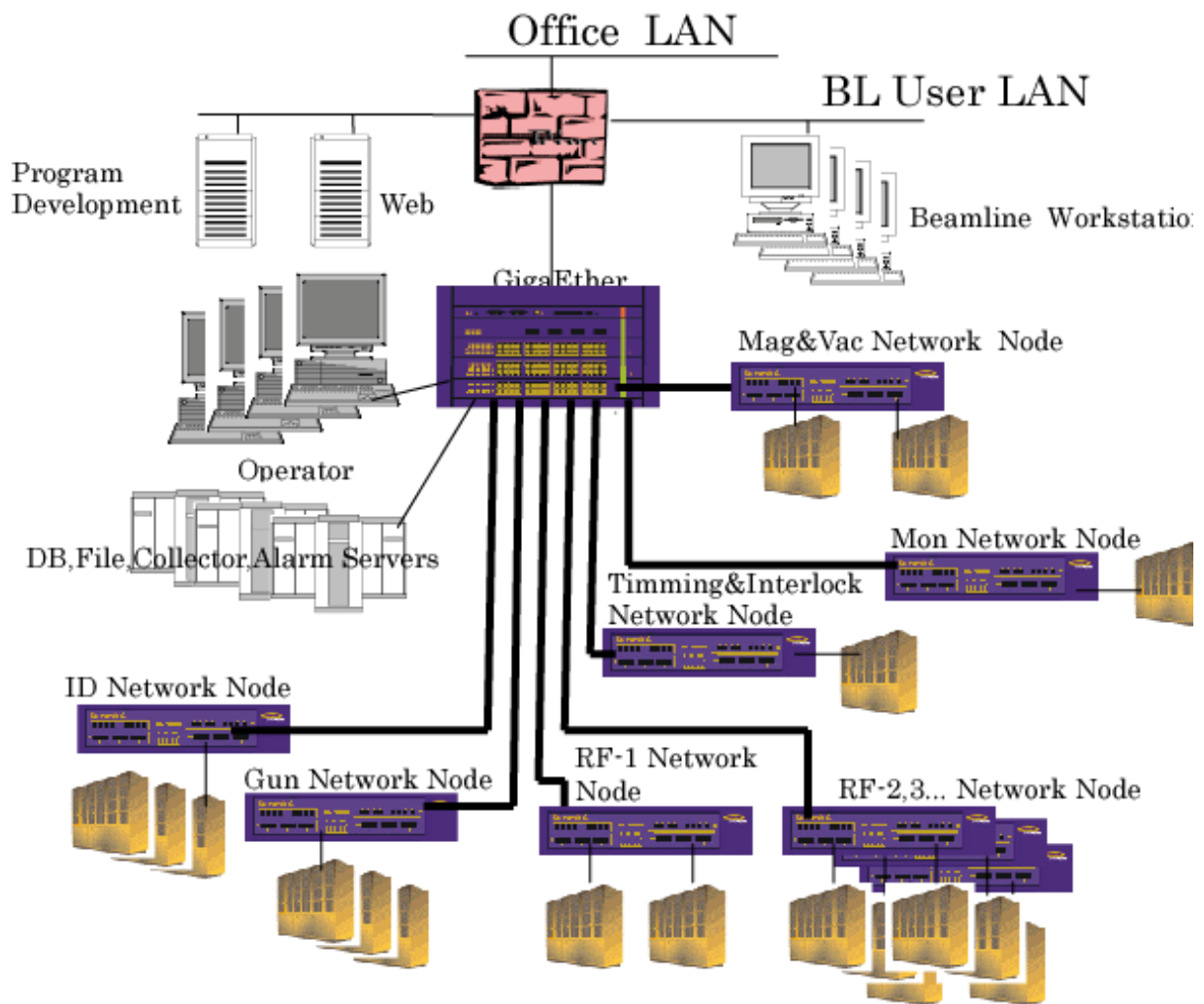


Figure1. Overall Network Diagram

compiled with the standard make command on the program development HP-UX 11.0 servers, and actually run on the operator's console machines.

(3) Server Computers

Sybase-ASE will be used for the system relational database (RDBMS). Sybase is currently in use by SPring-8 and there are versions for both HP-UX and Linux. Because the Linux version of Sybase is inexpensive, an enterprise class RDBMS can be inexpensively set up. It would even be possible to run it on a multi-CPU PC with sufficient memory running RHL. Nevertheless, judging from our previous operational experience, since the overall reliability of the system depends so critically on this server and we know that the 64 bit enterprise server computers from HP have provided superior performance; HP products will be used for

SCSS. If there are signs that the database processing is not fast enough, the situation can be dealt with by increasing the numbers of CPUs. Dual power supplies and network hardware will be provided for redundancy, and data will be backed up to mirrored RAID disk storage system. Since high availability is required, there will be 2 database servers combined to provide a high availability cluster.

The file server will use NFS to export the executable operations programs, parameters and data files. Because accelerator operations would be impeded by any failure of the file server, just as in the database server case, it will have redundant power supplies etc. The actual files and data to be served will be kept on mirrored RAID disk. A rather small scale HP server computer will be used.

The usefulness of Web technology is well recognized not only because data access via a browser allows monitoring device data, but all

forms of information become available for viewing from any place. So the web server will be built on a multi-CPU server PC running RHL to make possible display of device data during operations, device data log files and alarm files etc.

(4) Device Control Subsystems

The control of the linac, including all device interlocks, will be done almost entirely with PLCs. The interconnection of the PLCs and the rest of the control system will be done through FL-net. Controllers for the klystron modulators and so forth will be designed so that they can be switched between local and remote control; and the same functionality should be available both to remote control and the local control panel. As previously mentioned, a FL-net interface board for VME will be developed so that VME can be used as the gateway between the PLCs and the rest of the control system.

a) Vacuum System Controls

Almost everything including machine protection interlocks can be done with PLCs. A single VME station will use FL-net to communicate with the vacuum system control PLCs under it.

b) Magnet Power Supply Controls

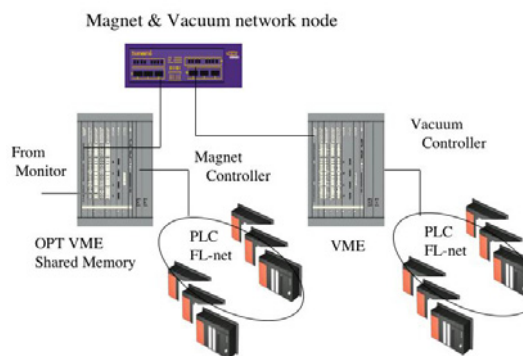


Figure 2. Magnet & Vacuum Network Node

Almost everything including machine protection interlocks can be done with PLCs. A single VME station will be used to control the beam transport line magnets; it will have an FL-net interface to communicate with its PLCs. The transport magnet control will use optical fiber, and so that pulse noise will not cause interference on signal lines, the VME crate will have an optical transceiver board.

c) RF Controls

A VME board will be designed with high speed AD / DA and FPGAs to provide the voltage and phase control waveforms for the acceleration cavities. Optical fiber will be used for the VME system data input. Other low level control, such as for power supply control and device protection interlocks will be done with PLCs. Intercommunications between the rest of the control system and PLCs will be over FL-net. Each klystron drives 4 accelerator structures forming a single unit. There will be a VME crate for each unit, and all of the low level logic, power supply control etc. for the unit will be done on a stand-alone basis by that VME system.

d) Beam Monitor System Control

The same VME waveform control board designed for the RF system will be used here too, with input data coming into the VME crate over optical fiber. Using the locally acquired signals, and a networked shared memory board, the VME

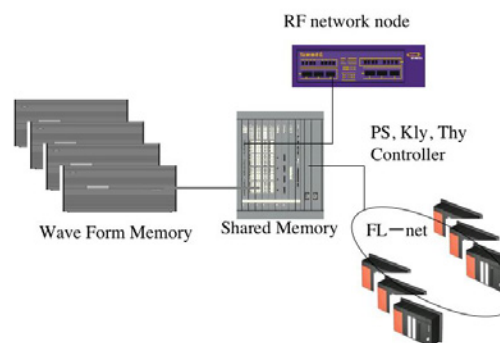


Figure 3. RF Network Node

controller will be able to provide high speed feedback to the transport line magnets. An optical transceiver board will be used for the beam current monitors, etc. again using optical fiber to isolate the analog system from the VME.

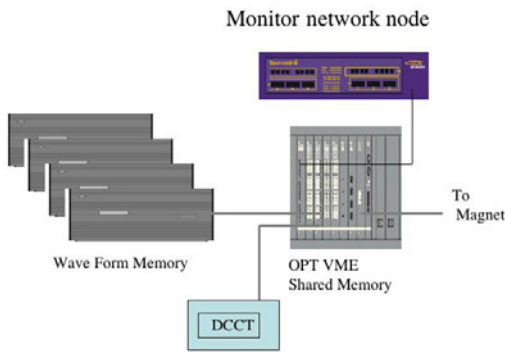


Figure 4. Beam Monitor Network Node.

e) Insertion Device Control

Figure 5 shows main features of the insertion device control system. Device interlock PLC data will be collected over FL-net. Everything else, pulse motor controllers and encoders, ADC/DAC signals etc. will all be taken care of with the VME system.

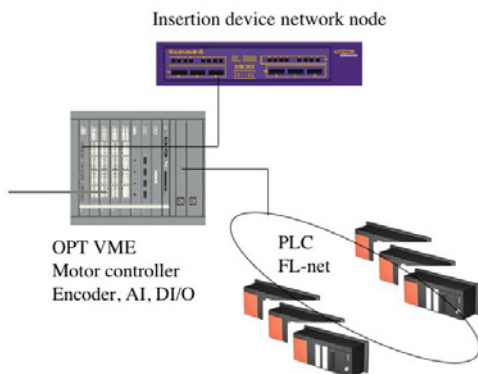


Figure 5. Insertion Device Network Node.

(5) Control Room

SCSS can be operated from the SPring-8 central control room, or a control room could be located in the SCSS facility from which operation would equally be possible. But before going into production operation, it is expected that the closer control room will be used for bringing up the individual components and the original SCSS commissioning. After operation from the central SPring-8 control room starts, the local control room could be used for maintenance purposes, etc.

3. Development Process and Methods

(1) Overall Philosophy

The process of developing the SCSS control system from initial startup until production operation is achieved can be specified. A list of all of the control points for the devices that make up the accelerator is to be made, along with a list of corresponding control commands. The MADOCA upper level software works with abstract devices, so that it does not have to be aware of hardware details such as channels or slots or the like. At the stage when the message lists are completed, we finally have an overall grasp of the accelerator operation. From here, spiral development of the software can begin keeping in step with the progress in development of the various component devices.

First working bottom up, application software for the lower level controls should be finished before higher levels are started. This means beginning with component device control software running on the PLCs and VME computers. Local control sequencing and diagnostic logic should also be prepared at this time, along with the control software for each equipment device component.

As the lower level control software is completed, operational testing of the controlled device can begin. This test operation would be in the local control mode, not remote control. Even when software is still incomplete, rapid prototyping techniques can be used to initiate testing. It is very important at this stage that point by point the

hardware and software controlling each operation be tested and proper operation confirmed, focusing on the new as yet untested portions as step by step development proceeds. From about the midpoint in software development, writing the operational GUI software for the operator's console can begin, and the correct operation of the GUI logic in a standalone mode with dummy returns from the operating system and hardware can be confirmed. Next, the MADOCA middleware can be linked in to complete the connection to the lower level control system and for the first time the overall testing can begin.

(2) Development Task Assignment

In developing the SCSS control software, assistance will be requested from the SPring-8 control group that originally developed MADOCA. The division of labor and responsibility between the SCSS device control designer and the appropriate SPring-8 control group specialist will be as follows. The device designer will also design the operational GUI program for that device. Since the GUI program captures essence of the device operation and collects into itself the relevant knowledgebase about the device, it should naturally be created by

person responsible for the device, who knows it best of all. The responsibility of the control group is to provide and support the MADOCA framework; and the control group point person is to assist in the integration of the device designer's application program into that overall framework.

It would be good if applications that run on the PLCs could be made by the person responsible for the device in question, but outsourcing such development would also be alright. But even if the fixed sequence coding and the device commissioning logic is outsourced, in cases where increased operational functionality might be needed at any time, or on an ongoing basis, then it is necessary that the PLC software development process, tools and technology be maintained by the in house staff. The control software that runs on the VME stations can be created by the SCSS staff as there are many example programs and experience to build on.

The control group will be depended upon to create the database administration tables, as well as the configuration tables with device parameters, alarm monitoring information etc. Because templates are already available, the web display system which is driven from the database will be easily made.

TIME BASE AND RF SIGNAL GENERATION, TRANSMISSION AND DISTRIBUTION SYSTEM

The 6 GeV electron linear accelerator (linac) for the SCSS soft X-ray free electron laser uses 5712 MHz pulsed rf to accelerate electrons [1]. High-power klystrons installed along the accelerator generate the pulsed rf signals. A system to distribute a reference rf signal to the klystrons is necessary. Furthermore, a timing pulse distribution system is needed for the klystron modulators to make the pulsed rf, and for monitor and instrumentation devices. The SCSS will generate soft X-rays with the extremely narrow ~ 0.5 ps pulse width 6 GeV electron beam in order to analyze the structure of proteins and their time resolved dynamic behavior. Depending on the experiment, in some cases, measurement precision with femto-second order timing jitter is required [2]. For this reason the systems which distribute the reference time standard rf signal and trigger pulse, and which thereby determine the time accuracy of the accelerator, should have the same femto-second order precision. This makes the low power rf system and the timing distribution systems of the linac very important. In the following paragraphs, we describe the systems for realizing the femto-second time accuracy, the causes of the timing errors in the systems such as noise, and finally the rationale for why the systems were chosen.

THE CAUSES OF ACCELERATOR ENERGY VARIATIONS

In an electron linear accelerator, the causes of variation in energy accelerating an electron riding at the crest of the rf pulse fed from a single klystron into an accelerator structure are defined as follows:[3]

1. The klystron output variation caused primarily by a changes in the high-voltage pulse.
2. The input frequency changes and temperature changes of the cooling water to the accelerator structures.
3. The effect of detuning of the rf pulse compression cavity such as a SLED. The detuning is may be caused by a temperature change of cooling water. This effect is also due to changes of the frequency of operation of the accelerator.
4. The effects due to thermal expansion of the rf cables, frequency instability of the master oscillator and phase variations of the klystron and rf solid state devices which are proportional to ambient temperature changes.
5. The effects of trigger timing pulse jitters and the rf phase jitters.

The low-power reference rf system and the timing pulse distribution system must be such that the 4 and 5 terms are reduced as much a possible. In previous accelerators, this effect has been suppressed by using a phase stabilized coaxial cable [4] having an electrical length stability of 2 ppm/ $^{\circ}$ K to transmit the timing and reference rf signals. This cable is very thick and heavy and not easy to work with, and large rf power is necessary for driving the cable for a long distance (e. g. it means large rf signal transmission loss and large power dissipation in the cable.) In the next system, we should also employ a light cable to be easy to work and to have small power dissipation. We must realize the stable low power rf and timing system for SCSS.

SCSS LOW POWER RF SYSTEM (REFERENCE RF SIGNAL TRANSMISSION)

Figure 1 shows the SCSS time base distribution and low-power rf reference system, designed to reduce as much as possible jitter and disturbance causing factors. The low-level rf system for driving the high power C-band klystrons which are the

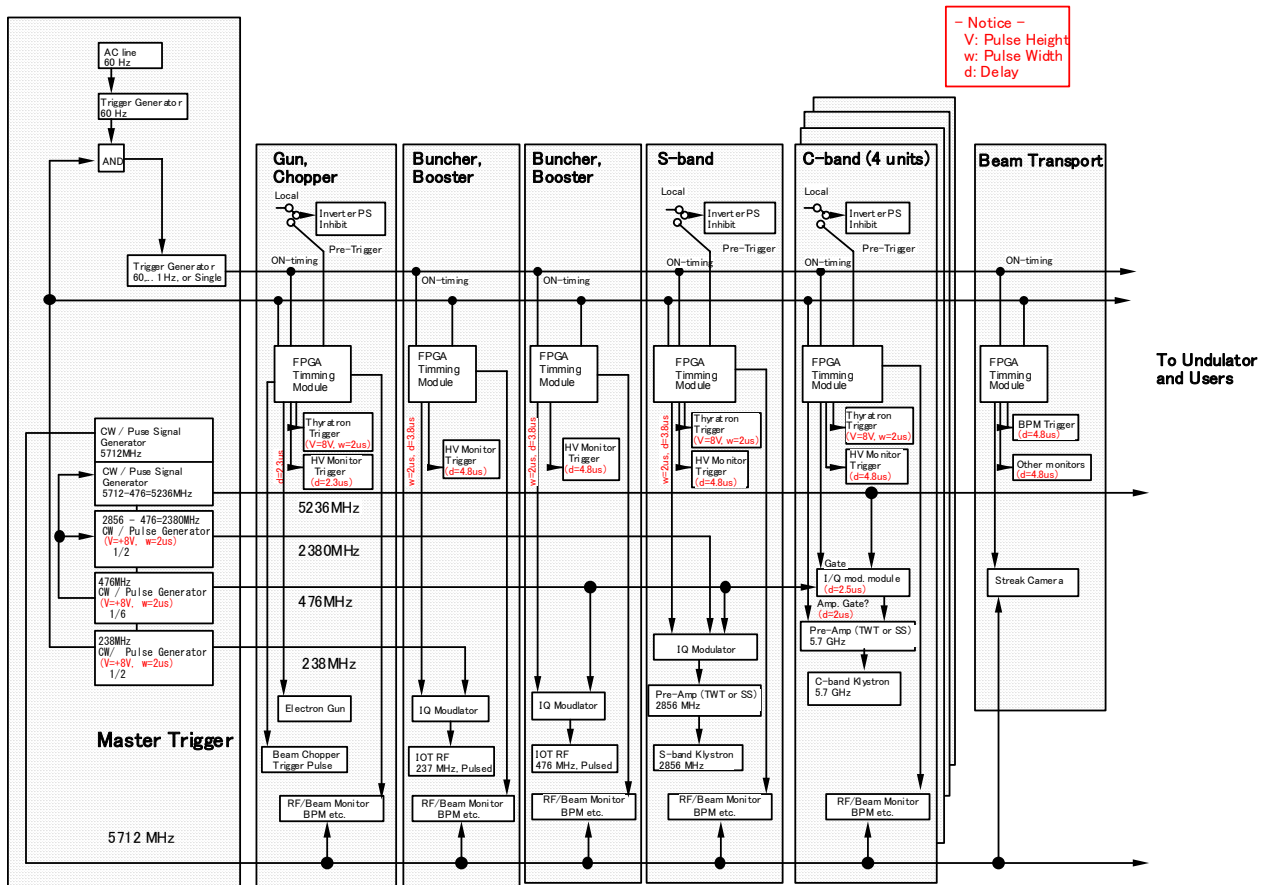


Fig. 1: Fig. 1. The low power rf and timing distribution system for SCSS. The output of the Master Trigger drives 3 logical groups of components: the Injector (Gun, Beam Chopper, Sub-Harmonic Buncher (238 MHz and 476 MHz), Buncher, and Booster accelerator 2856 MHz), the Main Accelerator complex, and the beam transport system to the undulators. The rf signals at 5712 MHz, 2856 MHz, 476 MHz, and 238 MHz are made by frequency division and a time reference is also created by the master oscillator. Optical fiber cables are used for transmitting the signals.

main rf sources for the SCSS is shown in Fig. 2. The system is comprised of I. a master oscillator system, II. a signal transmission/distribution system, and III. a drive system delivering the signals to the klystrons etc.

I. Master Oscillator system

The master oscillator system as shown in Fig. 3 makes rf signals with frequencies of 238 MHz 476 MHz, 2380 MHz, 5326MHz and 5712 MHz. The 238 and 476 MHz signals are for the sub-harmonic buncher and the booster acclerator. The signals of 2380MHz and 5329MHz are necessary for the IQ modulations at the klystron inputs. 476 MHz from the IQ modulator has added to it either 2380MHz

or 5326 MHz to produce the final signals at 2856 MHz and 5712 MHz which drive the klystrons. 2856 MHz is for a booster accelerator and 5712 MHz is for main accelerator.

To decrease phase noise to make the above mentioned frequency signals, we employ frequency division method. Because dividing by N from a source frequency can decrease the amplitude of signal source noise (phase noise) by up to 1/N at the divider output. Conversely, multiplying by N increases the noise amplitude up to N times. Note that the noise of a commercial synthesizer signal generator does not increase in amplitude proportionally to an increase in frequency [5]. Therefore, we choose the frequency division

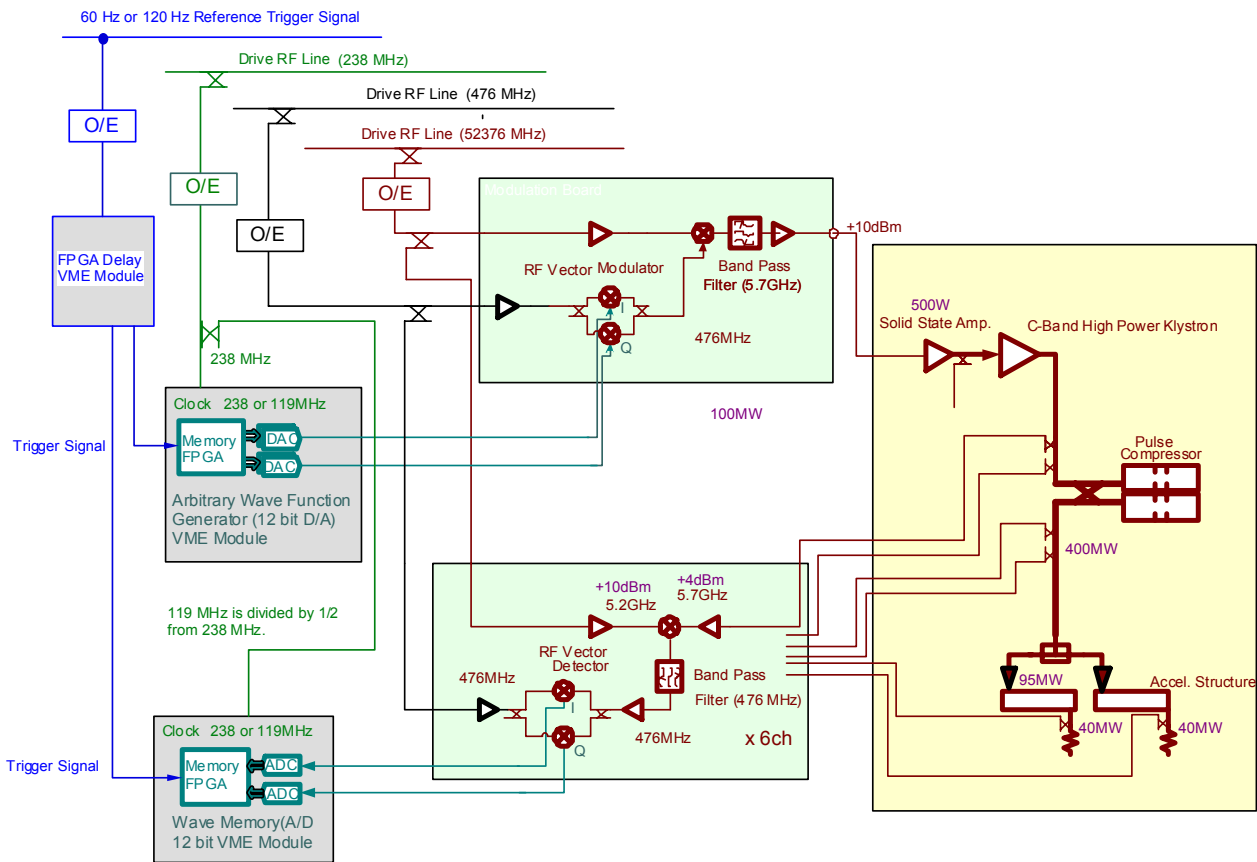


Fig. 2. Low Level rf system for SCSS. This system mainly uses IQ modulation and detection to control the phase and amplitude of rf signals for driving the high power klystrons. The IQ detector and modulator are controlled by VME ADC and DAC modules interfaced to the SPring 8 control system (MADOCA) [6].

method, because of its better low noise characteristic.

The Master Oscillator is composed of:

- a low noise 5712 MHz synthesizer signal generator having an almost pure signal spectrum,
- frequency division and adding circuits for generating the above frequency signals from 5712 MHz,
- and an E/O (Electrical/Optical) converter for each signal.

For obtaining a highly stable optical signal as a time standard, we employ an optical comb generator [7] that generates laser light modulated by the rf signals of the previously mentioned frequencies (Fig. 4). An electrical/optical (LiNbO₃ acoustic modulator) modulates the light. The optical output of this generator has a short

pulse with the frequency spectrum with a comb like structure, with very stable and almost purely monochromatic frequency components. An optical signal of the necessary modulation frequency such as 5712 MHz is extracted from the comb structure by using an optical filter. The wave length of the laser light is 1520 nm and the stability of the 5712 MHz optical component is mainly dependent on stability of the synthesizer signal generator doing the frequency modulation.

II. Signal transmission/distribution system

The role of the signal transmission/distribution system is to transmit and distribute the rf signals such as 5712 MHz generated by the master oscillator system, this is done with cables. To decrease the energy fluctuation of the electron beam in the SCSS linac, the thermal dependence of the

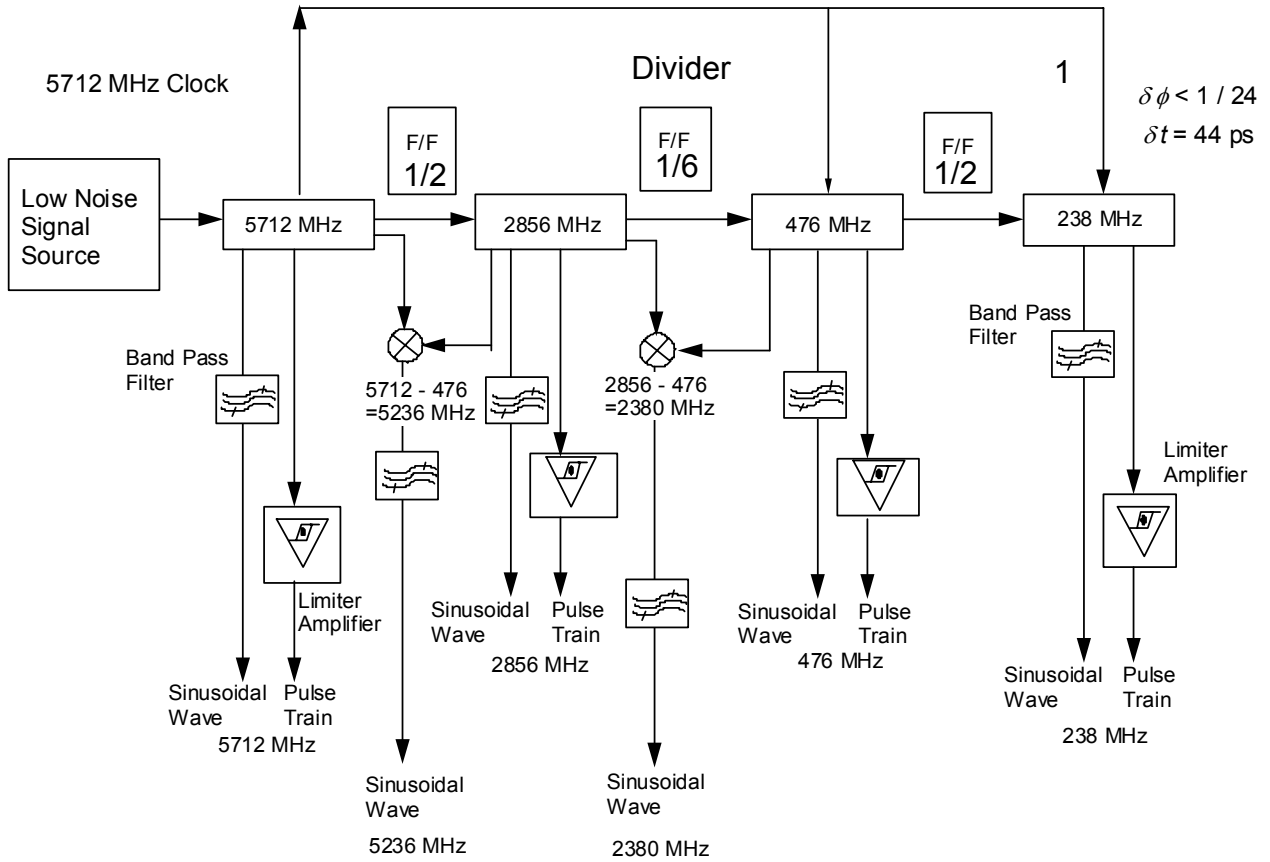


Fig. 3. Master oscillator for SCSS. The signals of 238 and 476 MHz are for a sub-harmonic buncher and a booster accelerator. The 2856 and 5712 MHz rf signals are necessary for booster and main accelerators guides. The signals of 2380MHz and 5329MHz are needed for IQ modulations at the input of klystrons.

electrical length of the cables must be reduced. Therefore, we employ a phase stabilized optical fiber cable [8,9] to transmit the signals. The cable is light and small power dissipation. It is a single mode optical fiber where the electrical length change due to ambient temperature changes is compensated for by an LPC (Liquid Polymer Crystal) coating. This LCP material is coated on the outer cladding surface of the cable. The temperature coefficient of the cable electrical length is 2 ppm/°K at 20 °C [9]. An optical coupler splits the signal to feed optical fiber cables driving each klystron. If there is not enough optical power available, an erbium-doped optical fiber amplifier (EDFA) can be used to amplify the optical signal.

III. Driving system

The purpose of the driving system is to convert the optical signal as delivered by the signal

transmission system into an electrical signal, and then to amplify it as necessary before making the phase, amplitude or pulse modulation needed by the user device. A schematic diagram may be seen in Fig. 2.

The details are as follows:

1. The first stage is an O/E converter. In the past, such converters mainly used an avalanche photo diode having a high speed pulse response. However, this diode is noisy. At the present time, an O/E converter with a PIN photo diode which has low noise is available on the market. Some of these diodes have cut off frequencies up to 40 GHz; they can satisfy our requirement for transmitting 5712 MHz. Therefore, we plan to use PIN photo diode based O/E converter.
2. After the O/E converter, there is an IQ (In-phase/Quadrature) modulator to produce pulse, phase and amplitude modulation.

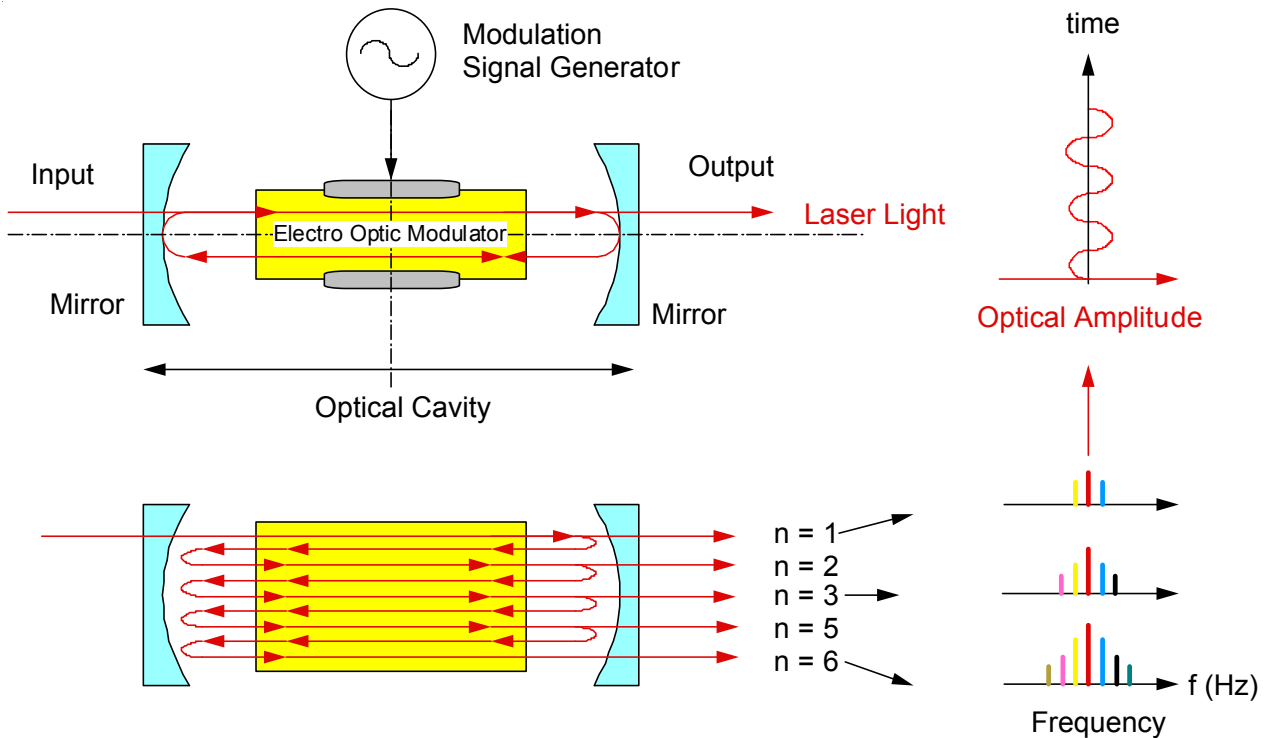


Fig. 4. Schematic drawing of an optical comb generator. This instrument generates an accurate and stable optical signal having a comb frequency structure.

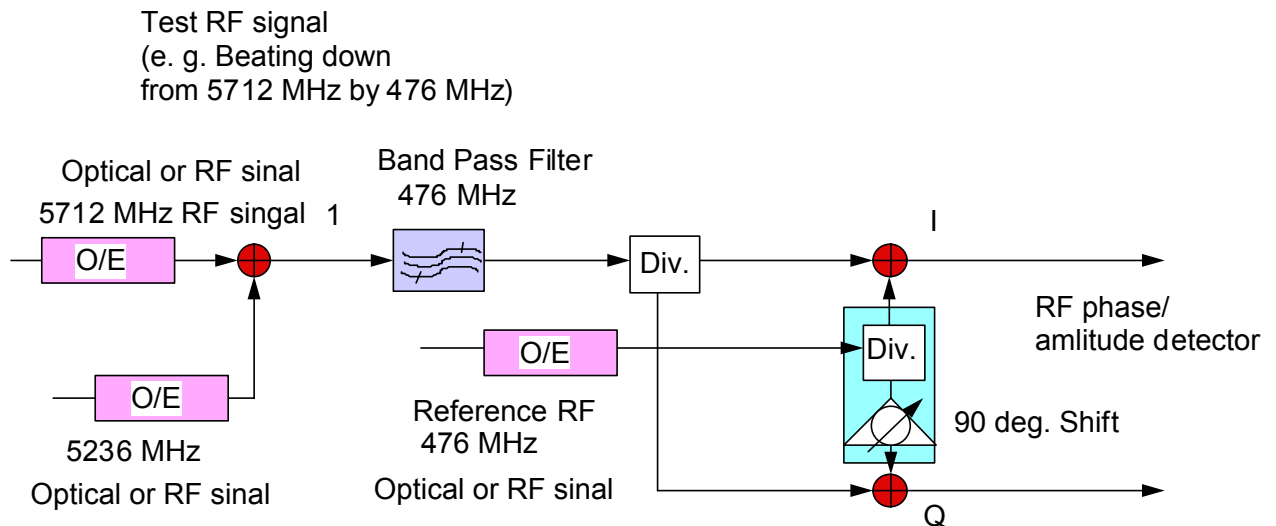


Fig. 5. IQ modulator for generating drive signals for high-power rf sources such as the klystrons.

- Figure 5 shows a schematic of the modulator. It can be used for functions such as rf pulse modulation to drive the klystron and make phase adjustments between the electron beam and acceleration rf so as to obtain the maximum energy gain.
- Following that there is a 600W solid state amplifier in the modulator for driving the

klystrons.

- Besides the driving functions described so far, it is also necessary to monitor the phase and amplitude of the rf outputs of the klystrons and accelerator structures. To do this, an IQ detector as shown in Fig. 6 can be used. The detector can also obtain phase/amplitude information from beam

induced fields in the accelerator structures (e. g. for phase adjustment) and monitor the variation in individual rf pulse energies.

TRIGGER PULSE TRANSMISSION SYSTEM

A trigger pulse transmission system using copper coaxial cable can be difficult to use in high speed applications because the pulse raise time is slowed because of high frequency attenuation due to the skin effect on the inner conductor of the cable. But without a fast raise time, an accurate trigger time to fire an instrument or data acquisition is impossible. For these reasons, we employ an optical fiber cable system for transmitting trigger pulses. Figure 1 shows the overall system that is comprised of a master trigger, an optical transmission plant, and a signal splitting and distribution system.

The necessary operational functions provided by the system are as follows:

- a. A master trigger pulse train establishing the electron beam acceleration cycle is necessary for pulsing the electron gun and klystron modulators. This master trigger system is always operated at its maximum rate, 120 Hz.
- b. Depending on the operational mode, the

master trigger pulses might have to be either synchronized or unsynchronized with the commercial power mains frequency of 60 Hz. But they should always be synchronized with the 5712 MHz acceleration frequency. This synchronization is what guarantees accelerating the electrons at stable point on the rf crest, and ensures the energy/current stability of the accelerated electron beams.

- c. The master trigger system can set any repetition rate up to 120 Hz for independently extracting electron beams from the electron gun and pulsing the klystron modulator. The system continuously outputs master trigger pulses. Functions of parts a. and b. are included in the Master Trigger.
- d. Each trigger pulse, distributed over optical fiber from the master trigger to the various accelerator devices, should be re-synchronized to the 5712 MHz reference clock, or one of its divisor frequencies, at the individual driven devices. This can decrease rise time jitter in the trigger pulse.
- e. The trigger distribution circuit (Fig. 7) belonging to local devices such as the klystron modulators should be able to arbitrarily control whether to activate or inactivate the trigger pulse at each device, and individually set any repetition cycle pattern. The signal distribution part of the

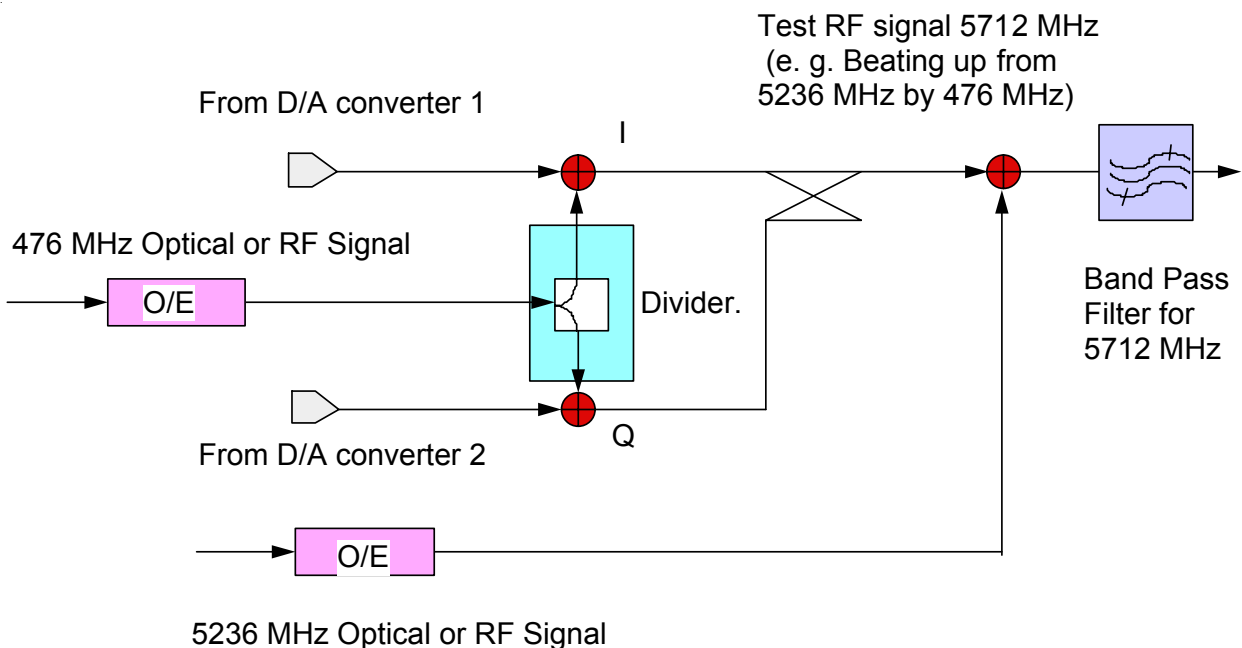


Fig. 6. IQ detector for monitoring the output signals from high-power rf sources such as the klystrons.

trigger pulse transmission system implements the functions of parts d. and e. Figure 8 shows the trigger sequences for the main accelerator including the klystron (Fig. 8-A) and the injector including the electron gun (Fig. 8-B).

The trigger items of interest are shown as follows:

Injector/Accelerator related signals (I-VIII)

- I. A pre-trigger and a trigger to start the thyatron of the high-voltage modulator for the electron gun. These triggers generate a high voltage pulse.
- II. A trigger to decide the repetition rate of the electron beam.
- III. A trigger for the deflector which determines the beam pulse width.
- IV. Triggers for the IQ modulators and amplifiers of the 238 MHz and 476 MHz sub-harmonic buncher and booster.
- V. A pre-trigger and a trigger for the thyatron

of the S-band klystron modulator.

- VI. Triggers for the IQ modulators of the input drive rf signal to the S-band booster accelerator.
- VII. Triggers for the A/D converters used in monitors of beam positions, rf signals, and high-voltage signals around the injector accelerator.
- VIII. Triggers for other data acquisition units such as in the various PLC (Programmable Logic Controller) devices.

Main accelerator related (A-D)

- A. Pre-triggers and triggers for the thyatrons of the C-band klystron modulators.
- B. Triggers for the IQ modulators for the input rf signals to the C-band main accelerator.
- C. Triggers for A/D converters for the monitors of beam positions, rf signals, and high-voltage signals around the C-band main accelerator.
- D. Triggers for data acquisition such as PLC devices.

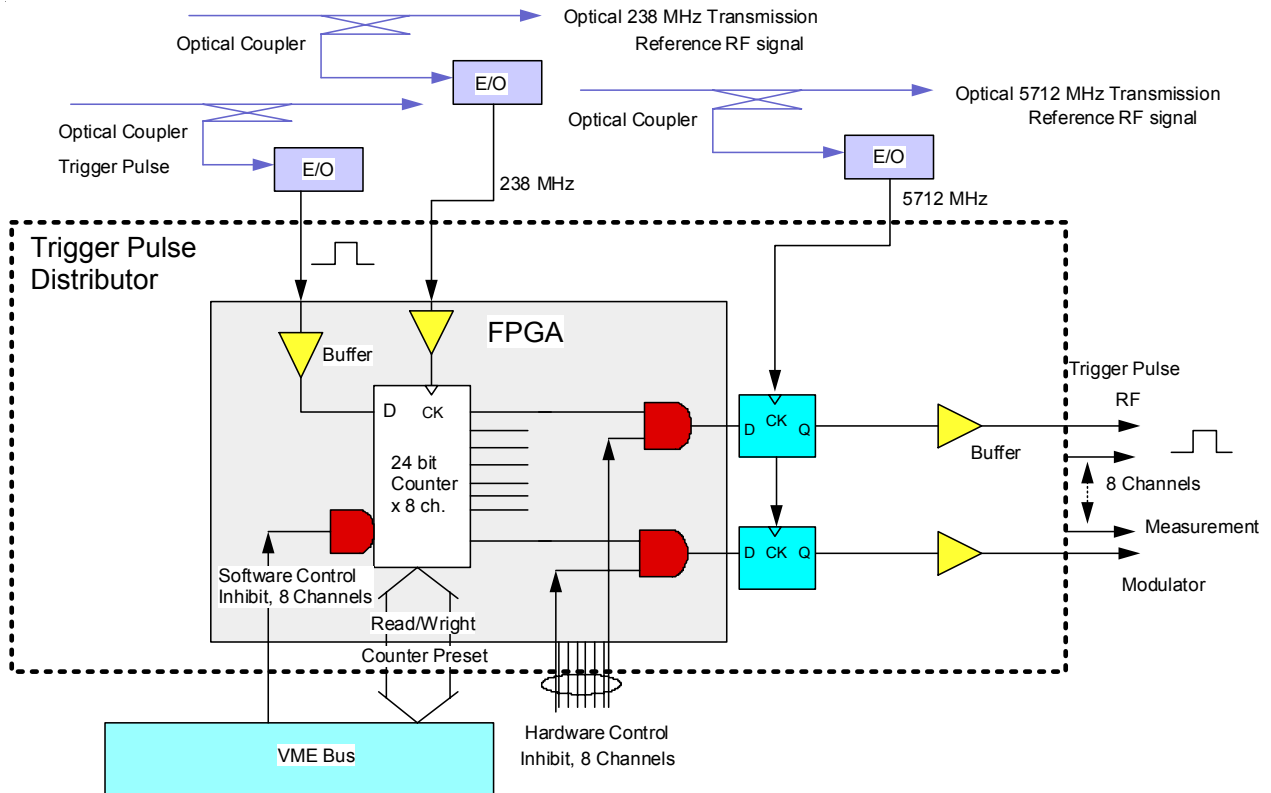
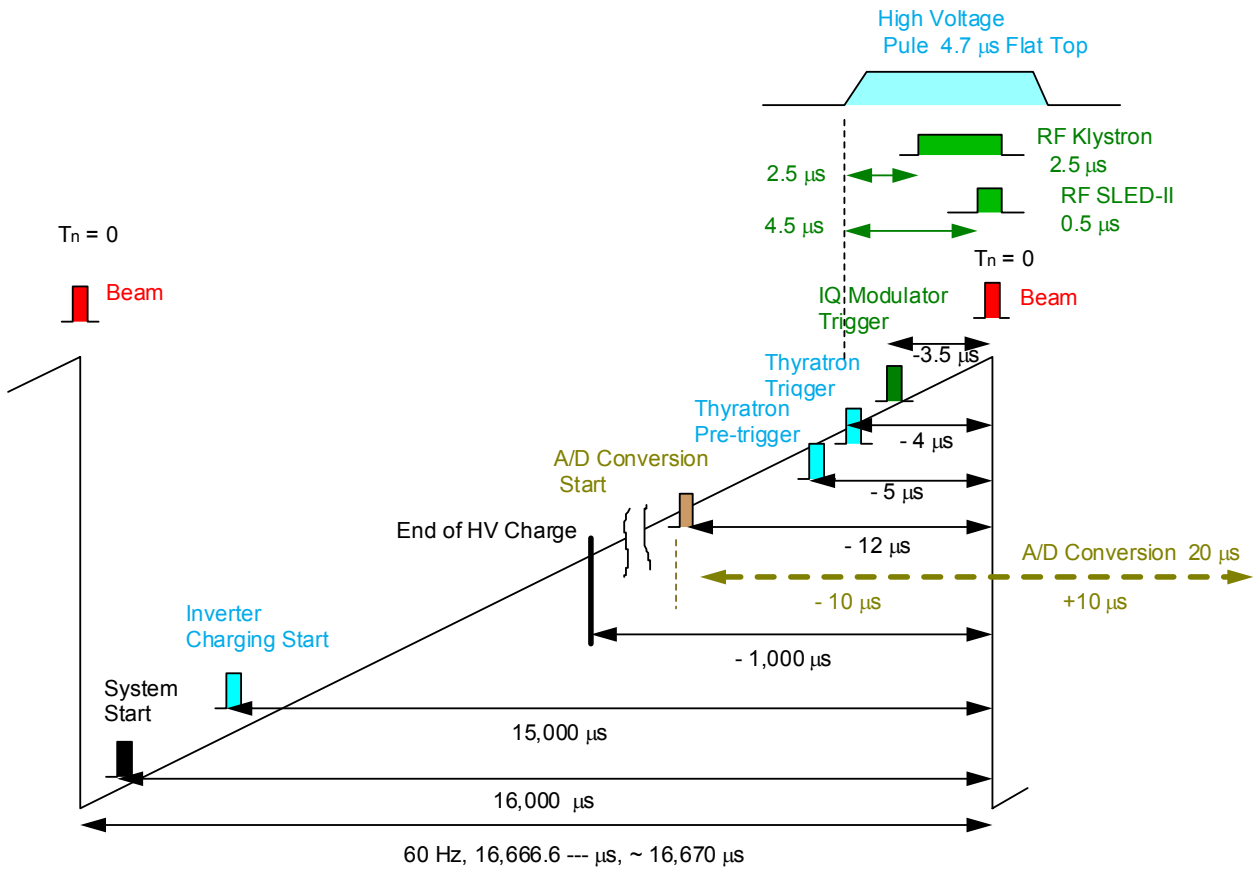
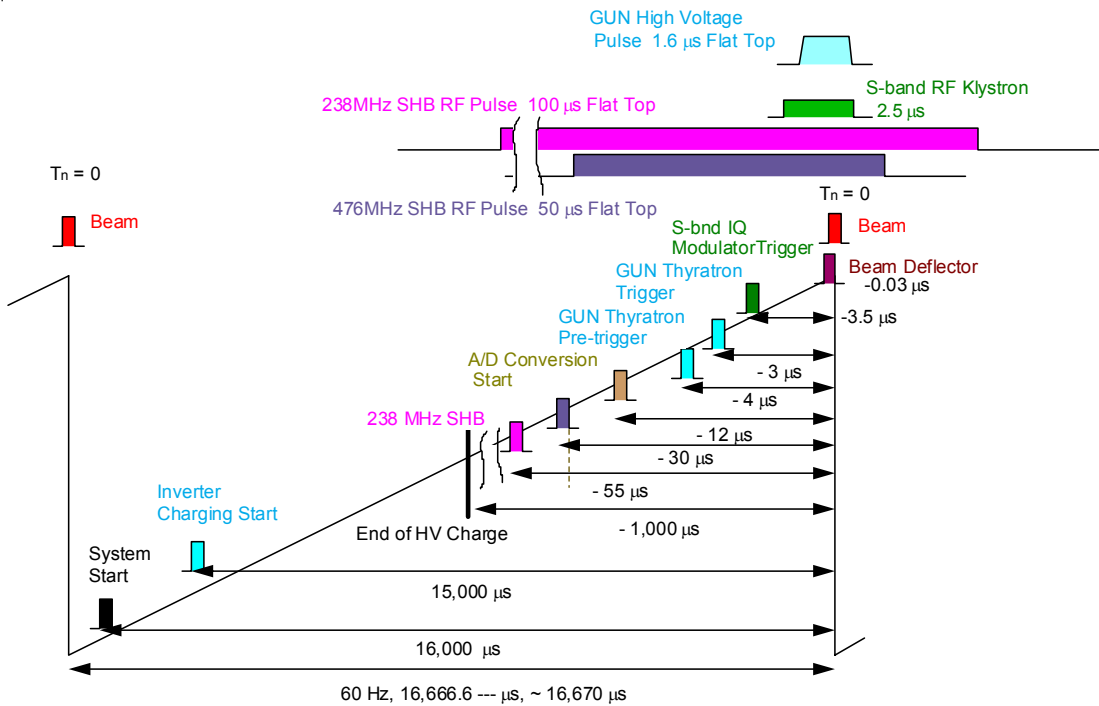


Fig. 7. The block diagram of a trigger distribution circuit using FPGA. It controls activating timings of devices such as the klystron modulators, and ensures synchronization the output trigger pulse to 5712 MHz rf signal.



A) The timing sequence to activate the main accelerator components (such as the klystrons).



B) The timing sequence for the injector accelerator components (such as the electron gun).

Fig. 8. SCSS accelerator timing chart and trigger signals.

Downstream of the main accelerator:

1. Triggers for the pulse magnet used to switch the beam trajectory and for instruments such as streak cameras.

To implement the above functions and the synchronization to the 5712 MHz rf signal at the master trigger and distribution units, we employ fast GaAs logic IC's and FPGA's with counters as shown in Fig. 7.

REFERENCES

- [1] T. Shintake, "Status of the SCSS Project", Asian Particle Accelerator Conference (APAC 2004), MOM102, March 22-26, 2004. Gyeongju, Korea
- [2] Refer to the SCSS Scientific Case, This Report.
- [3] H. Hanaki, "Stability of RF Signal (Low Power RF system)", Design Report on PF Injector Linac Upgrade for KEKB, KEK Report 95-18, Chap. 9.1.2, pp 188-196, 1996 in Japanese.
- [4] <http://www.mitsubishi-cable.co.jp/>
- [5] Agilent technology catalog, p 149, 2004.
- [6] Refer to the SCSS Control System, This Report.
- [7] M.Kouroggi, B.Widiyatmoko, K.Imai and M.Ohtsu "Generation of Expanded Optical Frequency Combs", Edited by A.N Luiten, "Frequency Measurements and Control", Springer-Verlag Berlin Heidelberg 2001, pp 315-335
- [8] Kakuta, Tanaka, "LCD Coated Optical Fiber with Zero Thermal Coefficient of Transmission Delay Time", Sumitomo Electric Industries Ltd., Yokohma, p 244, Japan.
- [9] S. Tanaka, "Phase Stabilized Optical Fiber", Tec. Rep. of Sumitomo Electric Ind. Ltd., 1989.

RADIATION SAFETY ISSUES

SCSS relies on SPring-8 experience and know-how for radiation safety analysis (design of the shielding, including beamline shielding) and management (radiation safety system). Preliminary studies confirmed that skyshine is the most critical issue for the design of the SCSS bulk shield, because of the low annual dose limit at the site boundary and the short distance between the beam (dumps, slits) and the site boundary. SPring-8 being a multi accelerator complex, the dose criterion at the site boundary has also a strong influence on shielding.

BASIC CRITERIA

The shielding design criteria are based on the ALARA (as low as reasonably achievable) principle, the dose limits being set by the law regulating the prevention of radiation hazards and by SPring-8 regulations (Table 1). By the law, the effective dose limits to radiation workers from both internal and external radiation sources are 50 mSv per year and 100 mSv with in5 years. For the public, the dose within 3 months must not exceed 1.3 mSv at the boundaries of the controlled area, and 0.25 mSv at the boundaries of the site. However, SPring-8 regulations enforce a dose limit for radiation workers equal to one third of the legal dose limit (8.3 μ Sv/h), while at the site boundary (public area) the total annual dose limit is set at 50 μ Sv. Actually, SPring-8 being a multi accelerator facility, the maximum allowance for the SCSS is about 20 μ Sv/y.

Finally the design and operation of the SCSS safety systems (radiation monitoring system, access control system, interlock system and data management) should be consistent the SPring-8 safety system: while the SCSS will be operated independently from the other SPring-8 accelerators, its radiation safety systems will be integrated to the SPring-8 system.

SHIELDING DESIGN

Beam parameters and geometrical configuration

Fig. 1 shows a schematic view of the SCSS with the closest distance between the loss points, the beam dump and the site boundary: the linac will be located along the SPring-8 one kilometer long beamline, with the undulators and beam dumps installed in the direction of the SPring-8 storage ring. As a result, the distances from the electron beam loss points and the beam dump to the site boundary are about 180 m and 80 m respectively. As explained hereafter, such short distances add extra constraint on the design of the shield (skyshine).



Figure 1 : Schematic view of the SCCS showing the closest distance between the loss points, the beam dump and the site boundary (in red).

Table 1: Maximum dose limits set by the law and by SPring-8 regulations

Area	Law	SPring-8 regulation
Radiation workers	50 mSv/y and 100 mSv/5y	8.3 μ Sv/h
Boundary of the controlled area (Public)	1.3 mSv/3 months	-
Boundary of Spring-8 site (Public)	0.25 mSv/3 months	50 μ Sv/y

The SCSS will operate at energies up to 6 GeV in single bunch mode (1 nC) at 60 Hz. The operation time is assumed to be the same as SPring-8, that is 8000 hours. Once set up for user operation, the linac is principally a low beam loss machine, with several slits to scrap the insufficiently tuned electrons. Therefore, it is reasonable to assume that the point wise beam losses occur at the slits with a rate of 1 %.

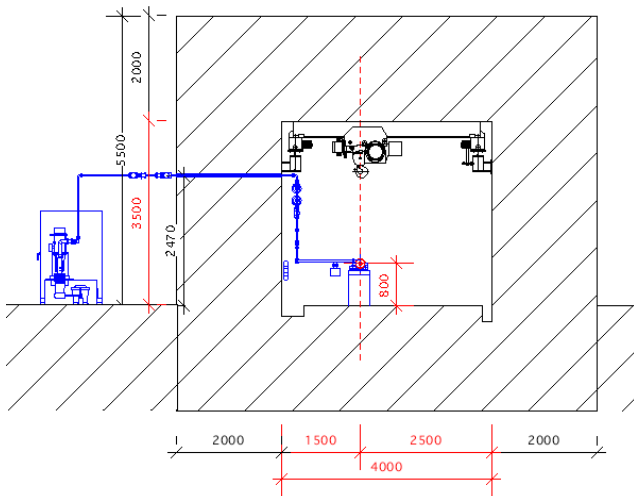


Figure 2 : Schematic view of a cross section of the SCSS linac tunnel : the tunnel is 4 meters wide, 3.5 meters high, with the beam at 80 cm from the floor and 2.5 m from the wall of the non-controlled area.

The cross section of the linac tunnel used for dose evaluations is shown on Fig. 2: the tunnel is assumed to be 4 meters wide, 3.5 meters high, with the beam at 80 cm from the floor and 2.5 m from the wall of the non-controlled area. The beam dumps, located underground, have a double structure (graphite and steel) to reduce the production of radiation and minimize the thickness of the shielding material (Fig. 3).



Figure 3 : Cut away view of the beam dump : the inner cylinder is made of graphite, the outer one from iron.

Neutrons and gamma-rays due to electron beam losses were considered in the direction perpendicular to the electron beam axis, and the SHIELD 11 code [1] was used with ordinary concrete characteristics (density 2.1 g/cm^3). Skyshine dose calculations were performed with the Stevenson-Thomas formula and the SPring-8 analytical method [2].

Bulk shield

The calculation results show that the annual dose limit at the site boundary is critical for the shield design because of the short distance between the linac and the site boundary. Moreover, as noted previously, when considering the total annual dose at the site boundary, the contributions from the different SPring-8 accelerators mean that the margin for the SCSS annual dose is less than $20 \text{ } \mu\text{Sv/y}$. For the tunnel, the calculations indicate that 2 m of ordinary concrete is enough to satisfy the dose criteria for the radiation workers and the dose criteria at the boundary of the controlled area. However, to satisfy the annual dose criterion at the boundary of the SPring-8 site, 3 m of concrete or 2 m of concrete plus an additional iron local shield (40 cm) is needed.

As for the beam-dumps (Fig. 4), they will be installed underground and inclined at 20° . To satisfy the dose criterion at the boundary of the controlled area (radiation workers), the thickness of the ordinary concrete shield is set to 2 m in the lateral direction, and 3 m in the forward direction. However, to satisfy the annual dose criterion at the site boundary (public) requires 3 m of ordinary concrete, with an extra 50 cm of iron laterally.

Photon beam shutter and photon absorber

In addition to the neutron and gamma photons due to electron beam losses, the gas bremsstrahlung and associated photon neutrons must be considered, as well as the muons emitted forward of the beam shutter or photon absorber, especially as these are installed on the beamline axis (the direction of the experimental hutch). Gas bremsstrahlung has been thoroughly investigated for third generation

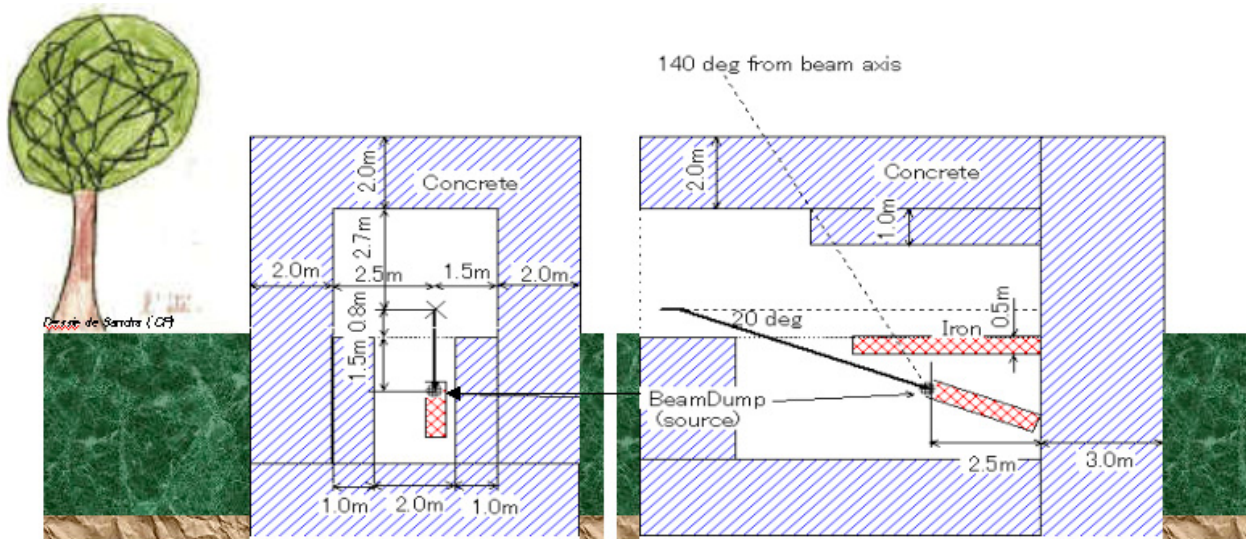


Figure 4 : Schematic view of the beam dump area : the beam dump is set with an inclination of 20°.

synchrotron radiation facilities [3] because of its high energy and its high directionality, which mean that it can easily propagate down into the beamline. However, for the SCSS, unlike storage type facilities, the intensity of gas bremsstrahlung is expected to be lower because of the low intensity current: assuming the same residual gas pressure as that of the standard SPring-8 straight section (1 nTorr), intensity is expected to be five orders of magnitude smaller. Still, the maximum dose rate due to gas bremsstrahlung outside of the shield tunnel is at least 80 $\mu\text{Sv/h}$, so that a shield such as a beam stopper must be considered.

The high energy gas bremsstrahlung will also generate photoneutrons through interaction with the high Z materials of the beamline components. However, since in the case of the SCSS the intensity of gas bremsstrahlung is low, the dose due to the photoneutrons will be, in general, negligibly small.

Muons are produced and emitted in the forward direction at the electron beam switch yard, undulators, slits and the beam dumps. The dose due to muons is not so high: for example, it is about 1 $\mu\text{Sv/h}$ at 10m from the source point for a 1% beam loss. However, the relative importance of the dose due to muons grows up as the shield thickness increases.

For SCSS, the shield ability that the beam shutter or photon absorber is expected to have is therefore determined by the neutrons and gamma-rays due to the electron beam losses. Concretely speaking, a beam shutter with an equivalent shield ability of 1.5 m of iron is required in the case of a 1 % beam loss seen at a distance of 13 m from the outside of the shield tunnel.

Finally, since synchrotron radiation imparts intense heat to the beam shutter or the photon absorber, countermeasures should be considered to reduce the heat load. Shielding from the scattered photons of synchrotron radiation should also be considered.

INDUCED ACTIVITY

The induced radioactivity due to irradiation by the electron or bremsstrahlung beams were estimated by using the saturation activity of a unit electron beam loss and the data summarized in the SPring-8 [2] and IAEA [4] reports. For example, it was found that the main induced activities are Nitrogen-13 in air and Beryllium-7 in water. However, since the SCSS will use an exhaust system with long retention time and a closed cooling water system, additional attention must be paid to radio isotopes such as Argon-41 and Tritium. Similarly, the dose due to induced activity could be

derived from the saturation activity data and QAD-CGGP2, a point kernel method code [5] : at 1 m from the graphite beam dump, the dose was evaluated at 83 $\mu\text{Sv/h}$ just after the shutdown and 0.43 $\mu\text{Sv/h}$ one day after the shutdown.

SAFETY SYSTEMS

The SCSS safety systems, which consist of a radiation monitoring system, an access control system and an interlock system, are described conceptually in Fig. 5. All these systems should be operated consistently under the SPring-8 systems and all the safety data should be managed in an integrated fashion. Basically, all parts of the system which relate directly to human safety are connected to each other by hardwire. The ones not related to human safety can be operated independently.

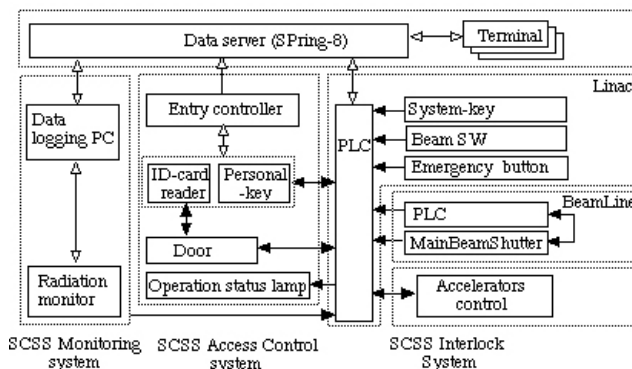


Figure 5 : The SCSS safety systems.

Radiation monitoring system

The radiation monitoring system consists of area monitors, which will be installed in and around the radiation controlled areas, and gas monitors which will be installed in the exhaust systems of the accelerator tunnel to check the level of radioactivity concentration. Some of the area monitors will be connected to the interlock system, to shutdown the machine operation if necessary. Besides, passive dosimeters will be attached to possible “hot” spot, to measure the cumulative dose over a week or a month. Since the SCSS cooling water systems will run in a closed circuit, the water will normally not discharge into the general waste lines. Nevertheless, from time to time, the activity of water samples will

be checked with off-line liquid scintillation counters.

Access control system

The controlled area will be accessible through an auto lock door equipped with an ID card reader: only the persons having an ID card with the due authorization will be allowed to enter. The entrance to the accelerator tunnel will use the same system as SPring-8: this personal key system, which is connected to the interlock system, allows to confirm simultaneously who enters the controlled area and the accelerator tunnel.

Interlock system

The safety interlock system consists mainly of PLC (Programmable Logic Controller) and hard wires which connect the PLCs. In order to keep the independence, the main interlock must be set up with two different systems by using PLC and multipurpose logic circuits. The interlock systems of the beamlines and the accelerator have to be constructed independently. The safety interlock system of the beamline is closed by itself and the status is monitored to give the permission to operate the accelerator. The interlock system of the accelerator must be designed on the basis of the centralized operations.

REFERENCES

- [1] SLAC SHIELD11 - an analytical shielding code maintained at SLAC Current version, 2000a.
- [2] Asano Y., and Sasamoto N., “Radiation shielding and safety analysis for SPring-8” JAERI-Tech 98-009 (1998) in Japanese.
- [3] Asano Y., “A Study on radiation shielding and safety analysis for synchrotron radiation beamline”, JAERI-Research 2001-006 (2001).
- [4] Swanson P., “Radiological safety aspects of the operation of electron linear accelerators”, IAEA Technical Reports series No.188 (1979)
- [5] Sakamoto Y., and Tanaka S., “QAD-CGGP2 and G33-GP2 : Revised Versions of QAD-CGGP and G33-GP Codes with Conversion Factors from Exposure to Ambient and Maximum Dose Equivalents”, JAERI-M-90-110 (1990)